ABSTRACT

Title of Document: STUDY OF THE FEMTOSECOND DYNAMICS AND SPECTROSCOPY OF LASER IONIZED PLASMAS.

Jennifer Anne Elle, Doctor of Philosophy, 2015

Directed By: Professor Howard Milchberg
Department of Physics

Ultra-short laser pulses are used to ionize gas in different configurations and study the plasma and ionization dynamics. The variation in non-linear index of refraction as a function of time is used to diagnose laser-plasma interactions. First, a proposed novel method to stimulate lasing in the atmosphere is studied. A few mJ pulse is used to ionize nitrogen gas in a long column without dissociating the molecular nitrogen. A 140ps laser is used to heat the resulting electron population in an attempt to generate a population inversion between the $C^3\Pi_u$ and $B^3\Pi_g$ states of molecular nitrogen. No evidence of lasing from this transition is observed. Next, a few mJ pulse is used to ionize xenon gas, creating Xe^+ plasma. Ionization in Xe^+ is observed far below the threshold predicted by multiphoton ionization theory due to resonant multiphoton ionization of collisionally excited states. To my knowledge, this is the first observation of resonant ionization involving multiple resonances. Finally, construction of an experiment to detect predicted

birefringence in a relativistic laser-plasma interaction is described, with preliminary testing of diagnostics included.

STUDY OF THE FEMTOSECOND DYNAMICS AND SPECTROSCOPY OF LASER IONIZED PLASMAS.

By

Jennifer Anne Elle

Dissertation submitted to the Faculty of the Graduate School of the
University of Maryland, College Park, in partial fulfillment
of the requirements for the degree of
Doctor of Philosophy
2015

Advisory Committee:
Professor Howard Milchberg, Chair
Professor Wendell T. Hill III
Professor Ki-Yong Kim
Professor Phillip Sprangle
Dr. Jared Wahlstrand

Dedication

This work is dedicated to my family. To my mom and dad who have always encouraged me to chase my dreams and who have supported me in whatever I chose to pursue. To my sister, whose friendly competition has driven me. To my husband, who made physics fun again and basically talked me into going to graduate school.

Acknowledgements

Research is entirely a cooperative endeavor, and there are many people without whom this work could not have been done. First, I would like to thank my advisor Professor Howard Milchberg for teaching me how to run a scientific experiment, sharing his many years of experience and physical insights, and for providing many shiny toys for me to play with.

I also need to thank Dr. Jared Wahlstrand for being incredibly generous with his time and keeping me pointed in the right direction. Thanks for teaching me that sometimes you just have to persevere and other times it is better to try another approach rather than fighting with the one which isn't working. The trick is knowing the difference.

And of course, my fellow graduate students with whom I have shared this wonderful, infuriating journey. Thanks to Brian Layer and Yu-hsin Chen who taught me most of what I know about lasers. Thanks to Sung-Jun Yoon, Andy Goers, Sina Zahedpour, and George Hines with whom I have brain-stormed, conspired, commiserated and spent long evenings and weekends getting our temperamental machine to work. I am so glad to have had the chance to work with and learn from all of you. Thanks to the undergrads Linus Federer, Reuven Birnbaum, and Colin Kennedy who have worked with me over the years.

Though not directly involved in research, the shop and office staff of IREAP have been enormously helpful during my time as a graduate student.

Finally, I thank my husband Remington Reid for keeping me sane. I'm not sure I'd have made it without you.

Table of Contents

List of Figures

Chapter 1 : Introduction

This thesis addresses several experiments involving the study of high-intensity laser pulses interacting with the gas and plasma states of matter. The laser pulses involved are several tens of femtoseconds to hundreds of picoseconds in duration, as are the experimental timescales of interest. Electronic diagnostics are too slow to accurately resolve such short time-scales, so all-optical diagnostics are used in this work. Most notably, a unique spectral interferometry diagnostic is used to measure perturbations of the material index of refraction due to interaction with high intensity laser pulses. Chapter two is a review on how the material index of refraction changes in response to exposure to laser fields of varying intensity. Chapter three then describes the spectral interferometry diagnostic used throughout the later chapters. Much of the development for this diagnostic is described elsewhere. A description of the instrumental error due to calibration is included here for the first time, as is a discussion on the measurement error introduced by refraction effects. Chapter four describes the student-maintained laser systems used in this work, including installation of a new seed laser in a pre-existing 140ps Nd:YAG system and synchronization between the Nd:YAG system and a 20 TW Titanium:Sapphire laser.

Subsequent chapters each describe a study of laser-matter interactions under different conditions. Previous examination of short pulse laser-matter interactions has enabled new technologies such as laser machining [1], reliable high-precision eye surgery [2], art restoration [3], and laser spectroscopy to name just a few. There are also many exciting current areas of research. For example: compact electron [4] and ion accelerators for medical applications [5], attosecond spectroscopy [6], and remote sensing [7]. The

experiments described in this thesis are contributions to the scientific effort to investigate material behavior upon exposure to short-duration, high intensity optical fields.

Chapter five describes an investigation of an atmospheric UV wavelength laser which could in future be projected to a location at some remove from the generating laser facility for application in remote sensing spectroscopy. The proposed population inversion is between the $C^3\Pi_u$ and $B^3\Pi_g$ vibrational states of N_2. Recent theory suggests the lasing transition may be excited using a two-pulse synchronized laser system unique to the Maryland laser-matter interactions group. The experiment and results are described in detail.

In chapter six, an anomalous ionization signal from a pre-formed singly ionized xenon plasma due to an ultra-short pulse is studied. It is shown that ionization occurs at an intensity two orders of magnitude below that predicted by non-resonant multiphoton ionization theory. The ionization mechanism is due to a never-before studied highly resonant multiphoton process which ultimately has the same signature as single-photon ionization. It is thought that the process is generalizable to other large atoms besides xenon, which are the subject of future studies. Numerical simulations of a multi-level atomic system are compared with experimental results and a possible ionization pathway is presented.

Finally, chapter seven describes the construction and on-going trouble shooting of an experiment designed to measure birefringence in plasma due to relativistic electron motion. Plasma optics are highly desirable in laser applications where the laser intensity exceeds the damage threshold of solid materials. If plasma birefringence can be demonstrated and explored fully, a new generation of polarizing optics without a limiting

damage threshold may be developed. The SSSI spectral diagnostic described in chapter three and used extensively in chapter six is well-suited to diagnosing plasma birefringence, but SSSI has not yet been applied to a multi-terawatt laser system and new sources of experimental noise must be isolated and removed before the diagnostic achieves the necessary sensitivity. The experiment is a work in progress and results to date are presented.

Chapter 2 : High Field Nonlinear Processes

2.1 Introduction

Introductory texts on the topic of optical electromagnetic fields in matter present the material response as linear in the electric field. That is, the frequency-dependent polarization induced in an atom or molecule is proportional to the electric field $E(\omega)$. The proportionality factor $\chi_e(\omega)$ (linear susceptibility) is dependent on the atomic or molecular structure and proportional to the atomic/molecular density: $P(\omega) = \chi_e(\omega)E(\omega)$, where $P(\omega)$ and $E(\omega)$ are the amplitudes of the polarization and field components at frequency ω. Alternatively $P(\omega)$ and $E(\omega)$ can be considered to be Fourier transforms of the time-dependent fields $P(t)$ and $E(t)$. In actuality, linear optics may be viewed as approximate model useful for relatively weak single frequency fields based on the expansion of the material response as a Taylor series $P = \sum_n K^{(n)} \chi^{(n)} E^n$ where K is a numeric degeneracy factor. In circumstances where more than one frequency component is present in the system, the material response due to each driving frequency and due to new frequencies created by the beating of the electric fields must be calculated to obtain the polarization of the material. In strong electric fields significant contributions to the physical behavior of a system come from higher order terms that are not linear in the electric field. As the field strength increases these higher order terms become progressively more important and a host of nonlinear effects arise which are not present in the linear theory. Eventually, the field becomes so strong that ionization and plasma effects must also be included. A large subset of nonlinear processes are those

involving multiple frequencies. These processes are well studied and will not be considered here. For the interested reader, references can be found for second and third harmonic generation [8], sum and difference frequency generation [9], optical parametric oscillation and amplification [10], [11], four wave mixing [12], optical phase conjugation [13], optical rectification [9], parametric down-conversion [14], and the Pockels effect [15]. In this chapter, the different regimes of physics experienced by bound and free electrons as the electric field strength is increased will be discussed. The discussion assumes a laser as the source of the electric field.

As the field strength is increased beyond the regime where a linear approximation applies, bound electrons experience a time- and field-dependent potential consisting of the atomic coulomb potential plus laser field. Eventually, the field strength is such that the bound electrons are removed from the parent atom and plasma is generated. Several nonlinear ionization regimes are traversed as the field strength increases further, until the electromagnetic field is so strong the magnetic contribution becomes significant and nonlinear effects in the free electrons are observable. This chapter nonlinear processes in detail in a gas medium for intensities from 10^{10} to 10^{18} W/cm^2.

2.2 Linear optics

In the linear regime, the material polarization in a linearly polarized laser field is due to the driven oscillation of electrons bound to a positively charged nucleus by the Coulomb force. A very simple model for the atomic response considers the bound electron experiencing a linear restoring force from the nucleus with the laser field as a driving term. A phenomenological damping term is also included to give a differential equation for the displacement $x(t)$ of the electron.

$$\frac{d^2\vec{x}(t)}{dt^2} + \Gamma \frac{d\vec{x}(t)}{dt} + \Omega^2 \vec{x}(t) = -e/m_e \, \vec{E}(t) \tag{2.1}$$

The electric susceptibility of a gas is the polarizability $\alpha(\omega)$ of an atom times the atomic number density *N*, $\chi(\omega) \equiv N\alpha(\omega)$. The polarizability may be found from the induced atomic dipole moment due to the driving electric field $\vec{p} = e\vec{x} = \alpha\vec{E}$. In general, an atom will have *j* electronic states, each with a different resonant frequency and damping term. A sum over *j* states must therefore be added to the electric susceptibility. Solving Eq (2.1) with a driving field of frequency ω gives χ:

$$\chi(\omega) = \frac{Ne^2}{m_e} \sum_j f_j \frac{i\Gamma\omega + \Omega_j{}^2 - \omega^2}{(\Omega_j{}^2 - \omega^2)^2 + \Gamma_j{}^2\omega^2} \tag{2.2}$$

with f_j, the classical oscillator strength, equal to the number of electronic states per atom with resonant frequency Ω_j. Then the linear material polarization

$$P(\omega) = \chi(\omega)E(\omega) \tag{2.3}$$

To transform Eq (2.3) back to the time domain, $\chi(\omega)$ may under certain circumstances be approximated as a constant, or very weakly dependent on ω. First, the frequency of the electric field must be far from any atomic resonance. If the field is not monochromatic, then the bandwidth should be small so that $\chi(\omega_0 \pm \Delta\omega) \approx \chi(\omega_0)$ where ω_0 is the center frequency. In the adiabatic limit, with $\chi(\omega) = \chi(\omega_0)$, the polarization can be written $P(t) = \chi(\omega_0)E(t)$. Under this condition, a laser pulse propagating through a uniform gas column will emerge with a uniform phase delay proportional to the index of refraction $n_0 = \sqrt{1 + 4\pi \cdot \chi(\omega_0)}$ of the gas without change to the field time history.

2.3 Nonlinear processes

Beyond the linear response, the index of refraction depends on higher orders of the laser field. The nonlinear processes discussed below occur at different laser intensities. In a neutral gas, the optical Kerr effect adds a contribution to the index of refraction which is proportional to incident intensity. As the gas is ionized, the Kerr effect is reduced and the plasma contribution to the index of refraction dominates. At high enough intensities, relativistic electron motion and strong magnetic fields contribute to the plasma response. For $a_0 < 1$ where $a_0 = eA / mc^2 = eE / mc\omega$ is the normalized vector potential, the relativistic contribution is again proportional to intensity. Figure 2.1 shows the different limits of these processes as a function of laser intensity for laser wavelength λ=800nm. For convenience, the gas response is formulated in terms of the index of refraction of the medium rather than polarization. The index of refraction is straight-forwardly related to the phase delay imposed on a laser pulse traversing a medium, which is accessible experimentally as described in chapter 2.

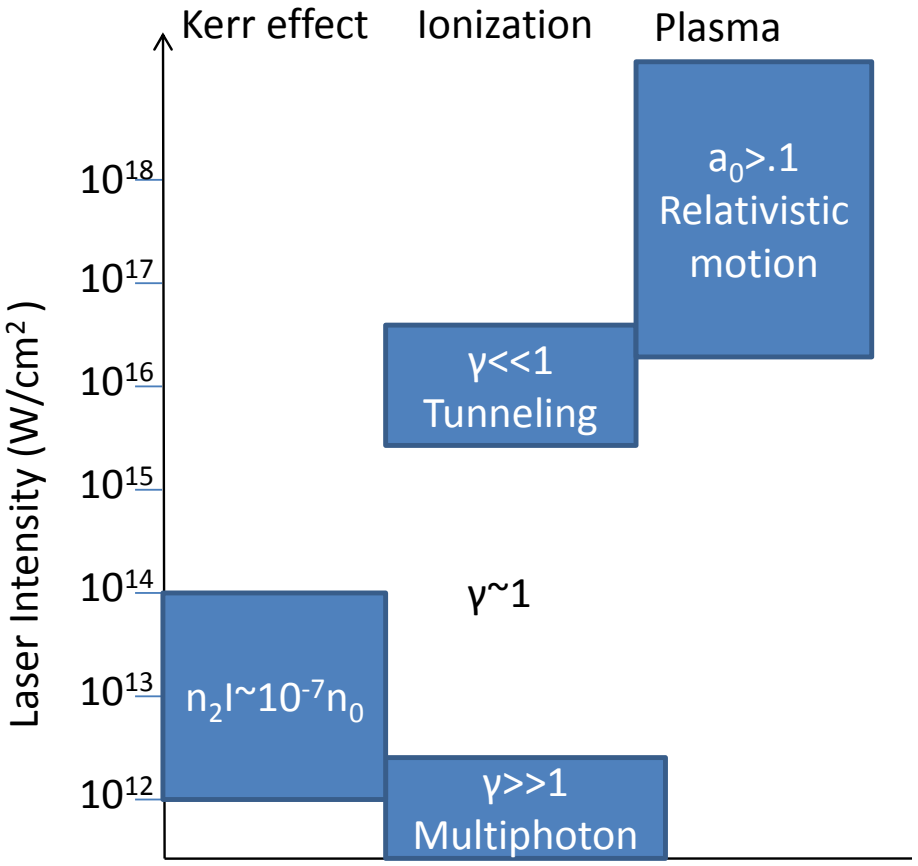

Figure 2.1 Schematic of nonlinear processes and the intensity regimes in which they occur for 800nm light and an ionization potential of 15 eV. See section 2.4 for a discussion of the Kerr effect, section 2.5 for ionization processes, and section 2.6 for relativistic motion.

2.4 Optical Kerr Effect

Consider nonlinear contributions to the electronic response of a gas. A gas medium, being isotropic, has no even order susceptibility terms. The lowest nonlinear term is the third order term, $\chi^{(3)}$. The polarization through third order is

$$P(\omega) = \chi^{(1)}E(\omega) + \frac{3}{4}\chi^{(3)}(\omega)\,|E(\omega)|^2\,E(\omega) \tag{2.4}$$

The polarization can be rewritten to resemble the linear regime in terms of an effective χ which is dependent on the intensity of the laser field, $P(\omega) = \chi_{eff}E(\omega)$ with

$\chi_{eff} \equiv \chi^{(1)} + \frac{3}{4}\chi^{(3)} |E(\omega)|^2$. Converting the square of the electric field to intensity and expressing the nonlinearity in terms of index of refraction rather than electric susceptibility gives

$$n_{eff}(t) = n_0 + n_2 I(t) \tag{2.5}$$

$$n_2 \equiv \frac{12\pi^2 \chi^{(3)}}{n_0^2 c} \tag{2.6}$$

The intensity dependent portion of the index of refraction is known as the optical Kerr effect and is responsible for the nonlinear processes of self-focusing and self-phase modulation from the bound electron nonlinearity. [16] [17]

On the microscopic level, the Kerr effect can be ascribed to distortion of the atomic Coulomb potential due to a strong external electric field. For the driving field frequency away from any resonances, the electron response time is typically sub-femtosecond and can be treated as instantaneous for even single cycle optical pulses. The nonlinear index of refraction is typically on the order of 10^{-19} cm^2/W for gas densities corresponding to 1 atm at room temperature [18]. The instantaneous nonlinear contribution is directly detectable using spectral interferometry [19] at a level $n_2 I / n_0 \sim 10^{-6}$, requiring a laser intensity of ~10 TW/cm^2. In practical units, intensity may be converted to electric field according to

$$E_{\max}\left[\frac{V}{cm^2}\right] \approx 2.75\times 10^9 \left(\frac{I}{10^{16} W/cm^2}\right)^{1/2} \tag{2.7}$$

requiring an electric field strength of $E_0 \sim 3\times10^7\left[\frac{V}{cm^2}\right]$. For reference, the strength of the atomic field for the ground state of hydrogen is $E_{hydrogen} \sim 5\times10^9\left[\frac{V}{cm^2}\right]$.

$E_0 / E_{hydrogen} << 1$ and the measurable Kerr effect onset is in the perturbation theory regime.

In molecular gases, in addition to the prompt electronic response, there is a slightly delayed nonlinear response. The delayed response originates from orientation of the induced molecular dipole moment. Consider for illustration a diatomic molecule. The polarizability of the molecule is not isotropic. Instead the polarizability along the bond axis, $\alpha_{\|}$, is greater than that perpendicular to the bond axis, $\alpha_{\perp}$. See Figure 2.2

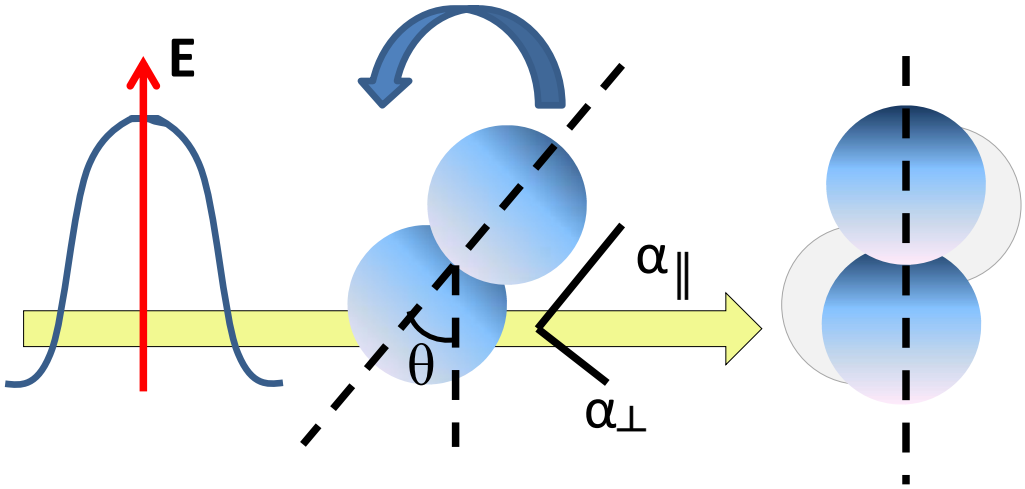

Figure 2.2 Polarized external electric field induces an asymmetric dipole moment on a diatomic molecule. The resultant torque is proportional to the angle θ between the field polarization direction and the molecule axis and rotates the molecule toward alignment with the field.

In the limit of a small electric field, an ensemble average over a randomly oriented population of molecules in thermal equilibrium gives the linear rotational contribution to the index of refraction

$$n_0^{(rot)} = \sqrt{1 + 4\pi N\left(\alpha_{\parallel}/3 + 2\alpha_{\perp}/3\right)} \tag{2.8}$$

where N is the number of molecules [15].

In the presence of a linearly polarized external field, the molecule will experience a torque $\vec{\tau} = \vec{p} \times \vec{E}$, where $\vec{p}$ is the induced dipole moment and $\vec{E}$ is the laser field. For a field with pulse duration much longer than the molecular rotation period, the molecule experiences pendular oscillation with periodic alignment along the field direction [20]. In the case of a pulsed electric field with duration shorter than the molecular rotation time, the ensemble average degree of alignment is a function of time after the driving field:

$$\Delta n^{(rot)} \approx \frac{2\pi N}{n_0}\Delta\alpha\left(\left\langle \cos^2\theta \right\rangle_t - \frac{1}{3}\right) \tag{2.9}$$

The degree of molecular alignment is found from quantum perturbation theory. The laser pulse induces a coherent excitation between the population of states of odd (j) and even (j-2) angular momentum. The states evolve with temporal phase $\exp\left(-i\varepsilon_j/\hbar\, t\right)$ and the ensemble averaged degree of alignment is [21]

$$<\cos^2\theta>_t = \frac{1}{3} - \frac{2}{15\hbar}\frac{j(j-1)}{2j-1}(\rho_j - \rho_{j-2})\Delta\alpha\,\mathrm{Im}\left[e^{i\omega_{j,j-2}t}\int_{-\infty}^{t} dt' E^2(t') e^{-i\omega_{j,j-2}t'}\right] \tag{2.10}$$

where ρ_j (ρ_{j-2}) is the population of the odd (even) angular momentum states and $\omega_{j,j-2} = \frac{\mathcal{E}_j - \mathcal{E}_{j-2}}{\hbar}$ is the difference in energy of the two states. Such systems have been found to undergo periodic alignment and anti-alignment with the driving field [20,21]. The rotational response of light molecules occurs within several hundred femtoseconds of the driving impulse [18], so sub-hundred femtosecond pulses are necessary to resolve the difference between the instantaneous and delayed electronic response in molecular gases. The time for one full period of the molecular rotation is on the order of a few hundred femtoseconds to several tens of picoseconds, depending on the gas species [21].

2.5 Ionization

As the laser intensity is increased further, the gas medium begins to ionize and plasma effects quickly come to dominate the index of refraction. The cold plasma approximation used here assumes minimal ion heating. This is a good approximation if the electron-ion collision time is much longer than the laser pulse width, which is the case for ~100 fs pulses and atmospheric density gases. Then the charge density and current source terms may be written

$$\rho_e = -eN_e + qN_i \tag{2.11}$$

$$\vec{J}_e = -eN_e\vec{v}_e \tag{2.12}$$

where the ion background with charge q and density N_i is stationary and ensures charge conservation. The electron velocity can be found from Newton's law, including a damping term v_e due to electron-ion collisions and assuming a monochromatic electric field $\vec{E}(\vec{r},t) = \vec{E}(\vec{r})e^{-i\omega t}$.

$$\vec{v}_e = -\frac{ie\vec{E}}{m_e(\omega + i\nu_e)} \tag{2.13}$$

The index of refraction of the cold plasma is then found to be

$$n^2 = 1 - \frac{{\omega_p}^2}{\omega(\omega + i\nu_e)} \tag{2.14}$$

$$\omega_p \equiv \sqrt{\frac{4\pi e^2 N_e}{m_e}} \approx 5.64 \times 10^4 \sqrt{N_e} \left[\frac{rad}{s}\right] \tag{2.15}$$

Here ω_p is the plasma frequency with the electron density N_e expressed in cm^{-3}. The electron-electron collision time υ_{ee} for 1 eV electrons at a density of $10^{19}/cm^3$ is on the order of hundreds of femtoseconds. The electron-ion collision time for room temperature ions of the same density is $\tau_{ei} \sim \frac{\tau_{ee}}{10} Z^4$ where Z is the atomic number. Thus the electron-ion collision time is typically long compared to sub-hundred femtosecond pulse durations and $\frac{{\omega_p}^2}{\omega^2} << 1$, so that the index of refraction may be approximated as

$$n \approx \sqrt{1 - \frac{{\omega_p}^2}{\omega^2}} \approx 1 - \frac{N_e}{2N_{cr}} \tag{2.16}$$

$$N_{cr}\left[cm^{-3}\right] \equiv \frac{m_e\omega^2}{4\pi e^2} \approx 1.1 \times 10^{21} \left(\frac{\mu m}{\lambda}\right)^2 \tag{2.17}$$

To calculate the plasma index of refraction as a function of incident laser intensity, it is necessary to quantify the electron density as a function of intensity starting in a neutral gas. The ionization rate w of an atom due to an external field can be found from

$$N_e = N_a \int w(t)dt \tag{2.18}$$

for an ensemble of N_a atoms, neglecting recombination which occurs on hundreds of picoseconds to nanosecond timescales.

In the early 1960s it was thought that two competing ionization mechanisms existed, with very different dependencies on the electric field strength. In the multiphoton mechanism, an electron transitions from the ground state of an atom into the continuum by simultaneous absorption of at least K photons from the external field, each with energy $\hbar\omega < U_0$ where U_0 is the binding energy of the atom.

$$K = {}^{U_0}\!/_{\hbar\omega} + 1 \tag{2.19}$$

In the tunneling mechanism, the external field distorts the Coulomb potential of the atom to such an extent that it is possible for the electron to tunnel through the potential barrier into the continuum. See Figure 2.3 for an illustration of the two ionization mechanisms.

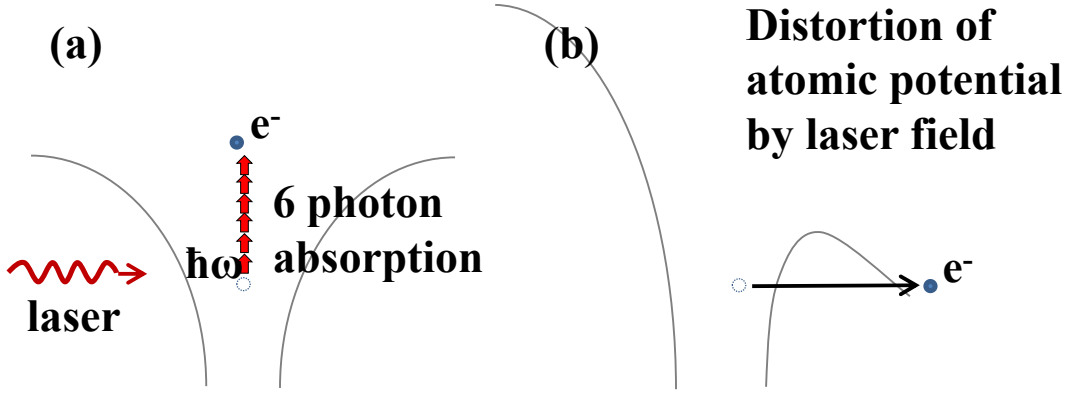

Figure 2.3(a) Direct multiphoton ionization. (b) Tunnel ionization

Keldysh demonstrated that the two ionization mechanisms are different limits of the same process [22]. By approximating the initial state as an s-orbital and the final state as a free electron in a monochromatic external field, with no contribution from the Coulomb potential of the parent atom, Keldysh was able to write a general ionization rate equation

which asymptotically approaches the multiphoton limit in one direction and the tunneling limit in the other. Rewritten, Keldysh's solutions may be expressed as [23]

$$\mathrm{w}(E,\omega) \propto \begin{cases} \exp\left[\dfrac{-2}{3F}\left(1-\dfrac{1}{10}(1-1/3\,\xi^2)\gamma_K{}^2\right)\right] & \gamma_K << 1 \\ K^{2K}\mathrm{I}^K & \gamma_K >> 1 \end{cases} \tag{2.20}$$

$$F \equiv \frac{m_e e\hbar}{(2m_e U_0)^{3/2}} E \tag{2.21}$$

$$\gamma_K \equiv \frac{\omega\sqrt{2m_e U_0}}{eE} = \frac{\tau_T}{\tau_L} \tag{2.22}$$

where F is the reduced field and γ_K is the Keldysh parameter and describes the ratio of the ionization potential to the field strength as a function of external field frequency. Alternatively, γ_K may be expressed as the ratio of the time over which a tunneling event occurs compared to the oscillating electric field period. ξ represents the ellipticity of the field and is defined according to

$$\vec{E}(t) = E\cos(\omega t)\vec{e}_x + \xi E\sin(\omega t)\vec{e}_y \tag{2.23}$$

The asymptotes of Eq (2.20) are plotted in Figure 2.4 as a function of the field strength E. Dotted lines indicate regions where γ_K ~1 and neither limit applies.

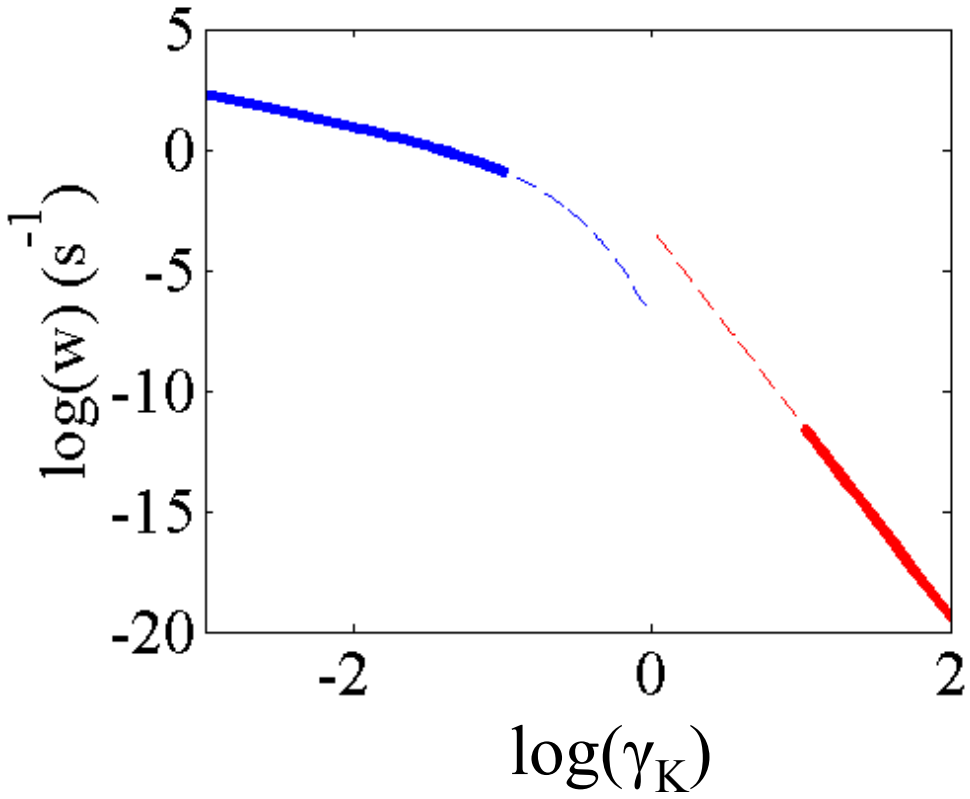

Figure 2.4 Multiphoton ionization limit plotted for $\gamma_K \geq 10$ (red) and tunneling ionization limit for $\gamma_K \leq 0.1$ (blue) for a toy atom. Input parameters are: U_0=15 eV, incident light at 800nm, 5 photon ionization. The dashed lines represent regions where $\gamma_K \sim 1$.

According to Eq (2.20), at low field strengths the external field does not strongly distort the atomic Coulomb potential and ionization occurs solely over the multiphoton pathway with no tunneling contribution. In this case, the ionization rate is proportional to the field intensity raised to the K^{th} power. In the limit of high field strengths tunneling ionization processes dominate and the ionization rate is exponential as the inverse of the square root of intensity.

To accurately express the pre-factors for Eq (2.20) the final state must include the atomic contribution to the potential. The Coulomb potential was first included in the last papers of two extensive studies on ionization of atoms in oscillating electric fields by

Perelomov, Popov, and Terent'ev [24] and Nikishov and Ritus [25]. Unfortunately, neither solution is applicable to the multiphoton limit. In the tunneling limit, $\gamma_K << 1$, the ionization rate for any state $|lm\rangle$ with orbital angular momentum l, magnetic quantum number m, and ionization potential U_0 in a linearly polarized external field E is

$$w_{lm}(E,\omega) = \frac{4\hbar^2 U_0}{m_e e^4} |C_{kl}|^2 \left(\frac{6}{\pi}\right)^{1/2} (2l+1) \frac{(l+m)!}{2^m m!(l-m)!} \left(\frac{2}{F}\right)^{2n^* - m - 3/2} \exp\left[\frac{-2}{3F}\left(1 - \frac{\gamma_K{}^2}{10} + \ldots\right)\right] \tag{2.24}$$

$$n^* \equiv \frac{Ze^2}{\hbar}\sqrt{\frac{m_e}{2U_0}} \tag{2.25}$$

F and γ_K are defined in eqs. (2.21) and (2.22). Z is the ion charge state, m_e is the electron mass which should not be confused with the magnetic quantum number m. The coefficients C_{kl} come from the definition of the asymptotic wave function of a free electron at $r >> (2U_0)^{-1/2}$ and may be found in tables of atomic properties, see for instance [26]. For s-states the Hartree approximation [27] gives the coefficients to within 10%

$$|C_{kl}|^2 = \frac{2^{2n^*-2}}{n^*(n^*+l)!(n^*-l-1)!} \tag{2.26}$$

In the case of circular polarization Eq (2.24) should be multiplied by $\sqrt{\frac{\pi}{3F(n^*)^3}}$ [28] [29]. The general elliptical case is discussed in [23] and references contained therein. In general, the ionization rate may be expressed as a product of the rate in a short-range potential, following the development of Keldysh, times a correction factor which takes into account the Coulomb potential contribution.

A more accurate but more numerically intensive development of the ionization rate was done by Faisal [30] and Reiss [31–33] and is known as the Keldysh, Faisal and Reiss theory. Numerical calculations based on this development are often used in fitting experimental data.

For all of the above work, the tunneling limit ionization rate was derived using the electric dipole approximation, which neglects any contribution due to the magnetic field and consequently is invalid in the relativistic limit. Recently the validity of the theories at extremely high field intensities was evaluated by Reiss [34] who found that for $\gamma_K > \frac{1}{2}\sqrt{\frac{U_0}{\omega c}}$ (in atomic units) magnetic field effects become appreciable. More recent work on extending the PPT development to the relativistic regime for hydrogen-like ions can be found in refs [35] and [36]. The analytically derived relativistic ionization rates are compared to one another, but not benchmarked against experimental data or simulations, so it is difficult to evaluate how accurate the many approximations are for representing the relativistic regime.

An analytic expression for the pre-factors in the multiphoton limit was found relatively recently by Popruzhenko et al [37]. The authors use a single-active electron approximation in the quasi-classical limit to calculate electron trajectories. They find the Coulomb correction factor $Q \simeq \left(\frac{2}{F}\right)^{2n^*}\left(1+\frac{2\kappa}{2.72}\right)^{-2n^*}$ This is compared to the tunnel limit calculations where $Q=\left(\frac{2}{F}\right)^{2n^*}$. The ionization rate in the limit $\gamma_K >> 1$ simplifies to

$$\mathrm{w} = \frac{2\hbar^2 U_0}{m_e e^4} 2^{2n^*} \mid C_{kl} \mid^2 2.72^{N_m+2n^*} K^{2N_m+2n^*-3/2} F^{2N_m} \tag{2.27}$$

where $N_m = K+1$ is the minimum number of photons required for ionization. Popruzhenko *et al*. [37] benchmark the general form of their solution, for all γ_K, against exact numerical results using both the Floquet method and the time-dependent Schrodinger equation (TDSE). The results are in good agreement with the analytic equation, which is reasonably complicated and not presented here.

Ultimately, the experimentally measured ionization rate in the multiphoton limit is difficult to fit without recourse to simulations, due to effects beyond the simple model including resonant and multi-electron effects. In many atoms, especially atoms with high atomic numbers, resonant multiphoton ionization (REMPI) is the dominant ionization pathway. In non-resonant multiphoton ionization each absorbed photon moves the electron into a higher energy virtual state, which may exist according to the uncertainty principle for a time Δt where $\Delta t \Delta E \geq \frac{\hbar}{2}$. Within Δt the electron must absorb another photon or decay back to its original (real) state. However, it is possible that a real excited state of the atom exists an integer number of photons from the initial state. In this case, the electron will reside in the excited state for the state lifetime, which is very long compared to the lifetime of the virtual state and the ionization timescale. With the excited state populated, n fewer photons are required for direct multiphoton from the excited state. The ionization rate through this resonant pathway is proportional to I^{K-n} and the resonant multiphoton ionization channel is more probable than ionization directly from the initial state. See Figure 2.5 for an illustration of the process.

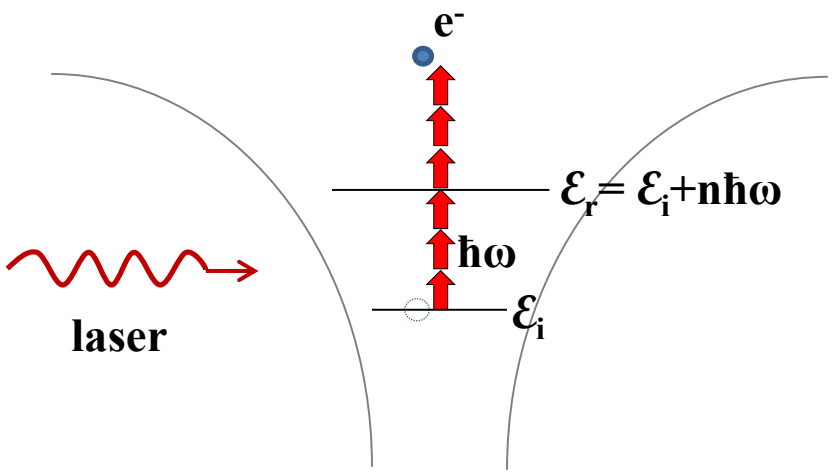

Figure 2.5 Resonant multiphoton ionization

For a monochromatic or narrow bandwidth external field, it is highly unlikely that the incident photons will be exactly resonant with an unperturbed atomic state. However, the oscillating laser field interacts with the atomic field to shift the energies of the atomic states. This Stark shift can be viewed as an induced polarizability of the atom by the external field. Using perturbation theory, the Stark shift is shown to be proportional to the incident intensity [38,39]. The shift of the n^{th} state is

$$\Delta\mathcal{E}_n = \frac{e^2 \mathrm{E}^2}{4} \sum_m \left(\frac{2\omega_{nm} \mid \mu_{nm} \mid^2}{\omega_{nm}{}^2 - \omega^2} \right) \tag{2.28}$$

$\omega_{nm}=\omega_n-\omega_m$ and μ_{nm} is the dipole operator between states n and m, with a sum over all other states m of the atom. For an ultrashort pulse with a Gaussian temporal profile intensities vary from zero to I_{max} over the envelope of the pulse. Furthermore, the bandwidth of the pulse tends to be relatively broad. For instance, a Ti:Sapphire pulse with 25 nm of bandwidth contains photons with energies spanning 1.59 to 1.53 eV. Between the broad energy range of the pulse and the large range of Stark shifts seen by

the atomic levels, it is much more probable that an atomic system investigated with an ultrashort pulse will pass through at least one resonance. In heavy atoms with closely spaced atomic levels, there may be many resonances. In addition to the shift of a state induced by the atomic field-external field interaction, there is also a broadening of the energy level which is proportional to intensity. For the simple case of a monochromatic laser, an approximate form for the ionization rate of a resonant system was found by Kontova and Terent'ev [40]

$$\mathrm{w}_{irf} \propto F^{2N_m} \frac{\Gamma_r^{\,2}}{((\omega_i + \Delta\mathcal{E}_i) - (\omega_r + \Delta\mathcal{E}_r) - N_m\omega)^2 + \Gamma_r^{\,2}} \tag{2.29}$$

Γ_r is the width of the resonant state and is the sum of the natural width of the state and the Stark broadening factor. Far from resonance, this reduces to the direct multiphoton ionization rate Eq (2.27). For ground or low-lying states, the Stark shift tends to be small due to the small induced dipole moment of tightly bound states. If the initial state of the atom is the ground state, the Stark shift $\Delta\mathcal{E}_i$ is negligible. In the other extreme, extremely high-lying states may have Stark shifts essentially equal to the energy gain of a free electron in the oscillating field, $\Delta\mathcal{E} = \frac{e^2E^2}{4m\omega^2}$ the ponderomotive energy. As the external field intensity shifts states toward a resonance, the ionization rate is no longer dominated by F^{2N_m}. Locally, the power of intensity is equal to the slope of the ionization rate plotted against the logarithm of intensity and will appear to take on every value less than N_m as the intensity is scanned through a resonance. See Figure 2.6. Thus it is possible in multiphoton resonant ionization for the intensity dependence of the ionization rate to be very different from the non-resonant limit over a narrow intensity range.

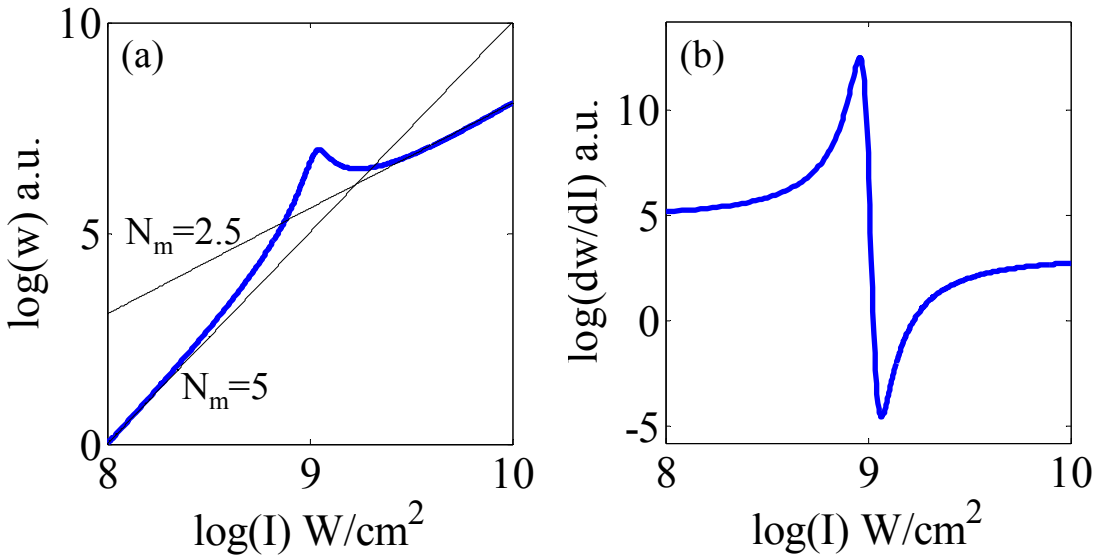

Figure 2.6 (a) Resonant multiphoton ionization rate (plotted without pre-factors) for detuning $\Delta=\mathcal{E}_i-\mathcal{E}_r-4\hbar\omega$ and Stark shift $\Delta v=40$cm/GW. In the absence of the resonance, the ionization rate is proportional to five photon absorption (field intensity I^5). Due to the resonance, the local dependence of the intensity exponent (b) ranges from 12.5 to -4.5.

In practice, more than one atomic state may be resonant or the external field may not be monochromatic. Additionally, it is possible to remove more than one electron at a time in multiphoton ionization. In this case, numerical simulations are necessary to correctly predict the ionization rates. TDSE Codes such as STRFLO [41] and QPROP [42] are publically available for numerical solution of the interaction of electromagnetic fields with atoms and ions, including resonant phenomena. Such simulations are computationally intensive for complex atoms but often simple cases are solved to benchmark experimental data or new theoretical approximations for ionization rates.

2.6 Nonlinear plasma response

After ionization, there are several nonlinear contributions to the index of refraction due to the field of a high intensity ultrashort laser pulse interacting with the free electrons. As long as free electrons are present, the generally peaked profile of the laser

focus causes electrons to be pushed to regions of lower intensity. This ponderomotive force can be described in the as follows: in a uniform electric field, an electron begins with some initial velocity and position, arbitrarily chosen to be v=0 and r=0 zero, and moves under the influence of the Lorentz force some distance r over one half cycle of the laser where the velocity again is equal to zero. The particle trajectory then switches direction and the exact inverse of the initial motion occurs, returning the electron to r=0 with v=0 over a full laser cycle. No net energy is transferred from the laser field to the electron. However, in a field with a spatial profile peaked on axis, $E(r=0)>E(r)$ and return motion of the electron takes place in a region of weaker field than the initial acceleration. The result averaged over a full cycle is a net force in the direction of weaker field. See Figure 2.7

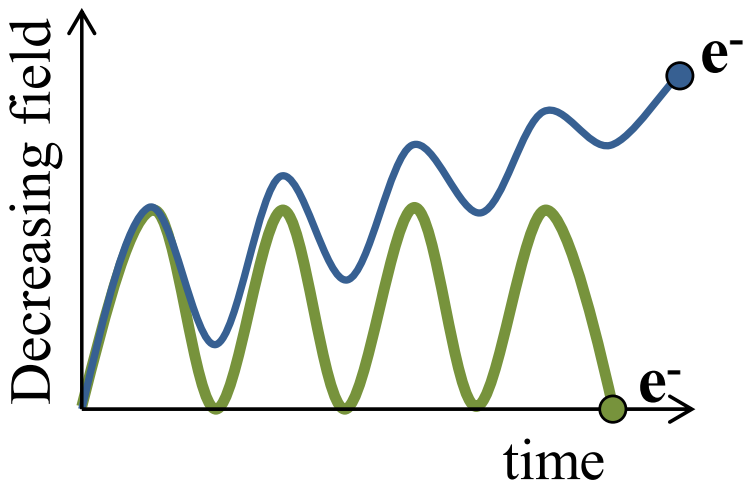

Figure 2.7 Electron trajectory in a constant field (green) and a field with gradient in the direction indicated (blue). The ponderomotive force pushes the electron in the direction of decreasing field strength.

More formally, the equation of motion in the nonrelativistic limit for a plane wave can be written

$$\ddot{\vec{r}}(t) = -\,{}^{e}\!/_{m_e}\left[\vec{E}(\vec{r})\cos(\omega t) + \vec{v}\times\vec{B}(\vec{r})\sin\omega t\right] \tag{2.30}$$

The spatial coordinate *r* may be split into a slow drift motion r_0 and a fast oscillatory motion r_1 which time averages to zero, so that $r=r_0+r_1$. In the limit of a uniform field, $r_0=0$. A Taylor expansion around r_0 to first order gives

$$\ddot{\vec{r}}_0 + \ddot{\vec{r}}_1 = {}^{e}\!/_{m_e}\left[\left(\vec{E}_0(\vec{r}_0) + \vec{r}_1 \cdot \nabla \vec{E}_0(\vec{r}_0)\right)\cos(\omega t) + (\dot{\vec{r}}_0 + \dot{\vec{r}}_1) \times \left(\vec{B}_0(\vec{r}_0) + \vec{r}_1 \cdot \nabla \vec{B}_0(\vec{r}_0)\right)\sin \omega t\right] \tag{2.31}$$

In the non-relativistic limit, contributions from the magnetic field are higher order effects. Time averaging the equation to first order over one period removes $\ddot{\vec{r}}_1$ and $eE_0\cos(\omega t)$ leaving the first order equation for the slow component.

$$\ddot{\vec{r}}_0 = {}^{e}\!/_{m_e}\left\langle (\vec{r}_1 \cdot \nabla)\vec{E}_0(\vec{r}_0)\cos(\omega t) + \dot{\vec{r}}_1 \times \vec{B}_0(\vec{r}_0)\sin \omega t\right\rangle_t \tag{2.32}$$

To find an equation for $\vec{r}_1$, examine the zeroth order solution for the fast component of Eq (2.31).

$$\ddot{\vec{r}}_1 \approx {}^{e}\!/_{m_e} E_0 \cos(\omega t) \tag{2.33}$$

Then $\vec{r}_1 \approx -\frac{e}{\omega^2 m_e}\vec{E}_0(\vec{r}_0)\cos(\omega t)$ and $\dot{\vec{r}}_1 \approx \frac{e}{\omega m_e}\vec{E}_0(\vec{r}_0)\sin(\omega t)$. Taking the time average and using the solution for $\vec{r}_1$ and $\vec{B}_0 = -\frac{1}{\omega}\nabla \times \vec{E}_0$ from Maxwell's equations Eq (2.32) may be simplified to

$$\ddot{\vec{r}}_0 = -\frac{e^2}{4m_e{}^2\omega^2}\nabla |\vec{E}_0|^2 \tag{2.34}$$

Finally, the solution for r_0 can be rewritten in terms of force so that

$$\vec{F}_p = -\frac{e^2}{4\omega^2 m_e}\nabla |\vec{E}_0|^2 \tag{2.35}$$

From the cold fluid equations, the variation in electron density can be found [43]

$$\delta N_e = \frac{N_0 c^2}{\omega_p}\int_0^t \sin[\omega_p(t-t')]\nabla^2\left[\frac{1}{2}a_0{}^2(\vec{r},t')\right]dt' \tag{2.36}$$

$$a_0 \equiv \frac{eE_0}{m_e\omega c} = \sqrt{\frac{I\lambda^2[\mu m]}{1.37\times10^{18}}} \tag{2.37}$$

a_0 is the normalized vector potential. Typically for $a_0 \geq 0.1$ relativistic effects must be included. The effect of the ponderomotive force is to decrease the electron density in the high intensity region of the beam, introducing a gradient in the plasma index of refraction proportional to the gradient of the pulse intensity.

Another nonlinear effect encountered when high intensities interact with free electrons stems from the relativistic mass dependence on electron velocity, which affects the plasma refractive index. In the relativistic regime, the plasma index of refraction, for negligible collisions, may be rewritten as [44]

$$n^2 \approx 1 - \frac{\omega_p{}^2}{\langle\gamma\rangle_t\,\omega^2} \tag{2.38}$$

$$\gamma(t) \equiv \frac{1}{\sqrt{1-\beta^2}} = \frac{1}{\sqrt{1-\frac{v(t)^2}{c^2}}} \tag{2.39}$$

γ is the relativistic correction factor.

2.7 Summary

There are a rich variety of processes where nonlinear phenomena in a gas or plasma occur. This dissertation will explore several of the intensity regimes discussed above. Chapter 2 is dedicated to a diagnostic used to measure the ultrafast pump-induced transient refractive index in either a gas or plasma. Chapter 3 discusses the lasers used for the experiments in later chapters. The last chapters are descriptions of experiments which take advantage of, or are used to study, nonlinear optical processes in gases. Chapter 4 describes laser heating of a long nitrogen plasma column in an attempt to create a controllable population inversion between molecular nitrogen states. Chapter 5 covers measurements concerning fast collisional excitation and multiphoton resonant ionization in a singly ionized xenon plasma. Chapter 6 contains preliminary results in an experiment designed to measure the difference between the ponderomotive change in the plasma index of refraction and the inertial mass contribution in a slightly relativistic laser pulse.

Chapter 3 : Single shot spectral interferometry for measurement of ultrafast dynamics in laser-matter interactions

3.1 Introduction to SSSI

To measure the change in index of refraction of a gas or plasma induced by a strong laser pulse, a weak probe pulse traverses the perturbed region and acquires a phase $\varphi = \varphi_0 + \Delta\varphi$ where φ_0 is the phase due to the gas in the absence of the perturbing laser pulse. An identical copy of the probe pulse which passes through a region of the gas where there is no change in the refractive index is used as a reference with phase φ_0. Then the phase shift can be extracted via interference of the reference and probe pulses. The probe pulse intensity must be small enough that it does not further perturb the interaction medium. In experiments suitable for probing via spatial interferometry, the transverse region where the index of refraction is perturbed is typically much smaller than the probe beam diameter, and a portion of the probe outside the interaction region may be used as a reference. Alternatively, a copy of the probe which traverses a spatial region lacking the index of refraction perturbation may be used as a reference. In other cases, the interaction region is as large as the probe beam, and it is not feasible to use a portion of the probe as a reference. Instead, the probe is copied using a Michelson interferometer with a glass plate in one arm to compensate for dispersion due to the beam splitter and the reference copy traverses the interaction region before the strong perturbing pulse arrives. Reference and probe are thus separated temporally but traverse exactly the same spatial region allowing information to be extracted via temporal

interferometry. To recombine the temporally separated pulses for interference, an imaging spectrometer is used to increase the reference and probe pulse duration. The maximum probe and reference separation time for which interference fringes may still be obtained is dictated by the grating dispersion. For a diffraction grating at normal incidence, the maximum pulse separation is $\tau \approx \frac{D}{c}\sin(\theta)$ where D is the beam diameter on the diffraction grating and θ is the wavelength-dependent first order diffraction angle. See Figure 3.1

Imaging the interaction region to the spectrometer slit provides spatial information about the index of refraction profile along the slit dimension. Ideally, the pump focal spot is axially symmetric and the interaction medium is approximately isotropic, so that one spatial dimension allows 2D reconstruction of the index of refraction profile. The spectral interference signal without pump excitation of the medium is given by

$$\left| \mathrm{E}_{\mathrm{pr}}(\omega) + \mathrm{E}_{\mathrm{ref}}(\omega) \right|^2 = 2\left| \mathrm{E}_{\mathrm{pr}}(\omega) \right|^2 \left(1 + 1\cos\,\omega\tau\right) e^{i\theta} \tag{3.1}$$

When the probe passes through the pump-excited region the spectral interference is given by

$$\begin{aligned} &\left| \mathrm{E}_{\mathrm{pr}}(\omega) + \mathrm{E}_{\mathrm{ref}}(\omega) \right|^2 = \left| \mathrm{E}_{\mathrm{pr}}(\omega) \right|^2 \times \\ &\left\{ 1 + \exp\left[2\Delta\mathrm{k}(\omega,T)\,\omega\,\mathrm{r}/c \right] + 2\exp\left[\Delta\mathrm{k}(\omega,T)\,\omega\,\mathrm{r}/c \right] \cos\left[\omega\left(\tau - \Delta\mathrm{n}(\omega,T)\,r/c \right) \right] \right\} \end{aligned} \tag{3.2}$$

where the change in the complex refractive index $\Delta n_c(\omega,T) = \Delta n(\omega,T) - i\Delta k(\omega,T)$ and T is the separation between the strong pump and the probe [45].

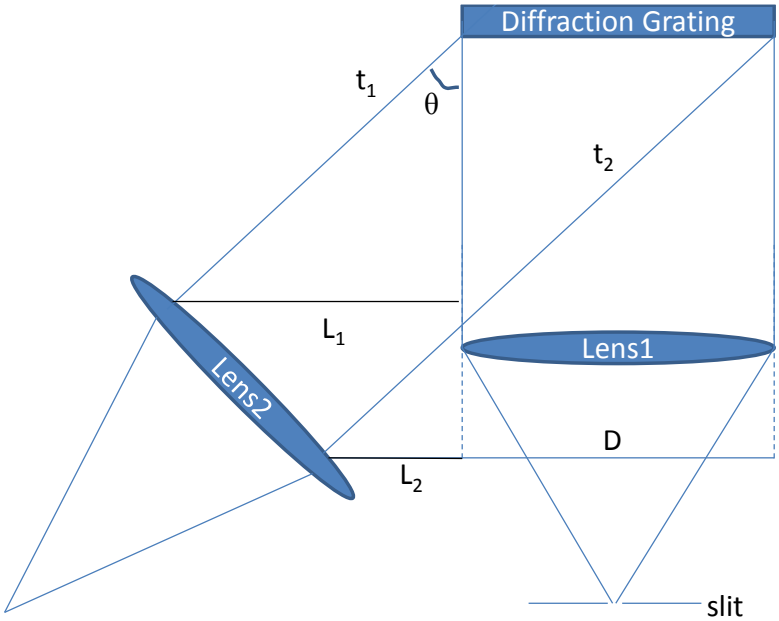

$\tau=abs(t_1-t_2)=abs(L_1/c\ sin(\theta)-(L_2+D)/c\ sin(\theta))$
$\approx D/c\ sin(\theta)$ for $L_1 - L_2 << D$

Figure 3.1 Diagram of imaging spectrometer with derivation of maximum probe/reference pulse separation for which temporal overlap is achieved.

The phase shift imposed on the probe pulse is related to the perturbation of the interaction medium according to $\Delta\varphi(r) = k\int \Delta n(r,z)dz$ where k is the laser wavenumber and $\Delta n(r,z)$ is the pump-induced shift in index of refraction for a probe propagating in the z-direction. For a sufficiently thin sample of interaction length L, where $L/z_0 << 1$ (z_0 is the minimum of the Rayleigh lengths of the pump and probe beams), and barring pump energy depletion, the integral can be written as

$$\Delta\phi(r) = k\Delta n(r)L \qquad (3.3).$$

where r is the coordinate transverse to the propagation direction and parallel to the slit.

To obtain temporal information about the laser-matter interaction, two techniques are commonly used. First, the time delay between the probe and pump arrival at the interaction region may be changed from one laser shot to the next. This multi-shot technique works well for highly repeatable processes, in which the temporal and spatial evolution of the medium after the pump pulse is identical for every laser pulse. For high power laser systems with large shot-to-shot energy fluctuations and highly nonlinear processes, the shot-to-shot reproducibility of the interaction is often poor. When single shot temporal information is desirable, it is possible to strongly chirp the probe pulse. For a probe with positive chirp (the direction of chirp naturally imposed on a broad bandwidth laser pulse passing through glass) low frequencies will pass through the interaction region at shorter time delays relative to the pump pulse arrival time than high frequencies. The temporal evolution of the index of refraction is thus encoded on the probe pulse as a function of frequency, which may be mapped to time. The temporal window accessible in a single-shot corresponds to the chirped probe pulse duration. Because the temporal resolution is ultimately restricted by the bandwidth of the probe pulse, it is desirable to have a broadband spectrum.

Time-resolved frequency domain interferometry has been done by many groups using a wide variety of probe pulse sources, including frequency doubling the strong pump pulse [46] [47] linearly chirping the pump pulse and splitting off a small probe [48], splitting off a probe before compression in a chirped pulse amplifier system [49], and using a small portion of the pump pulse to generate supercontinuum [50,51]. Of the available methods, the last is used in this work. A probe beam with 100 μJ of energy is focused into a xenon gas cell pressurized to two atmospheres, generating supercontinuum

with a 350 nm bandwidth. The fundamental light near 800 nm is rejected and the spectral range from 480 to 700 nm is chirped to form a 4 ps probe pulse. A Michelson interferometer copies the probe pulse to generate a reference pulse which precedes the probe by 2.5 ps. The supercontinuum probe and reference beams are combined with the pump beam using a dichroic mirror and co-propagate through a gas flow tube used to control the interaction length. The interaction region is imaged to the spectrometer slit. This technique is referred to as SSSI (supercontinuum single-shot interferometry).

3.2 Time to Space Mapping

The probe for single-shot spectral interferometry is a large bandwidth probe pulse dispersed by passage through some length of glass. Due to normal dispersion, the high frequency components of the probe traverse the glass more slowly than the low frequency components, resulting in a 'chirped' pulse where redder probe wavelengths arrive at the interaction region earlier than bluer probe wavelengths. The first work mapping temporal evolution of a nonlinear optical phenomenon onto probe frequency was done without interferometry, to follow the ionization-induced refraction of an ultrashort pulse in helium [52].

To quantitatively associate frequency and time, one must know the amount of chirp applied to the probe beam. To first order, the chirp may be considered linear so that $\omega(t) = \omega_0 + \kappa t$ where κ is the chirp parameter [49], a measure of how fast the probe frequency changes. In terms of experimentally measurable variables

$$\kappa = 2\beta\left[1 + 2\ln 2 / \left(\beta^2 \Delta\omega^4\right)\right] \tag{3.4}$$

can be derived from the inverse Fourier transform of *E(ω)* with linear chirp and a Gaussian spectral envelope where $\beta = \frac{1}{2}\frac{d\varphi^2}{d^2\omega}\Big|_{\omega_0}$ is the group delay dispersion (GDD) of the probe pulse and $\Delta\omega$ is the probe spectral full width at half maximum (FWHM) [53,54].

The direct time to frequency mapping suffers from an intrinsic time resolution limitation $\Delta t_{res} = \left(\tau_c^{\,4} + \kappa^2\right)^{1/4}$ where τ_c is the $1/e^2$ temporal coherence time of the probe pulse and κ is the linear chirp parameter as above [55]. In the limit of little or no chirp, $\kappa << \tau_c^{\,2}$, this reduces to the expected limit where the time resolution is dictated by the probe pulse duration $\Delta t_{res} \sim \tau_c$. In the opposite limit of a highly chirped pulse, $\kappa >> \tau_c^{\,2}$, the time to frequency mapping is limited by the inability to isolate a single frequency component in an oscillating signal which is rapidly changing frequency. Here $\Delta t_{res} \sim \sqrt{\kappa}$.

3.3 Fourier Analysis

To achieve a large temporal window the probe pulse is typically heavily chirped, resulting in poor temporal resolution using the direct mapping technique. Another method of analysis that circumvents direct mapping is necessary to fully utilize the bandwidth of the chirped pulse. The time domain probe electric field modified by the interaction being studied is

$$E_{pr}(t) = E_r(t-\tau)e^{i\,\Delta\varphi(t-\tau)} \tag{3.5}$$

The unmodified probe pulse is assumed to be an exact, time delayed copy of the reference pulse $E_r(t-\tau) = E_{pr0}(t)$. Using Fourier transforms, the temporal phase shift $\Delta\varphi(t-\tau)$ may be expressed as

$$\Delta\varphi(t-\tau) = Im\{\ln\left[\frac{F^{-1}\left(\left|E_{pr}(\omega)\right|e^{i\varphi_0+i\Delta\varphi(\omega)}\right)}{F^{-1}\left(\left|E_r(\omega)\right|e^{i\varphi_0}\right)}\right]\} \tag{3.6}$$

Where F^{-1} is the inverse Fourier transform, $|E_r(\omega)|$ is the reference spectral magnitude, $|E_{pr}(\omega)|$ is the modified spectral magnitude, $\varphi_0(\omega)$ is the spectral phase of the reference pulse, and $\Delta\varphi(\omega)$ is the induced spectral phase shift due to a change in the index of refraction between the probe and reference arrival time [54,56]. In order to extract the time-domain phase shift, which contains information about the material response, it is necessary to measure four quantities: $|E_r(\omega)|$, $\varphi_0(\omega)$, $|E_{pr}(\omega)|$, and $\Delta\varphi(\omega)$. $|E_r(\omega)|$ is measured by blocking the pump pulse. The reference phase $\varphi_0(\omega)$ can be expressed as a Taylor expansion about the central frequency ω_0 of the pulse.

$$\phi_0(\omega) \simeq \beta_0 + \beta_1(\omega_0)(\omega-\omega_0) + \beta_2(\omega_0)(\omega-\omega_0)^2 + \beta_3(\omega_0)(\omega-\omega_0)^3 + \ldots \tag{3.7}$$

where $\beta_n = \frac{1}{n!}\frac{\partial^n\phi}{\partial\omega^n}$. The reference phase is measured by observing the frequency at which an amplitude change induced by a short pump pulse occurs as a function of time delay between the pump and reference pulse $\omega(\tau)$. If the reference GDD is large, $\omega(\tau)$ is single valued and can be inverted to find

$$\tau(\omega-\omega_0) = \phi'(\omega-\omega_0) = \beta_1(\omega_0) + \beta_2(\omega_0)(\omega-\omega_0) + \frac{1}{2}\beta_3(\omega_0)(\omega-\omega_0)^2 + \ldots \tag{3.8}$$

which is fit to an n-degree polynomial to find all factors up to β_{n+1}. Typically, the change in phase when the fourth order dispersion is included is small and only terms up to β_3 are necessary to reliably reproduce the reference phase, although the necessary order will vary depending on the method used to chirp the pulse. See Figure 3.2 for illustration of the dispersion measurement. $E_{pr}(\omega)$ and $\Delta\varphi(\omega)$ are extracted directly from the interferograms using Fourier fringe analysis [57].

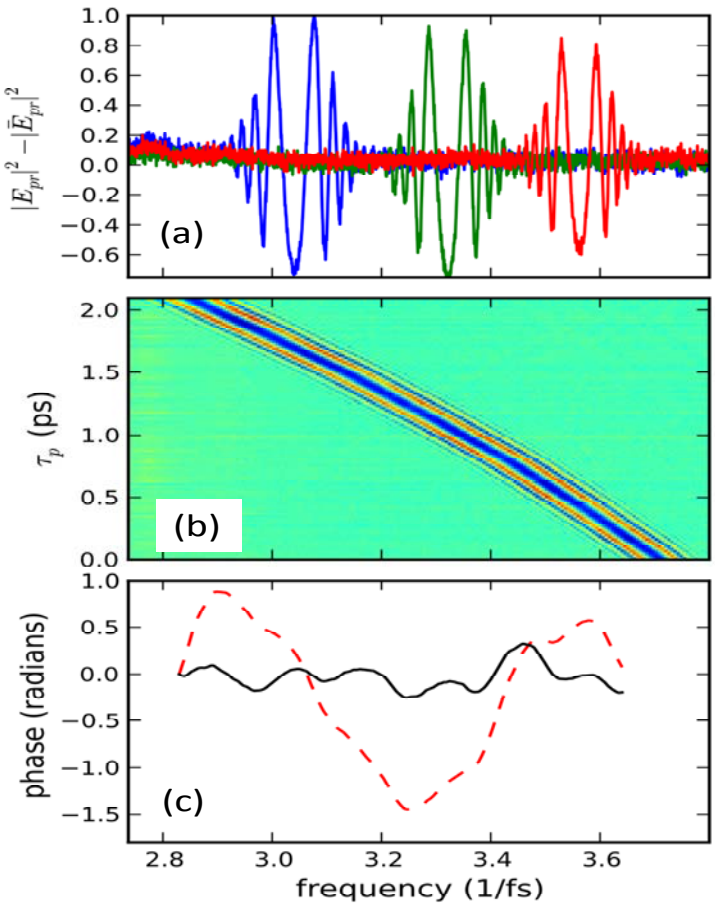

Figure 3.2 (a) One dimensional lineout of difference between unmodified probe intensity profile and probe intensity profile with a nonlinear contribution driven by a pump pulse. Red: time delay between pump and probe T=1.0ps, Green: T=0ps, Blue T=-1.0ps. (b) Two-dimensional array of intensity difference lineouts as a function of T. (c) Integrated residuals from fit to T(ω) for first order (red) and second order (black) polynomials

The time-resolved phase shift maps are very sensitive to the measured value of the reference phase $\varphi_0(\omega)$. In earlier implementations of SSSI, only the second order dispersion term β_2 was used in the Fourier analysis. Figure 3.3 shows a one-dimensional map of phase shift as a function of time during the ionization of xenon. The temporal behavior found using only group delay dispersion is considerably different from the true temporal behavior, found using higher order dispersion terms. Additionally, a 5% error in β_2 is enough to slightly affect the amplitude of the small positive bump, arising from the Kerr nonlinearity, measured prior to ionization.

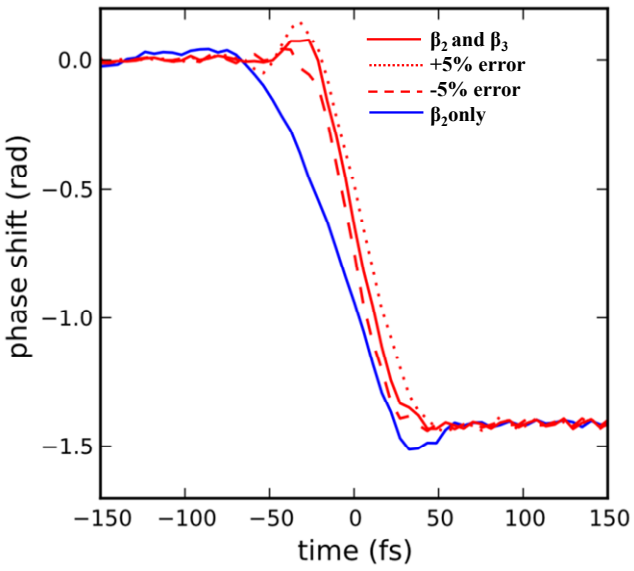

Figure 3.3 Extracted phase shift as a function of time during ionization of xenon with (red) and without (blue) higher order dispersion terms included in $\varphi_0(\omega)$. It is necessary to include the third order dispersion term to correctly extract temporal behavior. Small errors in measurement of the second order dispersion do not strongly alter temporal shape, but do change the magnitude of the small positive phase shift peak corresponding to the Kerr nonlinearity before ionization (red dashed and dotted lines).

The temporal resolution obtainable is no longer limited by large probe pulse chirp, as compared to the direct mapping method. Instead, the temporal resolution is dictated by the convolution of the spectrometer spectral resolution and the probe pulse chirp. Two

neighboring probe frequencies separated by the spectrometer resolution will traverse the interaction region at the speed of light in the medium. The temporal separation of the two neighboring frequencies is dictated by the Fourier transform of the spectral phase of the probe pulse $\varphi=\varphi_0+\beta_1(\omega-\omega_0)+ \beta_2(\omega-\omega_0)^2+ \beta_3(\omega-\omega_0)^3 +\ldots$ and determines the temporal resolution of the system. If the spectrometer resolution is fine enough, as it typically is, the temporal resolution is further limited by the pulse bandwidth $\Delta t = \frac{2\pi}{\Delta\omega}$ where $\Delta\omega$ is the full width at half maximum of the probe spectrum.

3.4 Implementation

There are upper and lower limits on the allowable probe and reference temporal separation. To implement the Fourier analysis the detector must have high enough spectral resolution to satisfy the Nyquist sampling limit. That is, the interference fringe spacing $\delta\omega = 2\pi/\tau$ should be at least twice the spectrometer resolution [58]. Generally, the stronger condition on the upper limit for probe and reference temporal spacing is that mentioned in the chapter introduction: the pulses must be close enough that they temporally overlap in the spectrometer (Figure 3.1). There is also a lower limit to the reference and probe separation dictated by the pulse duration τ_p. If $\tau<\tau_p$ portions of the reference pulse will be phase shifted by the interaction being probed, and the assumption of an unmodified reference used to solve for $\Delta\varphi$ is no longer valid.

To ensure axial uniformity, the gas-filled experimental region is limited to a distance smaller than the Rayleigh range of the pump pulse driving the nonlinear processes under study. Thus the pump intensity is approximately constant as a function of the axial coordinate z, assuming pump depletion is negligible. Gas is introduced through a small

tube with a regulator-controlled backing pressure. The tube is located inside a vacuum chamber with vacuum pumps capable of maintaining background pressure of 100 mTorr or less while the pressure in the gas tube is as high as 1 atm and not less than 10 Torr. The pump, probe and reference laser pulses propagate through a laser-drilled hole in the tube several hundred micrometers in diameter and typically 400 micrometers thick. The product $n \cdot L$ where n is the unperturbed gas index of refraction is measured carefully as a function of pressure upstream of the gas tube for every gas species using a continuous wave interferometer. The interaction length L is subsequently extracted, as a function of pressure [59].

Refraction of the supercontinuum probe from transverse index of refraction gradients must be minimized or accounted for in data analysis. From equation (3.6) it is apparent that the measured phase shift as a function of time depends on both spectral amplitude and phase variations in the probe pulse. The non-uniform profile of a laser focus will induce changes in the index of refraction with a transverse gradient. The transverse gradient acts as a lens for the SSSI probe pulse. The resulting curved phase front is converted to amplitude as intensity at the center of the pulse is refracted outward after a Rayleigh range of the effective lens. The perturbed probe amplitude $|E_{pr}(\omega)|$ is recorded as part of the spectral interferograms independent of the probe phase (Eq.(3.2)). However, for the experiments described in following chapters amplitude effects are not included in the phase shift measurements and refraction results in measurement error. For small transverse index of refraction gradients and short interaction lengths, the center of the interaction region is within an effective Rayleigh range of both the front and back interfaces of the gas. In this case, imaging the center of the gas flow tube is sufficient to

eliminate amplitude effects. For stronger transverse index gradients, simulations are done to estimate the difference between the measured phase shift with refraction error and the actual phase shift. See Figure 3.4.

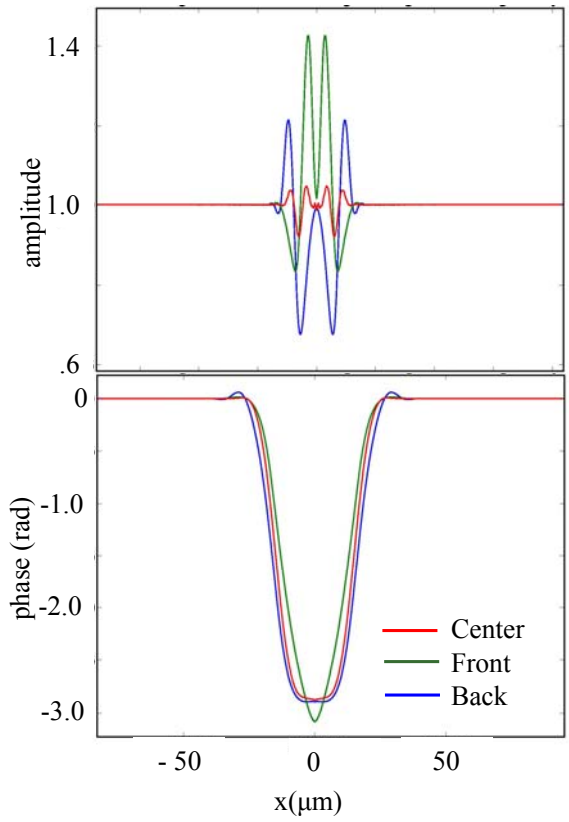

Figure 3.4 Simulated transverse amplitude and phase shift for a system imaging the front, center, and rear of a 400 μm thick, singly ionized xenon plasma at 100 Torr. Even imaging the center of the plasma, a 5% amplitude response is observed.

The beam propagation method is a well-known technique for simulating coherent light propagation. See for example [60,61]. The beam propagation simulation consists of two steps. First, the discrete Fourier transform is applied to the electric field E(x,y,z) to decompose the field into plain waves. These plain waves are propagated a small distance in k-space, and then transformed back into a spatial field. The resulting field propagated in the z-direction can be expressed with one transverse dimension x as

$$\Psi(x,\Delta z)=\frac{1}{2\pi}\int_{k_z\in\Re}\Phi(k_x)\exp\left[k_x x+k_z\Delta z\right]dk_x \tag{3.9}$$

where $\Phi(k_x)=F[\Phi(x,z)]$ is the discrete Fourier transform of the plain-wave phase imposed by a uniform medium $\Phi(x,z)=\exp\left[-ik_0 nz\right]$, n is the index of refraction of the medium, and k_z -the z component of the k vector for each ray- is equal to $nk_0-\frac{{k_x}^2}{nk_0+\sqrt{n^2{k_0}^2-{k_x}^2}}$. Dividing k_z into fast and slow components, Eq. (3.9) becomes

$$\Psi(x,\Delta z)=e^{ink_0\Delta z}\frac{1}{2\pi}\int_{k_z\in\Re}\Phi(k_x)\exp\left[\frac{{k_x}^2}{nk_0+\sqrt{n^2{k_0}^2-{k_x}^2}}\Delta z\right]dk_x \tag{3.10}$$

Eq. (3.10) accounts for propagation through a homogenous medium. Next, the spatial field is multiplied by the phase correction applicable to the region *Δz* due to any difference in the local index of refraction *Δn(x,z)* compared to the background index n. This may include variation of the index of refraction due to nonlinear effects, plasma or traversing imaging optics.

$$\Psi_{\Delta n}(x,\Delta z)=\Psi(x,\Delta z)e^{-ik_0\Delta n(x,z)\Delta z} \tag{3.11}$$

The process is repeated as many times as necessary, and is easily generalizable to two transverse dimensions. The longitudinal step size *Δz* is chosen so that the phase correction for each step remains small. The index of refraction profile can either be adjusted manually until the output phase shift matches the experimentally measured phase shift, or PPT ionization rates can be used with a realistic transverse laser profile and peak intensity to calculate the index profile due to the nonlinear ionization process. The SSSI experimental technique is used extensively in experiments in chapters 5 and 6. Chapter 4 utilizes spatial interferometry rather than temporal interferometry, but

significant refraction in the interferometric probe is compensated using the beam-propagation simulation discussed above.

Chapter 4 : Laser Systems

4.1 Nd:YAG laser

Two laser systems are used for the experiment in this chapter. The first is a seeded Nd:YAG laser operating at 1.064 μm. A new seed laser was installed in the course of this work. The oscillator is a commercial, diode pumped Nd:YVO_4 modelocked laser built by Time Bandwidth Products, model GE-100. The seed laser outputs a 38.0 MHz pulse train of 142.6 picosecond pulses at the design center wavelength of 1064.370 nm
At installation, the power directly out of the oscillator head was 705mW. The pulse train in the oscillator cavity is monitored by a photodiode and the photodiode output is accessible from an SMA connector on the back of the laser case. The output waveform is a 4 V delta-function like pulse train Figure 4.4 (a).

The rest of the laser system is described in detail elsewhere [62]. The pulse train frequency is decreased to 10 Hz before amplification using a pulse slicer unit capable of achieving >850:1 contrast. After the pulse slicer, there are three Nd:YAG amplifiers which altogether are capable of generating up to 800mJ of energy per pulse at 10 Hz. The first amplifier stage is a regenerative amplifier (RGA) operating as a self-filtering unstable resonator [63]. The RGA cavity is closed using a polarizing beamsplitter cube and two stage Pockels cell with a 3 ns rise time, and after amplification the pulse is switched out of the cavity by the same method. The output energy should be kept below 20mJ with the new, longer, oscillator pulse duration to prevent nonlinear self-focusing due to self-phase modulation induced by the amplifier rod and KD*P Pockels cell.

A Faraday isolator is located between the oscillator and RGA and between the RGA and the first power amplifier, which is arranged as a double pass ring. A half-waveplate and TFP after the ring amplifier are used for laser energy control. Due to the laser mode overfilling the ring amplifier crystal, the transverse spatial profile of the pulse exiting the amplifier exhibits strong diffraction rings, which must be removed before the final amplification stage. The beam is fed through a vacuum spatial filter, with a $1/e^2$ radius at the focus of less than 50μm. There are wings on the focused intensity profile of up to 10^{-2} to 10^{-3} times the peak pulse intensity out to a radius of 125μm, which quickly destroy a 200μ diameter diamond pinhole. Therefore, a 300μm pinhole should be placed at the focus to remove higher order modes from the pulse profile. The final amplifier is a single pass Nd:YAG rod, designed to work in saturation with 100mJ input. See Figure 4.1 for a diagram of the full system. All amplifiers are flash-lamp pumped and cooled on the same water loop. A schematic of the cooling loop is shown in Figure 4.2

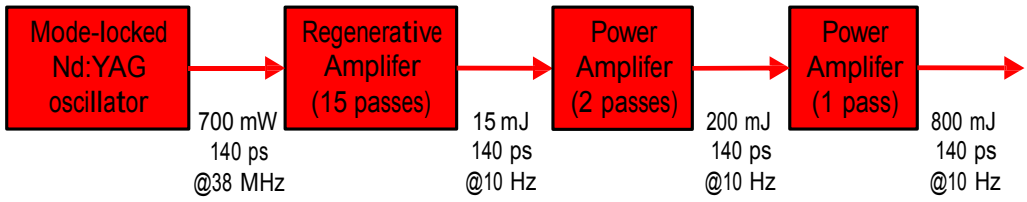

Figure 4.1 140 picosecond Nd:YAG system schematic layout

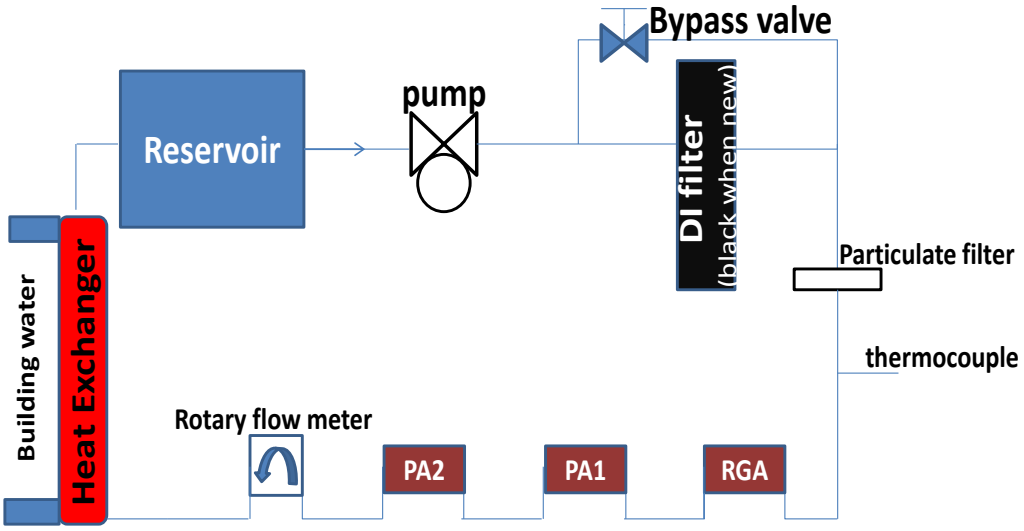

Figure 4.2 Nd:YAG cooling loop schematic

4.2 Titanium:Sapphire laser

Also used for many of these experiments is a custom-built commercial Ti:Sapphire (Coherent) laser capable of up to 800mJ output at a 10 Hz repetition rate in 36 fs pulses. A Coherent Micra Kerr-lens modelocked oscillator outputs <20 fs pulses at approximately 76.3 MHz with more than 65 nm of spectral bandwidth centered around 800nm. The oscillator pulse is passed directly into a Coherent Legend system. The Legend includes a stretcher, which temporally chirps the oscillator pulses to ~300 ps prior to chirped pulse amplification [64], and a 1 kHz RGA, pumped by a frequency doubled Coherent Evolution-15 Nd:YLF laser. The RGA contains two Pockel cells to close and open the amplifier cavity. The 1 mJ, 1 kHz output of the RGA is passed through an external Pockel cell to reduce the repetition rate to 10 Hz. It is then fed into a four-pass amplifier, pumped by two frequency doubled Q-switched Nd:YAG lasers, and finally recompressed in vacuum. See Figure 4.3 for a schematic of the layout.

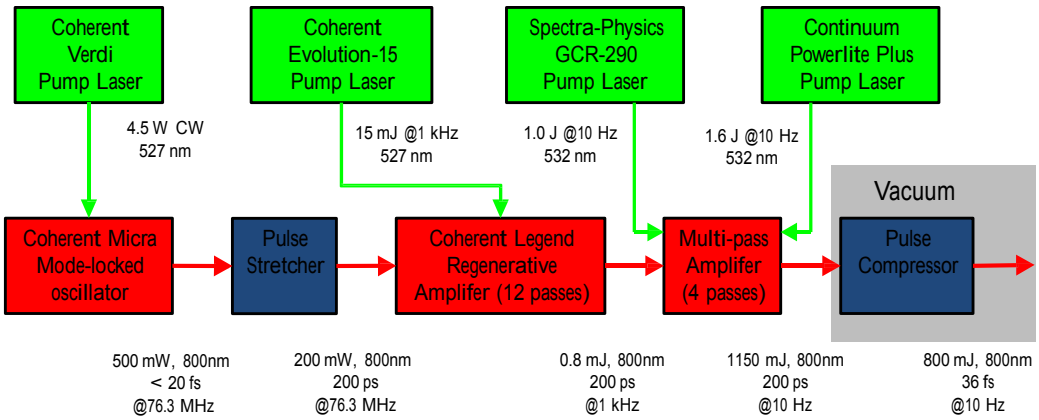

Figure 4.3 Ti:Sapphire system layout schematic

4.3 Synchronization

For these experiments, it is important to note that the Micra oscillator for the Ti:Sapphire system has an adjustable cavity length. Coarse control comes from the output coupling mirror, which is mounted on a translation stage with a motorized micrometer. Fine adjustment is done with a cavity mirror mounted on a piezo-electric transducer which is driven by a Coherent Synchrolock. The Synchrolock allows the phase and repetition rate of the Ti:Sapphire oscillator to be synchronized with an external clock, in this case the GE-100 Nd:YAG oscillator of the laser described above. The Synchrolock reference in accepts sine wave inputs with amplitude of 500mV±100mV. The delta function comb coming from the GE-100 photodiode is filtered using a low pass and high pass filter which are mini-circuits BLP-50 (part #10037, pass band DC-48 MHz) and BHP-25+ (part #15542, pass band 27.5-800 MHz) filters respectively. Oscilloscope traces of the photodiode output before and after filtering are shown in Figure 4.4.

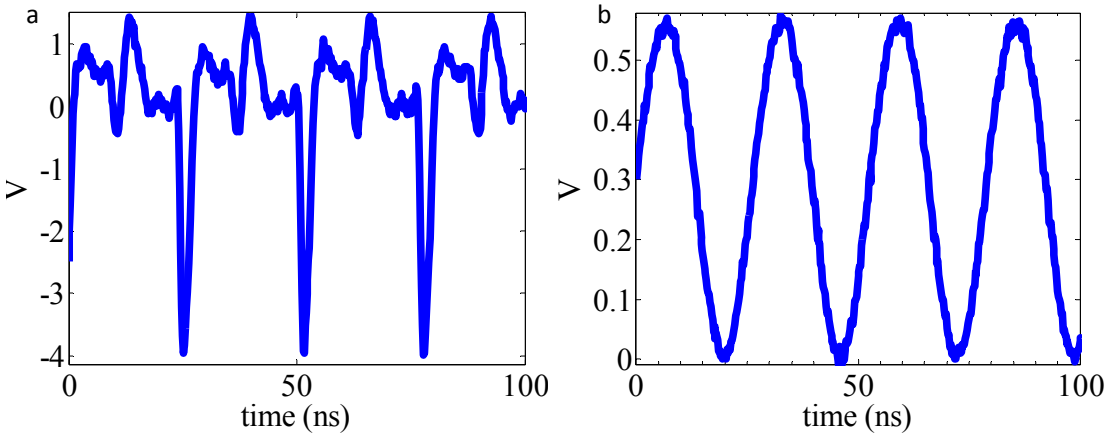

Figure 4.4 GE-100 Photodiode output
(a) Unfiltered photodiode output directly from GE-100
(b) Photo diode output after bandpass filter and amplification, for input into Synchrolock AP

The filtered photodiode signal passes through an analogue delay box, which allows the arrival time of the Ti:Sapphire and Nd:YAG optical pulses to be tuned to within one round trip of the Nd:YAG regenerative amplifier (23 ns). The analogue delay box attenuates the filtered photodiode signal strongly, so that there is not enough signal strength to serve as Synchrolock input. A signal amplifier with 20 dBm of amplification from 20-6000 MHz (mini circuits part #S F08601131) is therefore installed just before the Synchrolock. To reach 500mV of signal, 5dB and 4dB attenuators are placed after the amplifier (mini circuits model #HAT-5+ and #HAT-4 respectively).

The GE-100 photodiode signal is also fed directly to a Stanford 645 delay generator, which is capable of dividing the 38 MHz input clock into multiple lower frequency outputs. All system triggers are derived from this delay generator. Any devices which are sensitive to nanosecond scale delay must be synchronized with a specific oscillator pulse from either the Ti:Sapphire or Nd:YAG system. In practice, only the RGA Pockels cell timings are this sensitive and consequently the Pockels cell drivers require a trigger

enable signal at the system repetition rate and a trigger at the oscillator repetition rate. The next oscillator pulse after arrival of the trigger enable triggers the Pockels cell. After the two lasers pulses are arranged to within a round trip time of the 140 ps Nd:YAG RGA cavity, the Ti:Sapphire RGA Pockels cells are set to switch in the correct oscillator pulse to reduce the time delay to the Micra cavity round trip time (13 ns). Finally, the internal delay function of the Synchrolock is adjusted to synchronize the two lasers exactly. The two lasers can be synchronized to within 30 ps, with the timing jitter limited by the inherent jitter of the Stanford delay boxes. The Synchrolock itself is capable of < 250 fs jitter. The laser timing diagram is shown in Figure 4.5.

In an early configuration, the Stanford DG645 timing box was triggered by the Synchrolock output. This requires that both oscillators are running to operate either laser system, which produces unnecessary wear on the oscillators. Instead, the GE-100 photodiode was routed directly to the DG645 box making it possible to replace the GE-100 clock with an external crystal oscillator, so that either laser may be run independently. One downside of this configuration is that the 1 kHz trigger enable for the Ti:Sapphire RGA Pockels cells is now independent of the Synchrolock delay while the Pockels cell triggers themselves are not. The operator must be careful not to move the Synchrolock delay past the 1 kHz trigger enable, or the wrong oscillator pulse will be amplified and the timing between the two lasers will be incorrect by 13 ns (Figure 4.6). As a side note, changing cable lengths to the various delay generators will affect the system timing and should be avoided.

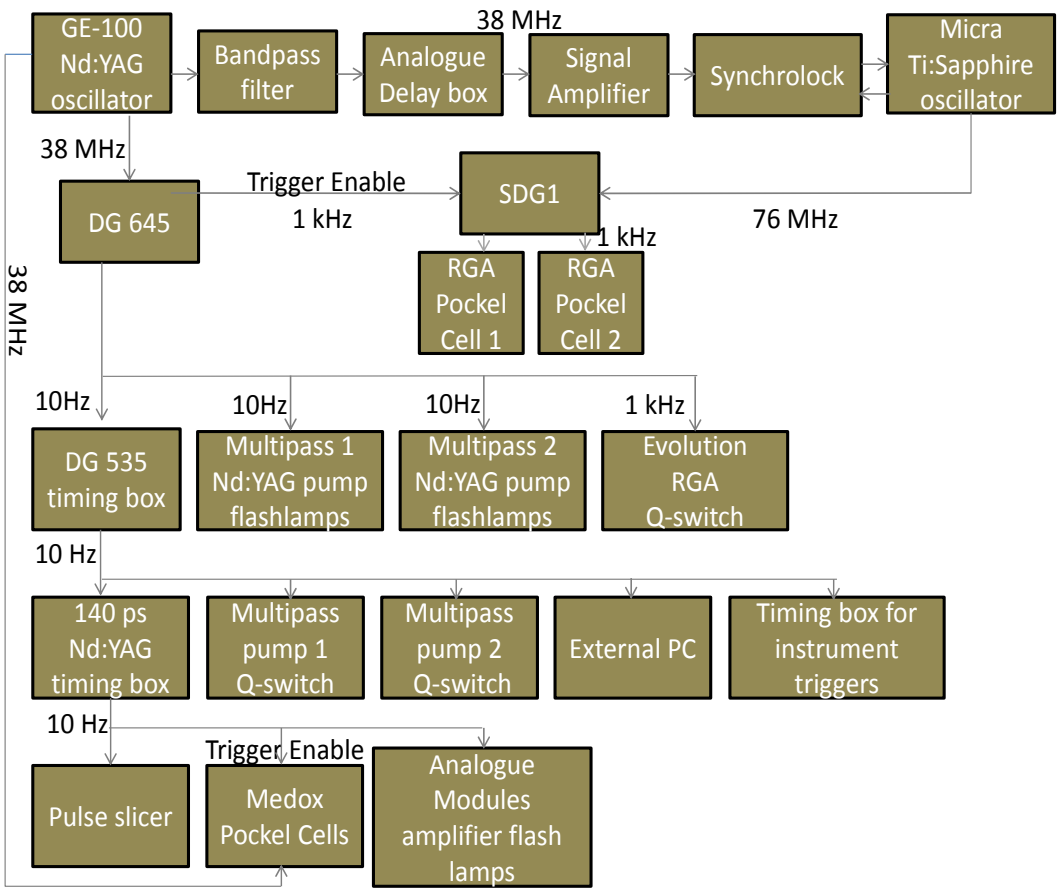

Figure 4.5 Laser system timing diagram.

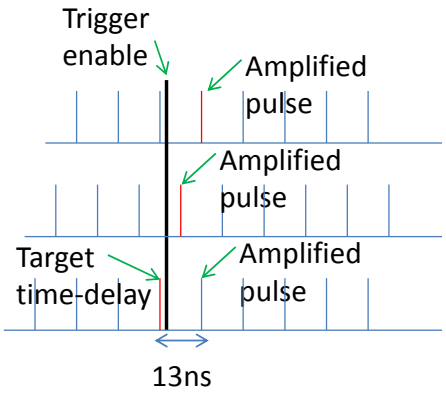

Figure 4.6 Trigger enable behavior of SDG timing box for Ti:Sapphire Pockel cell control.

Chapter 5 : Electron Density and Spectroscopy Measurements of Plasma Columns for Atmospheric Lasing

5.1 Motivation

Electric discharges in nitrogen gas have been used as a gain medium since the 1960s. Typically a high voltage electrical discharge pulse in nitrogen is used to produce a population inversion between the $C^3\Pi_u$ and $B^3\Pi_g$ vibrational states of N_2. Emission from this inversion (in the second positive system) produces UV light [65]. Early work found that a very intense, short duration pulse was generated a few nanoseconds into the high voltage discharge through heated electron collisional excitation of ground state nitrogen molecules [66]. Recently it was suggested two temporally delayed short-pulse lasers in an igniter-heater configuration should generate a population inversion in a similar manner [67], [68]. The scheme envisions an ultrashort pulse laser creating an initial electron density between roughly 10^{16} and 5×10^{16} cm^{-3}. The ultrashort pulse, typically 100fs FWHM or less, is followed a few hundred picoseconds later by a several hundred picosecond pulse which heats the preexisting electron population without further ionization to create the $C^3\Pi_u$ to $B^3\Pi_g$ inversion through collisional pumping by the transiently heated electrons. This would allow generation of ultraviolet wavelength lasers at a distance for remote sensing applications. Other groups have reported gain from the transition in question in high pressure gas mixes (1 atm N_2, 5 atm Ar) pumped by a single mid-IR filament [69] and indirect measurements of gain from a single filament in air [70]. To date, the plasma conditions which produce amplified spontaneous emission in laser induced nitrogen lasers have been poorly diagnosed. This chapter reports spectral and electron density measurements for various plasma conditions favorable to amplified spontaneous emission between the $C^3\Pi_u$ and $B^3\Pi_g$ states of N_2, generated by an igniter-

heater short pulse laser system. The igniter laser is a Ti:Sapphire system with 40 fs pulse duration and 10 Hz repetition rate. Up to 100 mJ are available for this experiment, which bypasses the vacuum system used when the laser is operated at its peak energy of 800 mJ. The heater laser is a Nd:YAG system with up to 600 mJ of energy in 140 ps pulses, also operating at 10 Hz. The two systems are synchronized to one another. See laser chapter for details.

5.2 Experimental Set up

Data from the experiment is generated in two configurations. In the first, a 40fs Ti:Sapphire laser pulse (the igniter) is focused through an axicon to generate an initial electron population. A high energy 140ps Nd:YAG pulse (the heater) is then focused through the same axicon after an adjustable time delay to heat the electrons and collisionally excite the $C^3\Pi_u$ state of molecular nitrogen. The axicon has a 1/8" hole drilled through the center, through which the Nd:YAG laser is used at low energy to probe the Ti:Sa generated plasma and obtain initial density measurements of the plasma column via interferometry. The center of the long plasma column is imaged to a folded wavefront interferometer which allows extraction of the integrated phase shift imparted to the probe over the full length of the plasma. Spectral emission of the plasma column is observed in two directions: parallel to the laser propagation direction and approximately 40 degrees from the propagation direction. The plasma column is imaged to an Ocean Optics HR+ 2000 spectrometer to maximize signal. The experimental set-up for configuration one is shown in Figure 5.1.

The two laser pulses are aligned spatially and temporally by optimizing igniter-heater driven gas breakdown for low energy heater pulses insufficient to produce breakdown on

their own. Temporal optimization is further refined using a fast photodiode, which allows us to place the peaks of the laser pulses within 200ps of each other. Time delay zero is then defined as the point with greatest electron density. The Ti:Sapphire and Nd:YAG laser mode-locked oscillators are synchronized with a phase-locked loop as described above, and the delay between the igniter and heater pulses is generated electronically.

Axicons with base angles of 30, 15 and 10 degrees have been used, which generate visible plasma columns 1, 3 and 5cm long respectively. The probe tends to refract somewhat for the longer columns, even though the electron density in the $\sim 10^{16}$ -10^{17} cm^{-3} range is relatively low. Simulations are used to estimate the amount of refraction and remove its contribution from the measured phase shift. Density may then be measured reliably as a function of time delay between igniter and heater pulses, axicon base angle, and igniter pulse energy.

In the second configuration, a 100fs Ti:Sapphire laser pulse is focused by a spherical lens system through the center hole in an axicon with an f# of 200. The pulse filaments in a well-understood dynamic process [71] to create a long plasma column. Filament densities have been measured to be between 1×10^{16} cm^{-3} and 5×10^{16} cm^{-3} depending on the focusing geometry and power [72]. The same heater pulse used in the first configuration is focused through an axicon with base angle 5 degrees to generate a 10cm long heated plasma column. The plasma emission is imaged to a spectrometer via the reflection off a Brewster window. Beam propagation simulations show that refraction becomes a significant issue for a 10cm long filament. Since in the case of a self-focused filament, the propagation dynamics and therefore the filament electron density profile

changes as a function of pressure, the linear extrapolation method used for the first configuration is no longer applicable and no density measurements were made.

Absolute counts viewed by the spectrometers for both experimental set-ups are very small. The spectra are integrated over several hundred shots to increase signal. For the same integration time and plasma conditions spectra are highly repeatable, justifying long time-scale integration. However, no time resolution of spectral data is available. Both experimental setups are located inside a vacuum vessel which allows different gas mixes and pressures to be studied.

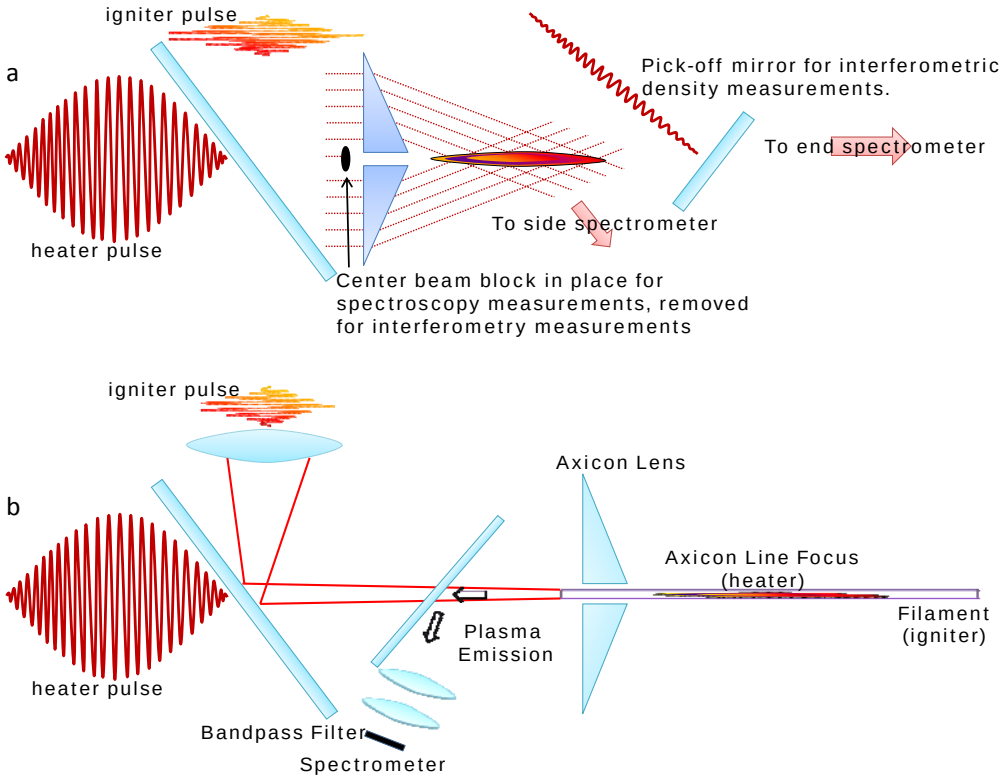

Figure 5.1 Experimental Setup.
(a) Configuration 1 igniter and heater focused through axicon lens and
(b) Configuration 2 with igniter filamenting through hole in center of axicon and heater focused through axicon lens

5.3 Results

The treatment of Penano et al [68] does not consider bulk plasma motion or avalanche ionization due to the heater pulse, and it assumes that the electrons obey a Maxwellian distribution. Avalanche ionization in air causes dissociation of the molecular nitrogen necessary for the population inversion of interest. Looking at spectral emission as a function of heater energy, the transition between avalanche ionization and pure heating in molecular nitrogen can be observed at atmospheric pressures (Figure 5.2) [73], [74]. The dominant plasma species are either N_2 or N^+ depending on the heater intensity. At lower pressures, the molecular emission is present even for very high heater energy, although there is still a notable transition between ion-dominated emission and molecular-dominated emission. Visually, it is possible to see when avalanche ionization begins to dominate in the plasma column by the presence of bright local breakdowns. Pre-ionization by the femtosecond ionizing pulse lowers the energy threshold for avalanche ionization by the heater pulse as well as doubling the fluorescent emission intensity of the plasma and lengthening the plasma column (Figure 5.3). The spatial smoothing of a gas breakdown has been observed by other groups in air constituent gases and the noble gases [75].

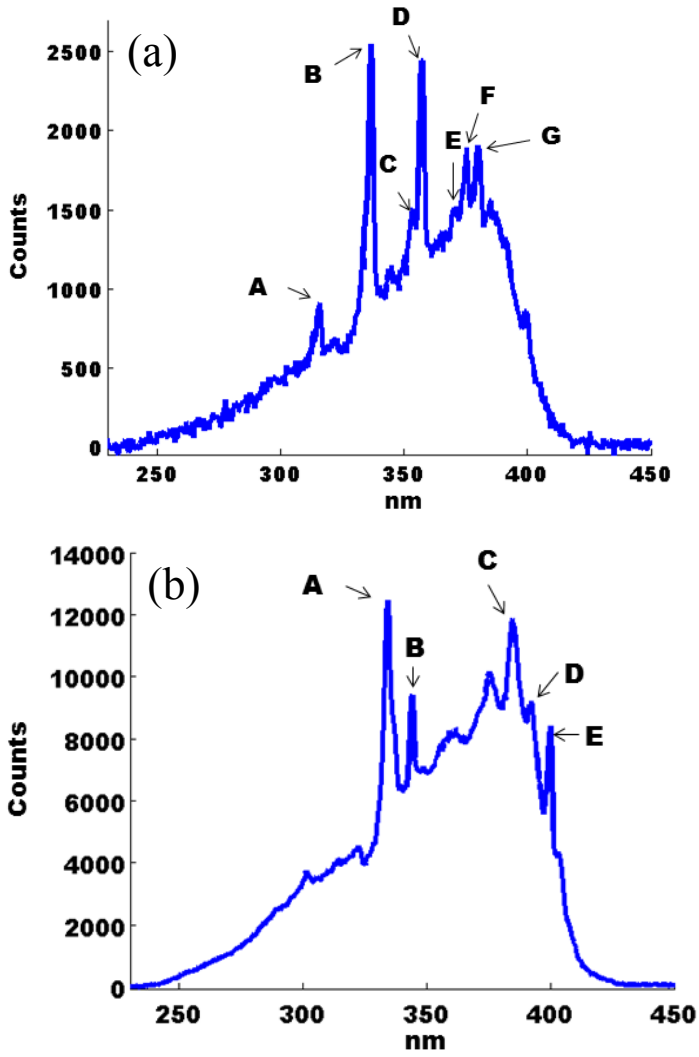

Figure 5.2 Plasma Emission
(a) Emission lines of the second positive band of nitrogen for 20mJ of igniter energy and 95 mJ of heater energy focused through a 30˚ base angle axicon creating a 1 cm plasma column. This spectrum is a sum over 100 laser pulses.
A 315.9nm, $C^3\Pi_u$ v'=1 to $B^3\Pi_g$ v''=0 **E** 371.0nm, $C^3\Pi_u$ v'=2 to $B^3\Pi_g$ v''=4
B 337.1nm, $C^3\Pi_u$ v'=0 to $B^3\Pi_g$ v''=0 **F** 375.5nm, $C^3\Pi_u$ v'=1 to $B^3\Pi_g$ v''=3
C 353.6nm, $C^3\Pi_u$ v'=1 to $B^3\Pi_g$ v''=2 **G** 380.5nm, $C^3\Pi_u$ v'=0 to $B^3\Pi_g$ v''=2
D 357.8nm, $C^3\Pi_u$ v'=0 to $B^3\Pi_g$ v''=1
(b) Emission lines of singly ionized nitrogen for 20mJ of igniter energy and 530 mJ of heater energy focused through a 30˚ base angle axicon creating a 1 cm plasma column. This spectrum is a sum over 100 laser pulses.
A 333.1nm, $2s^22p3p$ 3D J=2 to $2s^22p4s$ 3P° J=1
B 343.7nm, $2s^22p3s$ 1P° J=1 to $2s^22p3p$ 1S J=0
C 383.8nm, $2s^22p3p$ 3P J=2 to $2s^22p4s$ 3P° J=2
D 391.8nm, $2s^22p3p$ 1P J=1 to $2s^22p3d$ 1P° J=1
E 399.5nm $2s^22p3s$ 1P° J=1 to $2s^22p3p$ 1D J=2

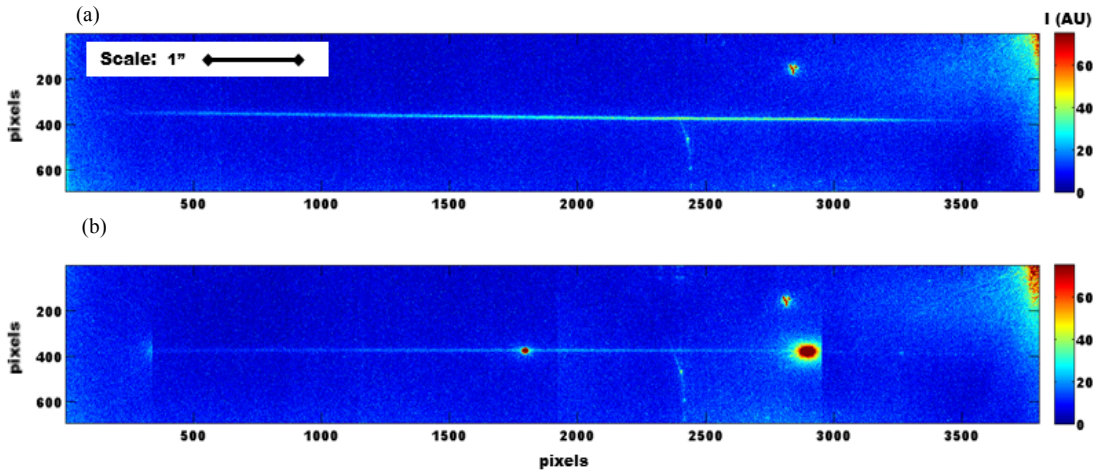

Figure 5.3 Pictures of plasma column
(a) Heated filament.
(b) Composite image consisting of an image of the igniter filament superimposed on an image of localized avalanche ionization due to heater pulse.

In addition to spectroscopic observations, electron density measurements were carried out. Due to the low electron densities involved, a probe passed transversely across the plasma does not pick up enough phase shift to accurately extract electron density. Instead, the probe for this experiment was co-propagated with the pump beam longitudinally down the plasma axis (Figure 5.4).

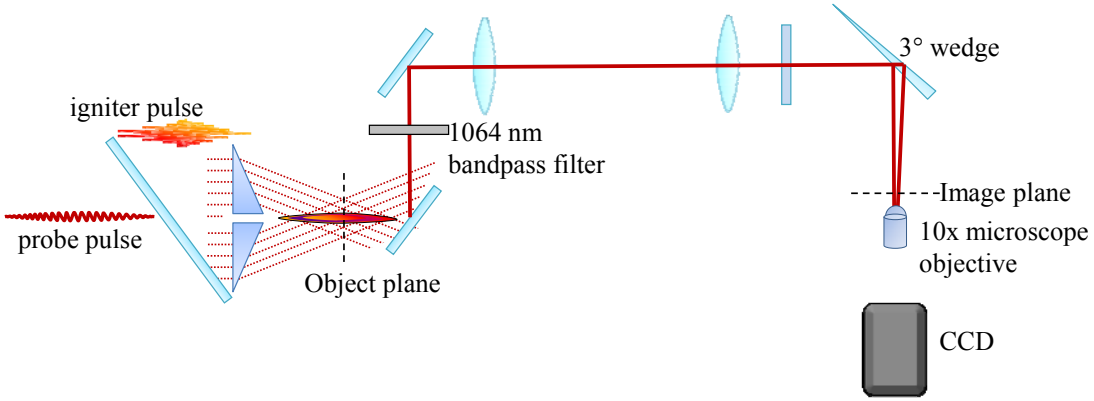

Figure 5.4 Interferometer layout

The phase shift is therefore integrated over the plasma column length and becomes significant. However, as described in chapter 2, probe refraction in plasma has a strong

effect on interferometric density measurements. Therefore, a simple beam propagation code is used to test the effect of refraction. The code takes as input an initial probe electric field and two-dimensional index of refraction profile. The field is transformed to the spectral domain and a Fraunhofer integral used to calculate diffraction. After transformation back to the spatial domain refraction is calculated using the input refractive index. The program then steps forward some axial increment Δz and repeats the process. See chapter 2 and reference [61] for details. For these simulations the plasma refractive index was assumed to have a Gaussian transverse profile with a full width half max of 80μm (corresponding to the experimental axicon focal spot). Axially, the index of refraction was assumed to have a step function profile, with the index of vacuum before and after the axicon line focus and $n \approx 1 - \frac{N_e}{2N_{cr}}$ as the standard plasma index of refraction determined by the electron density in the line focus where, in cgs units, the critical density is $N_{cr} = \frac{m_e \omega^2}{4\pi e^2}$, where m_e is the electron mass, e is the electron charge, and ω is the probe laser frequency. The simulation results are shown in Figure 5.5 (a) along with two experimental points for validation. According to the simulation, refraction should change the measured probe phase shift for a 3 or 5 cm plasma by at most a factor of four. However, the impact of a 10cm plasma column may be as large 20 times different from the result without refraction.

Having established that for the short plasma columns our density measurements are reasonably accurate, density measurements were made as a function of time delay between the probe and igniter pulses. The results were corrected according to the beam propagation simulations, but should be within an order of magnitude of the actual value

even with no correction. The results are shown in Figure 5.5(b) and agree with previous filamentation results [72].

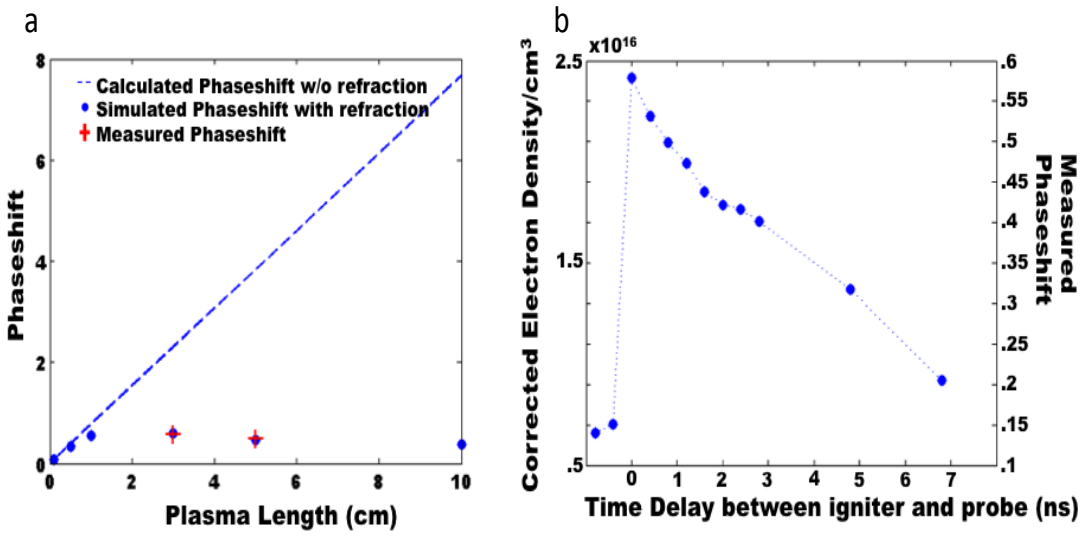

Figure 5.5 Density Measurements
(a) Beam propagation simulation compared to experimental results. Measured phaseshifts shown are peak values for the 15 degree (3cm plasma) and 10 degree (5cm plasma) axicons
(b) Electron densities for igniter energy 35mJ along a 3 cm plasma column in air as a function of time delay between pump and probe pulses.

Spectra were recorded for the ten and fifteen degree base angle axicons producing plasma columns 5 and 10 cm long respectively with the experimental chamber filled with nitrogen gas. The peak electron density in nitrogen is approximately 10% less than that of air due to the absence of oxygen, which has a lower ionization potential than nitrogen, but the spectra are simpler. Our side and end spectrometers are not calibrated relative to one another. Therefore to demonstrate amplified emission the possibly amplified spectral line is compared to a nearby line on each spectrometer. Then the relative signal observed along the plasma column is compared to the relative signal observed at 40 degrees to the axial direction (Figure 5.6). If amplified spontaneous emission is present the ratio between the amplified line and the nearby line should be much larger on the end

spectrometer than the side spectrometer, which should observe only spontaneous emission. Comparison of the amplitude of the spectral line located at 334.1nm due to the second state of ionic nitrogen with the amplitude of the spectral line located at 337.1nm due to the $C^3\Pi_u$ v=0 to $B^3\Pi_g$ v'=0 transition of molecular nitrogen, for which lasing has been observed in nitrogen discharge lasers, is shown below. The transition at 357.8nm, $C^3\Pi_u$ v'=0 to $B^3\Pi_g$ v''=1, which has also been observed to lase is unfortunately not accessible to our spectrometer due to a stop band from 345-400nm caused by a zero degree YAG dielectric mirror used to block laser light from the spectrometer. There is some evidence of higher emission in the molecular line which should lase as the plasma column length increases, but no evidence of the exponential gain expected for saturated stimulated emission. This may be because the plasma column is still too short to saturate the gain at these densities. It is also possible the computational results predicting lasing are overly optimistic.

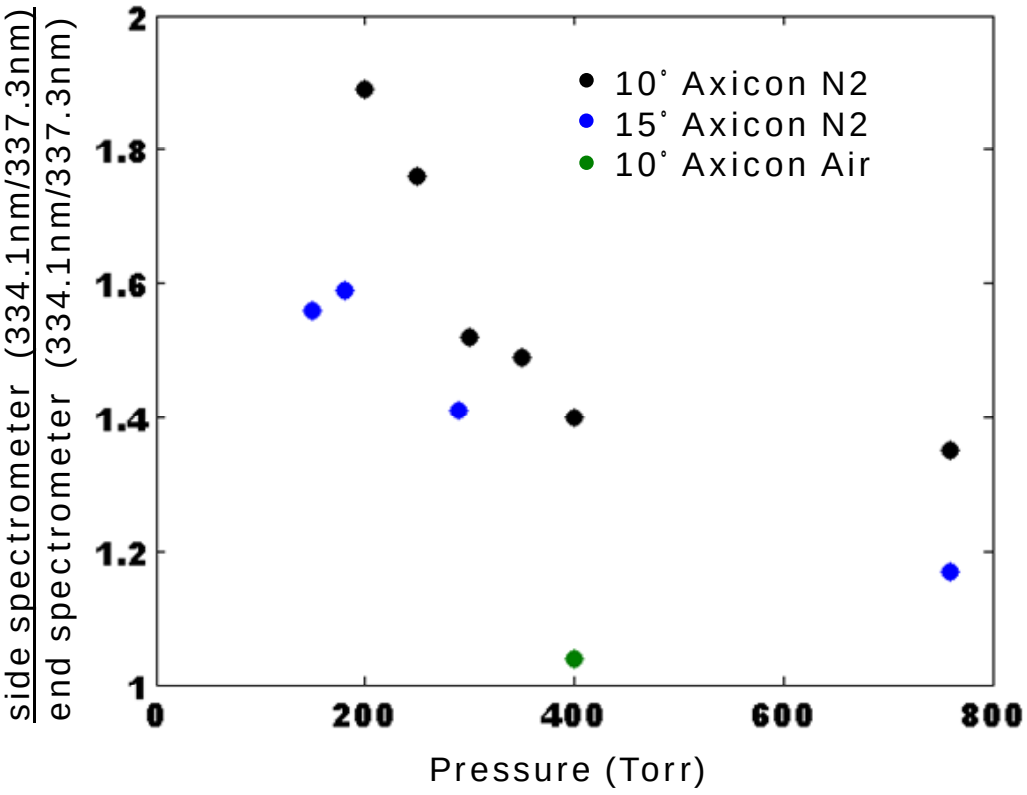

Figure 5.6 Strength of emission from $C^3\prod_u$ v'=0 to $B^3\prod_g$ v''=0 transition at 337.1nm from spectrometer collinear with plasma column compared to spontaneous emission viewed at 40˚ to axis of plasma column.

The axicon lens focusing the Ti:Sapphire igniter spreads the available laser energy along the length of the plasma column. For the above experimental set-up it is not possible to achieve a longer axicon-created plasma column with the necessary electron densities. Therefore the experimental layout is changed to configuration 2 described above. In this set-up, the Ti:Sapphire pulse is focused through a spherical lens and all available power contributes to field ionization at any given axial location. From previous studies, filaments are known to be density clamped with densities between ~$1x10^{16}$ and ~$5x10^{16}cm^{-3}$ depending on the focusing parameters and pulse duration [72]. The plasma length in this configuration is limited by the available heater power, which is sufficient to break down a 30cm length of gas. An axicon with base angle 5 degrees and 10 cm

visible breakdown length due to the heater pulse alone was on hand and used in the experiment. Because of the filamentation process, the spectrum in the forward direction is contaminated by a supercontinuum tail extending to UV wavelengths. Consequently, all spectra were observed from emission counter propagating with respect to the igniter and heater pulses. Bandpass filters were used to remove laser reflections which might damage the spectrometer. The two primary filters are 340+-5nm FWHM and 360+-5nm FWHM to allow observation of the 337.1nm ($C^3\Pi_u$ v'=0 to $B^3\Pi_g$ v''=0) and 357.8nm ($C^3\Pi_u$ v'=0 to $B^3\Pi_g$ v''=1) lines which have been observed to lase.

Emission through the 360nm bandpass filter is shown in Figure.5.7 (b). Clear differences are seen in the spectra of the igniter only, heater only, and combined pulses. The heater emission follows the transmission curve of the bandpass filter and is due to a broadband emission from local avalanche ionization. The 357.8 nm line is visible above the spectrometer noise floor in both the igniter only and igniter-heater spectra. The amplitude of this line in the igniter-heater plasma is larger than the simple sum of the heater and igniter plasmas, however the amplitude difference is not large enough to be explicit evidence of stimulated rather than spontaneous emission. Since oxygen attachment is expected to be detrimental to the excitation of a population inversion, this measurement was repeated in a mixture of krypton and nitrogen which has a similar ionization potential to air. The results are shown in Figure.5.7 (c). The increased signal compared to air is attributable to an increased background due to avalanche ionization rather than a relative increase of the 357.8nm line compared to background. The spectrum observed through the 340nm bandpass filter is not clearly distinguishable from noise.

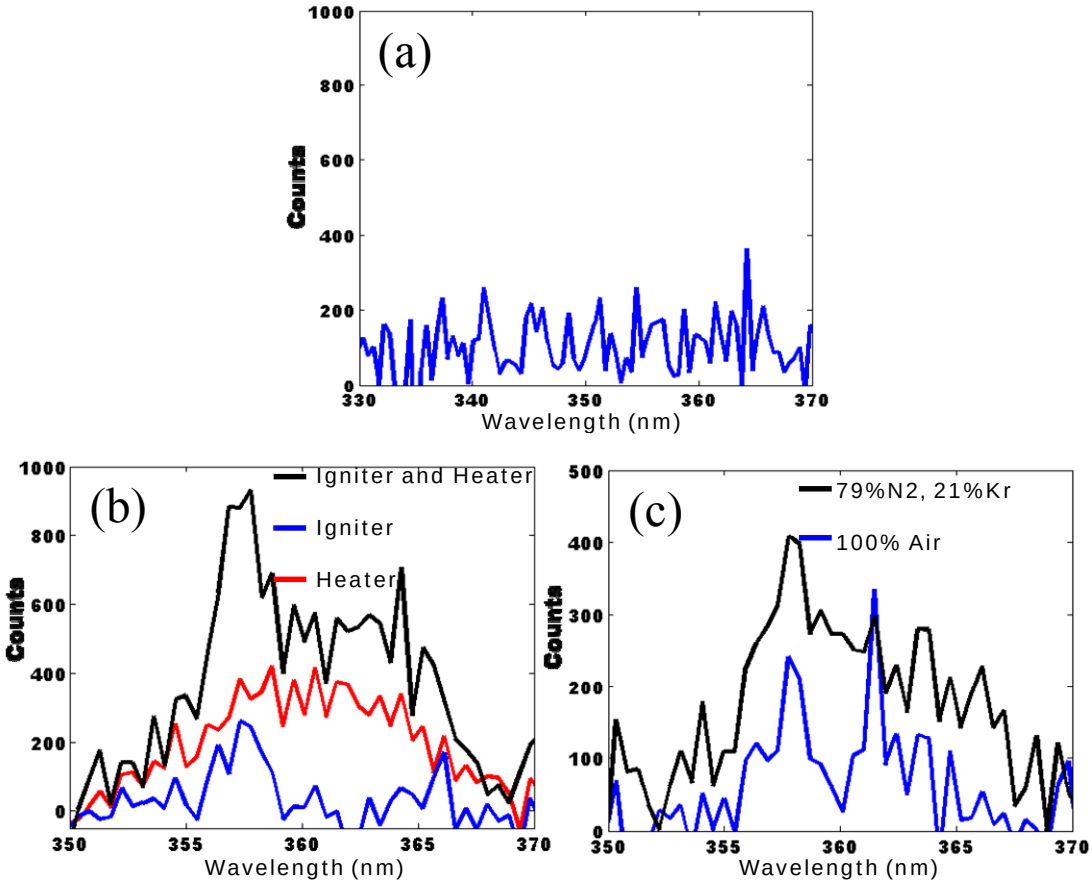

Figure.5.7 Spectroscopic Measurement
(a) spectrometer noise floor.
(b) Emission due to 10mJ igniter energy, 575mJ heater energy in air.
(c) Emission due to 5mJ igniter energy and 575mJ heater energy in air and in krypton, nitrogen gas mix.

5.4 Conclusions

For both experimental configurations the igniter-heater arrangement makes the ionization breakdown more uniform, reducing the occurrence of strongly localized avalanche ionization which is the typical break down mode of a focused 140ps Nd:YAG laser. The femtosecond filament emission is primarily molecular, in contrast to the strong ionic emission seen due to the heater laser alone. The heated filament also exhibits stronger emission than an unheated filament for the same igniter laser parameters. Slightly higher emission is seen in the forward direction than in the

transverse direction for short plasma columns, but if this is stimulated emission the gain length is much longer than the length of the plasma columns investigated. For long plasma columns, emission in the backward direction is observed but no evidence of strong amplification of the $C^3\prod_u$ v'=0 to $B^3\prod_g$ v''=0 transition is seen. The effect of refraction on interferometry density measurements can be compensated by numerical simulations provided the length and transverse extent of the plasma column is well known.

Chapter 6 : Resonant multiphoton ionization of Xe^+

6.1 Introduction

There have been a number of recent studies of plasma dynamics following ionization by an ultrashort optical pulse, using transient diffraction and examination of fluorescence spectra [76–78]. In this chapter, supercontinuum spectral interferometry in a thin gas target is applied to time-resolve the ionization from a relatively weak pulse in a pre-formed xenon plasma. The initial purpose of the experiment was to measure the nonlinear index of refraction of singly ionized xenon (Xe^+), analogous to the measurement in neutral atoms [18,19]. In practice, the positive phase shift imposed by the Kerr effect on a probe pulse in ionic Xe is not detectible, due to unanticipated further ionization of the Xe^+ medium. Even for a pulse with an intensity below the ionization threshold of neutral Xe (ionization potential 12 eV) there is significant ionization in the Xe^+ plasma (ionization potential 21 eV). The ionization yield is found to increase with the time delay between the plasma formation and the weak pulse, saturating at a few picoseconds of time delay. The most likely explanation is impact excitation of Xe ions followed by ionization of the excited Xe^+ states, which is roughly consistent with the expected impact excitation cross section and corroborated by the observation of absorption lines corresponding to excited states of Xe^+. Our data shows that the unanticipated ionization is due to resonant multiphoton ionization of the collisionally excited Xe^+ states and that this process is not unique to xenon. The picosecond timescale plasma dynamics discussed in this chapter are important in ultrafast laser-plasma interaction experiments which extend beyond the few hundred femtosecond regime.

6.2 Experimental Set-up

The experimental setup is shown in Figure.6.1. The xenon plasma is created inside a thin gas target consisting of a pinched copper tube with laser-drilled holes ~150 μm in diameter. Xenon is flowed into the tube at pressures of up to 100 Torr, and the vacuum chamber pressure outside the tube is several hundred mTorr. The linear phase shift imposed on a CW laser probe through the target is measured using an auxiliary beam line and a spatial interferometer [18]. The phase shift is consistent with a region of gas at the input pressure with an axial extent of 450 μm, which matches the distance between the outer walls of the flow tube. A Ti:Sapphire amplifier producing 40 fs, 3.5 mJ pulses centered at 800 nm is used to generate the four laser pulses used in the experiment. An initial plasma preparation pulse with intensity up to $3x10^{14}$ W/cm^2 is focused through vacuum into the gas flow tube (Figure.6.1). The spot size is ~40 μm, corresponding to an 8 mm confocal parameter. The short interaction range imposed by the gas tube ensures that the plasma is uniform along the laser propagation direction.

A weak pump pulse passes through the pre-formed plasma generated by the preparation pulse, and is used to study the ionization of Xe^+. The pump pulse is an order of magnitude less intense than the preparation pulse, and has the same focal spot characteristics.

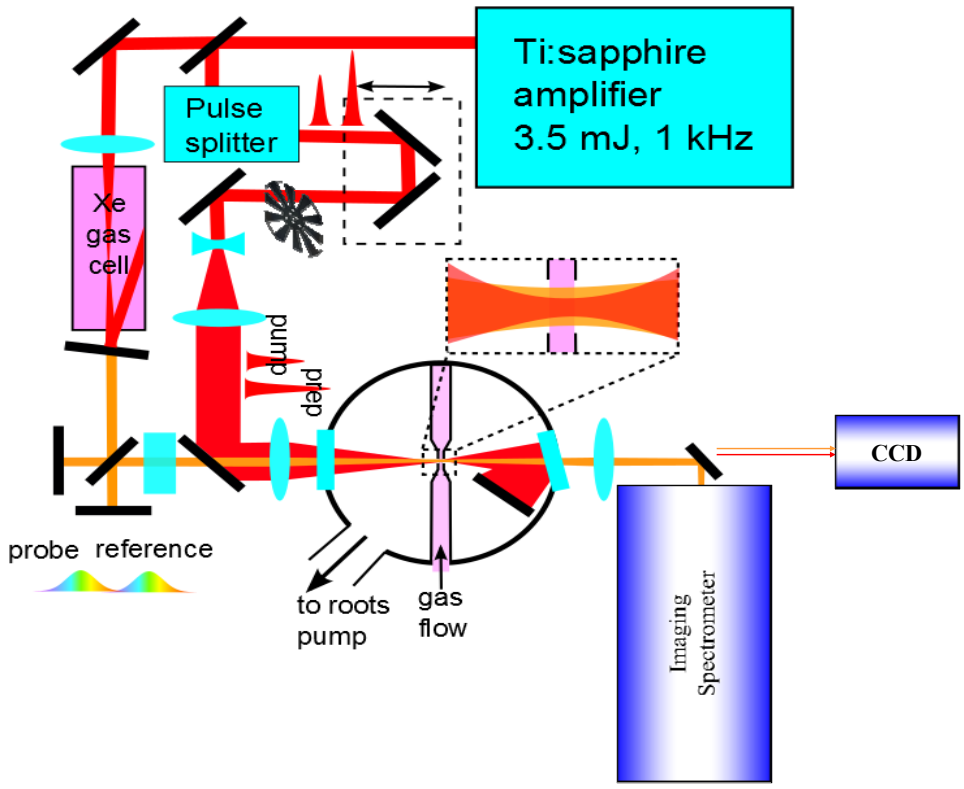

Figure.6.1 Diagram of experimental setup, including single-shot supercontinuum spectral interferometry for measurement of laser-produced plasmas.

The time-dependent electron density profile is found using single-shot supercontinuum interferometry (SSSI) [56], which measures the 1D spatial- and time-dependent phase shift imposed on a chirped probe due to laser-induced plasma. The SSSI technique has been described in detail elsewhere [21,54]. See also chapter 2.

Figure 6.2 (c) is a typical density map $N_e(x,t)$ with the SSSI probe temporally overlapping the preparation pulse, as shown in Figure 6.2 (a). The negative phase shift after t=0 is due to ionization by the preparation pulse [19,21]. The electron density due to ionization is $N_e(x,t) \approx -2N_{cr}\Delta n(x,t)$ where $N_{cr} = \frac{m_e\omega^2}{4\pi e^2}$ is the critical density and Δn is the change in index of refraction. At a maximum intensity of $3\cdot10^{14}$ W/cm^2, N_e = $3\cdot10^{18}$ cm^{-3}, consistent with more than 100% single ionization of 100 Torr Xe. The

depletion of the plasma preparation pulse energy during ionization is negligible. Assuming single ionization with the electron entering the continuum with zero velocity, the ~500 μJ preparation pulse is depleted by less than 1% using 12 eV for the Xe ionization potential [74].

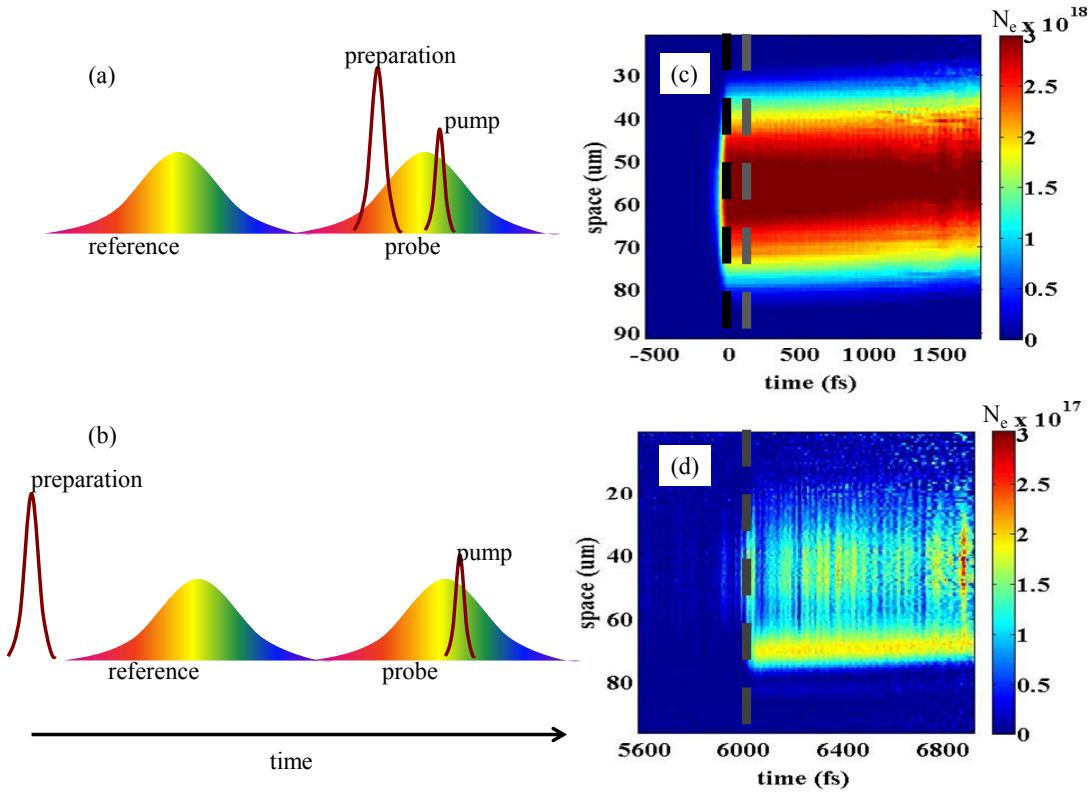

Figure 6.2 Two possible laser pulse timings. (a) Probing short delay times after plasma generation and (c) resulting extracted electron density includes absolute change in density due to plasma formation. The preparation (pump) arrival times is shown as a black (grey) vertical dashed line. (b) Probing long time delays after plasma generation. (d) The late time electron density map shows change in electron density due to pump pulse but contains no information about the absolute electron density. The striations visible in the electron density map (d) are Xe^+ absorption lines in the probe spectrum.

6.3 Below-Threshold Ionization

The primary result of this chapter concerns additional ionization by a weak second pulse, hereafter called the "pump" pulse, that arrives at a controllable time *t* following the strongly ionizing preparation pulse, as depicted in Figure 6.3(a). Enhancement of the

ionization yield is observed using two pulses, compared to the total ionization with each pulse alone (Figure 6.3). The pump induced phase shift in neutral xenon gas is one fifth that produced by the same pump pulse in a Xe^+ plasma, which has a much higher ionization potential of ~20 eV [74]. In fact, ionization is observed in Xe^+ for intensities an order of magnitude below the predicted threshold of $5 \cdot 10^{14}$ W/cm^2 calculated from multiphoton ionization theory [37]. Plasma dynamics and resonant processes must be taken into account to explain the ionization in the prepared plasma, which is responsible for approximately 5% of the total electron density. The time-dependent phase shift measured due to both preparation and pump pulses is shown in Figure 6.3(b), with a zoomed in vertical scale in Figure 6.3(c) showing the pump pulse-induced phase shift. The phase shift measured using SSSI is the difference between the phase imposed on the reference and probe pulses. The temporal spacing between the reference and probe pulses is fixed, so that measurements must be made in two different experimental configurations: with the preparation pulse either overlapped with the probe pulse (configuration in Figure 6.2(b)) or before the reference pulse (configuration in Figure 6.2(a)). In configuration 5.2(a), the measured phase shift can be converted to absolute electron density due to preparation pulse ionization. In configuration 5.2(b), the preparation pulse arrives well before the reference pulse, and the reference phase is shifted due to the plasma background. In this case, the difference in electron density between reference and probe arrival time is measured. The total time window in which the change in electron density can be measured in a single shot is 4 ps, the pulse duration of the probe pulse. This time window can be moved over multiple shots to view a larger temporal area. The preparation and probe laser intensities are carefully measured using

focal spot profiles and pulse energies recorded for every shot and pulse temporal durations recorded at the beginning of a data set.

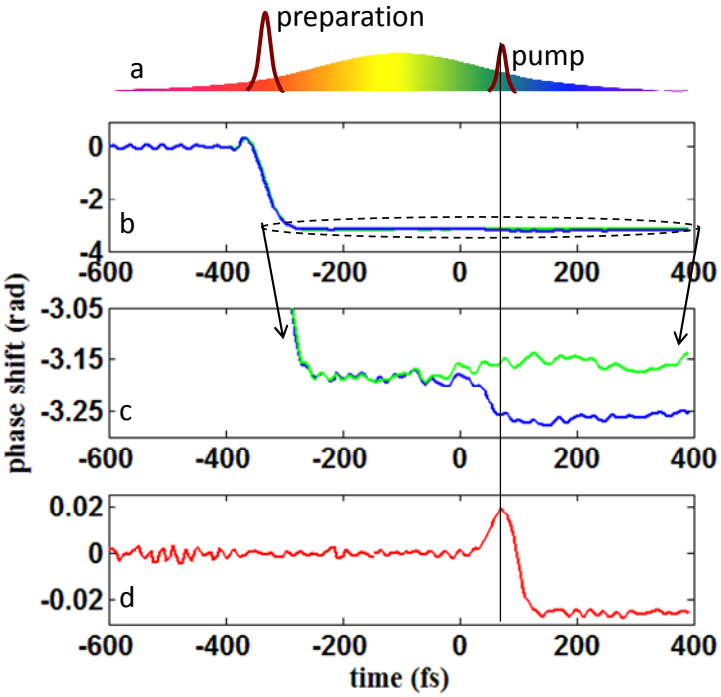

Figure 6.3 (a) Schematic of the pulse sequence. (b) Initial ionization by preparation pulse alone (green) and by the preparation and pump pulses together (blue) The two signals are identical until arrival of the pump pulse, indicated by the solid black vertical line. (c) Magnified view of region near t = 0, the arrival time of the pump pulse, showing the additional 100 mrad phase shift due to the pump pulse. (d) Phase shift due to Kerr response in neutral Xe followed by ionization due to the pump pulse [19]. The phase shift is approximately 20 mrad, 5 times smaller than observed in the mostly Xe^+ plasma present in part (c).

A possible explanation for the ionization of Xe^+ observed is the presence of excited states, which may be studied by transient absorption spectroscopy using the probe supercontinuum. The IR pump pulse and broadband reference pulse are blocked and the probe spectrum transmitted through the plasma is measured as a function of the time delay between the preparation pulse and the probe pulse. In the co-propagating geometry, absorption data is limited to 480-700 nm due to the bandwidth of the probe at short wavelengths and pump pulse saturation of the spectrometer at long wavelengths.

Figure 6.4 shows a typical absorption spectrum, at 4 ps time delay between preparation and probe pulses, overlaid with Xe^+ emission lines from the NIST atomic spectra database. Every ionic xenon line of appreciable strength in this wavelength range is present, giving direct evidence of excited Xe^+ states with energies from 11.5 eV to 15.5 eV.

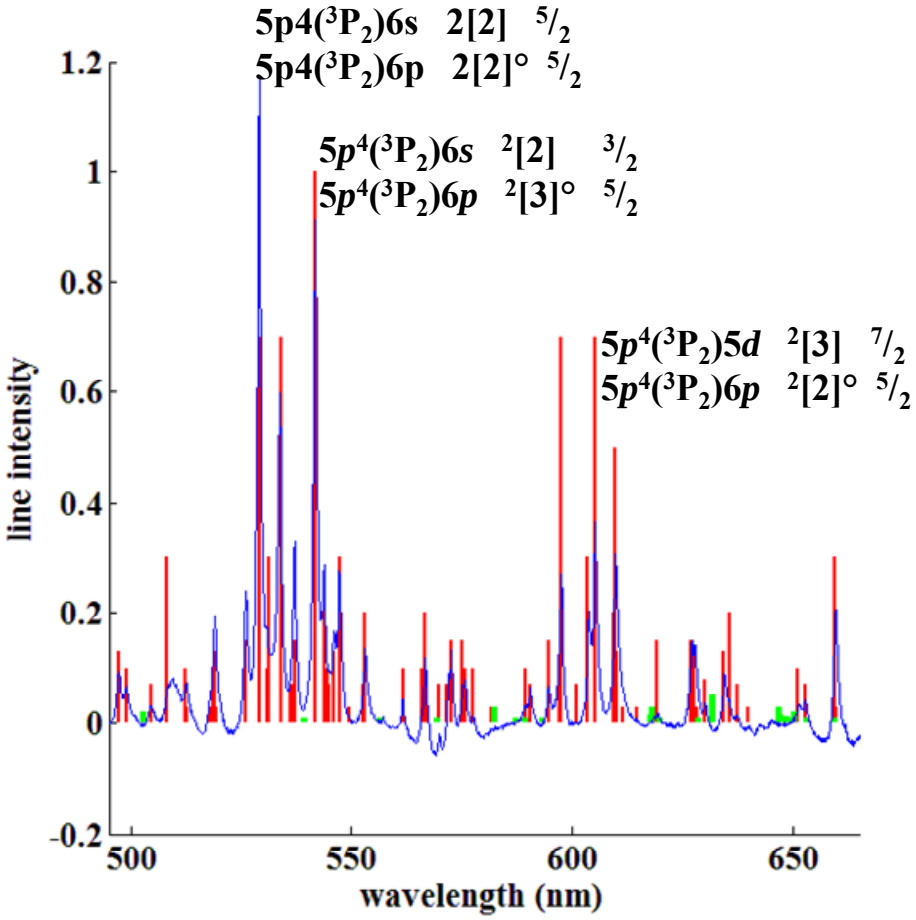

Figure 6.4 Absorption spectrum (blue) at 4 ps time delay between the preparation pulse and the probe pulse. The red lines are NIST tabulated values for Xe^+ [74], and the green lines are NIST values for neutral Xe. Observed absorption lines correspond to electronic states with energies between 11.5eV and 15.5 eV. The initial and final states for a few prominent transitions are labeled.

6.4 Collisional Excitation

To investigate the origin of the Xe^+ excited state population the change in the ionization rate and population as a function of time is studied. Time resolved electron

density measurements show the electron density increasing over several picoseconds after initial plasma formation before reaching a steady-state value. Examination of the temporal of population of excited Xe^+ states, as measured by time resolved absorption spectroscopy, reveals the same temporal shape and rate, with zero excited state population immediately after the plasma formation (Figure 6.5 (b)). Absorption data for a fixed laser intensity and variable electron density is fit to $1-\exp^{-x/\tau}$, where τ is the saturation time. The result of this fit for several different initial electron densities is shown in Figure 6.6. The saturation time has a quadratic dependence on the initial plasma density, as expected for collisional plasma processes when the electron and ion densities are equal. The same increase in excited state population as a function of time is observed in Kr^+ (Figure 6.7), with a slightly longer time constant.

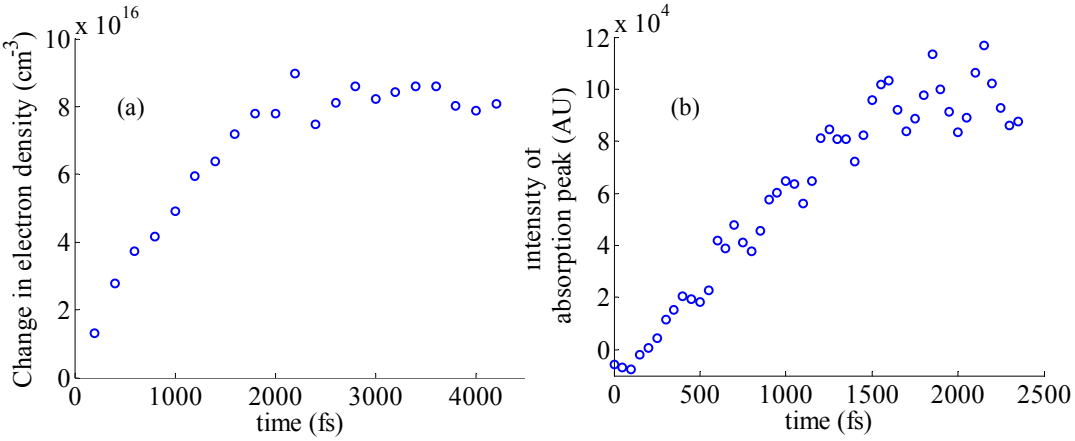

Figure 6.5 (a) Change in electron density due to ionization of Xe^+ from pump pulse as a function of delay after plasma formation. (b) Absorption as a function of time after plasma formation for 597.6nm line ($5p^4(^1D_2)6s\ ^2[D]$ J=3/2 to $5p^4(^1D_2)6p\ ^2[P]^\circ$ J=3/2 transition).

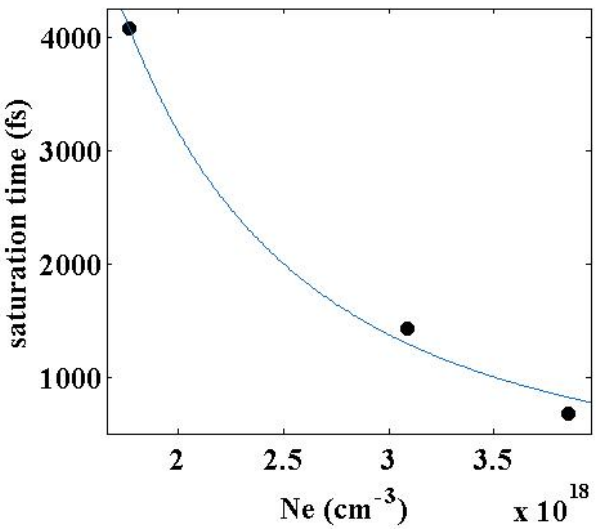

Figure 6.6 The saturation time of the 597.6nm Xe^+ absorption line as a function of initial plasma density, with a quadratic fit in blue.

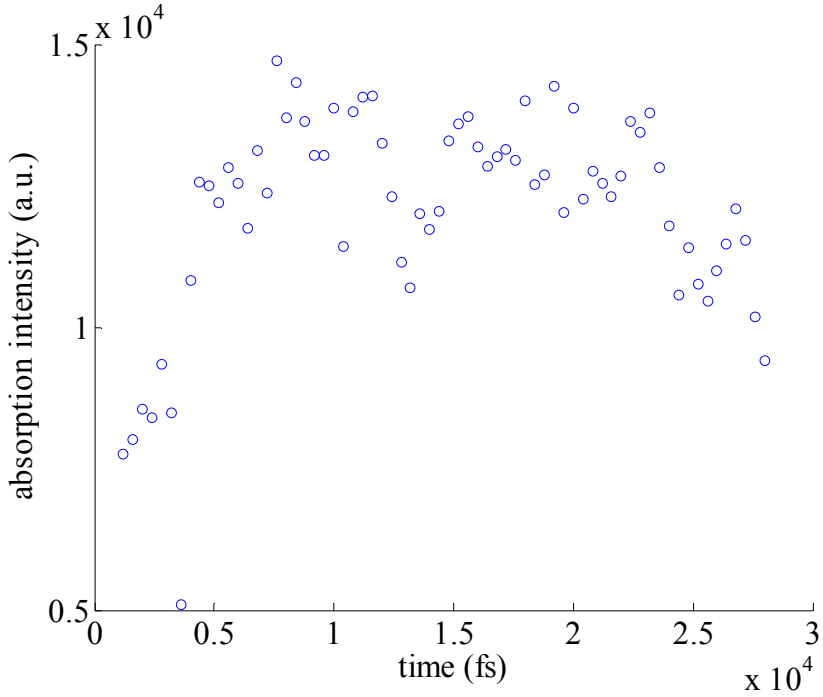

Figure 6.7 Absorption strength as a function of time for a representative Kr^+ spectral line.

An order of magnitude estimate for electron-Xe^+ excitation cross-sections can be made using measured cross-sections for Ar^+ for corresponding states. The Ar^+ maximum cross-section is $\sigma_{max}= 20\cdot10^{-17}$ cm^2 from the ground state to $3s^2 3p^6\ ^2S$ for 14eV incident

electrons [79]. In comparison, in Kr^+ $\sigma_{max}=10\cdot10^{-17}$ cm^2 from the ground state to $4s^24p^6$ ^2S for 22eV incident electrons [79]. Assuming a similar σ_{max} for electron-Xe^+ collisions, with the experimentally measured electron density, a collision frequency of $5.7\cdot10^{10}$ s^{-1} is obtained; leading to an estimate that 5% of xenon ions should be collisionally excited from the ground state to the low-lying excited states per picosecond. This is an overestimate, since it is highly improbable that the entire electron population will have the necessary energy to achieve a maximal excitation cross-section. However, it is of the correct order of magnitude to predict the few percent ionization of Xe^+ observed experimentally. A diagram of the electronic states of Xe^+ is shown in Figure 6.8 with the measured excitation cross-sections from Ar^+ imposed on the equivalent xenon states.

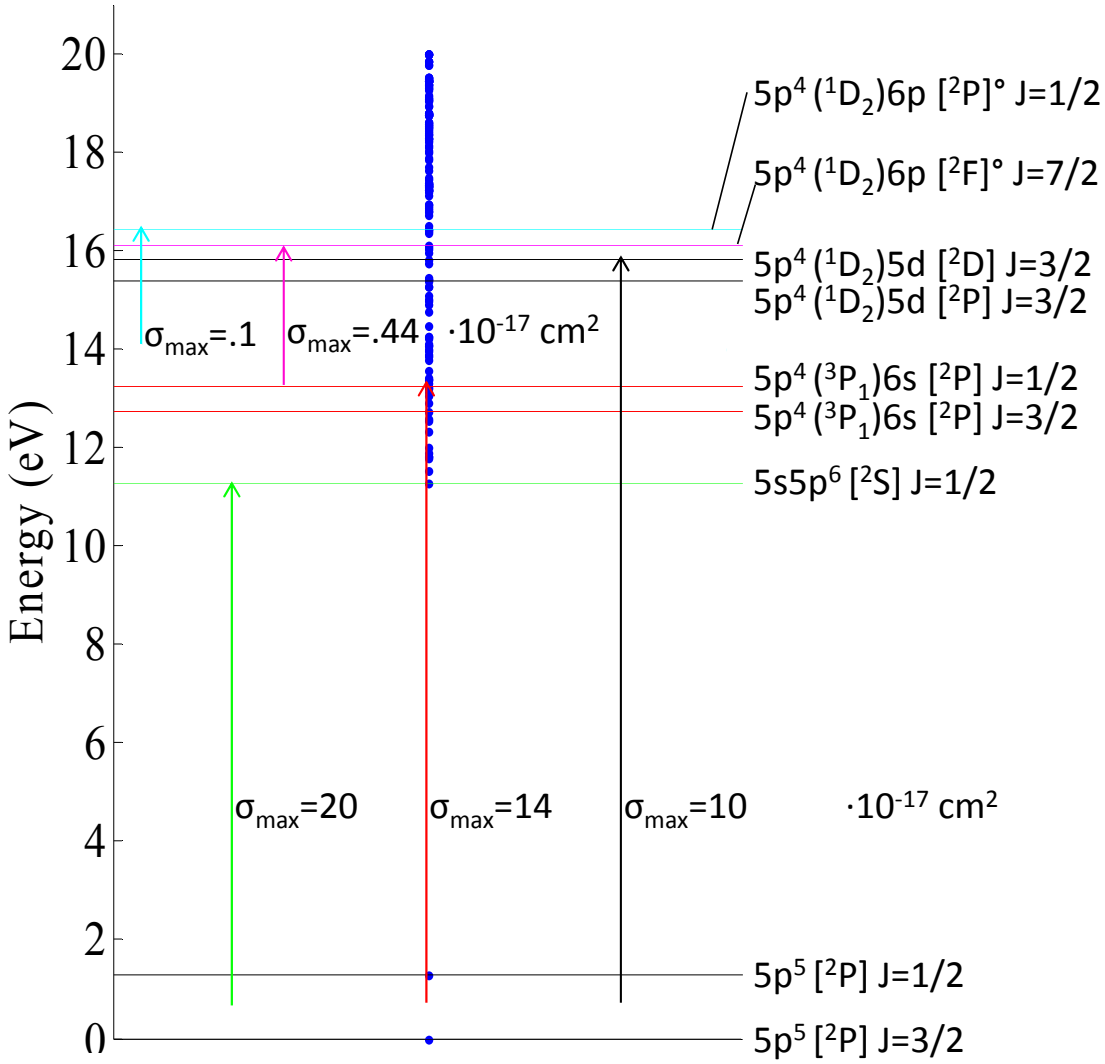

Figure 6.8 Level diagram of Xe^+ with associated Ar^+ excitation cross-sections where available. Blue dots are the energy levels. Excitation cross-sections have been previously measured in argon for transitions analogous to the spin-split ground state to (green) the isolated $5s5p^6\ [^2S]\ J=1/2$ state, (red) the states between the $5p^4\ (^3P_1)6s\ [^2P]\ J=3/2$ and $5p^4\ (^3P_1)6s\ [^2P]\ J=1/2$ states and (black) the states between $5p^4\ (^1D_2)5d\ [^2P]\ J=3/2$ and $5p^4\ (^1D_2)5d\ [^2D]\ J=3/2$. Above ~16eV, states are predominantly populated from low energy excited states instead of the ground state and have smaller excitation cross-sections (cyan and magenta).

6.5 AC Stark Shift and Resonant Multiphoton Ionization

The electron density is shown in Figure 6.9 as a function of driving pulse intensity with and without a prepared Xe^+ plasma. Ionization is observed in the Xe^+ plasma for laser intensities much smaller than those required to ionize neutral xenon gas or Xe^+ from

the ground state. The electron density increases linearly as a function of intensity up to $2.5x10^{13}$ W/cm^2, indicating that single photon ionization of highly excited states is responsible for the ionization beyond that seen in the unprepared gas. However, σ_{max} for ionic xenon states with energy above ~17 eV is orders of magnitude smaller than σ_{max} for the low energy states (below 16 eV) shown in Figure 6.8. No collisional ionization is observed above the SSSI noise floor in the xenon plasma in the absence of the pump pulse, supporting the conclusion that collisional population of high energy ionic states is much smaller than the collisional population of low energy states. The few percent change in the population of low energy excited states predicted from collisional excitation rates and measured by absorption spectroscopy matches the ~5% change in electron density in Xe^+ plasma. However, the much less than one percent predicted collisional excitation of high energy states is too small to explain the observed change in electron density. It is thus puzzling that measurement of electron density as a function of laser intensity indicates the ionization rate is linearly proportional to intensity (Figure 6.9). Non-resonant ionization from the low energy excited states should have a multiphoton characteristic, with an ionization rate proportional to intensity to the nth power where n in this case is five photons. On the other hand, linear ionization as a function of intensity coming from ionization of collisionally excited high energy states should be too small to explain the amount of ionization in Xe^+.

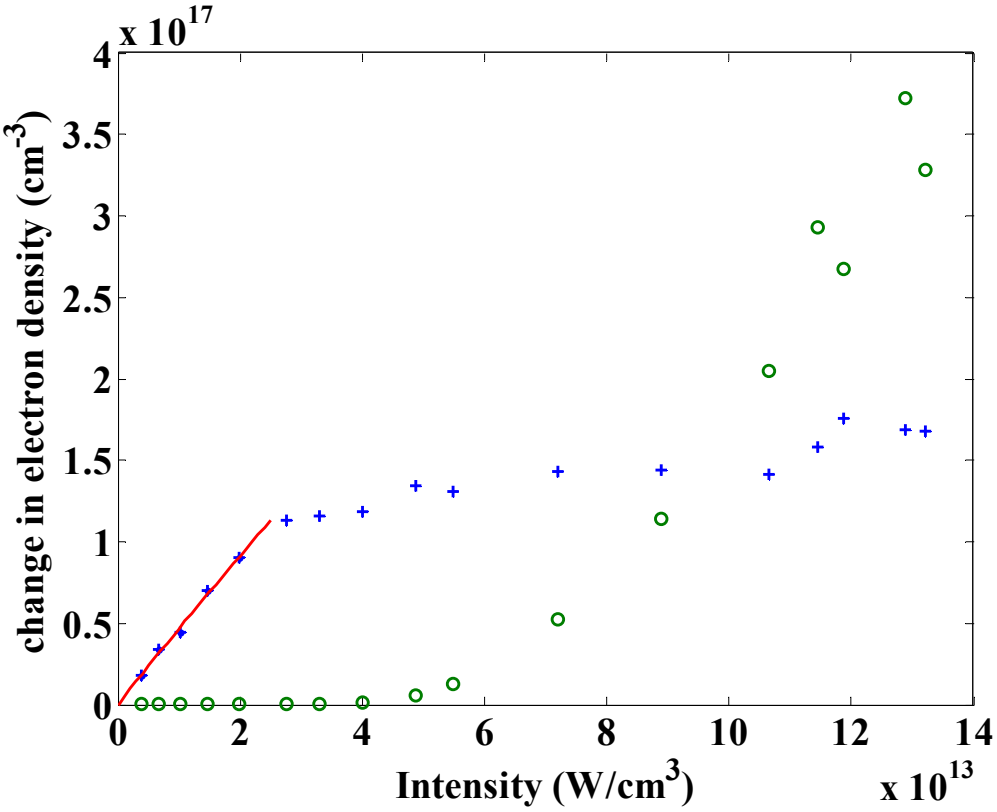

Figure 6.9 Change in electron density due to preparation pulse in Xe (green) and pump pulse in Xe^+ plasma (blue). Contrary to expectations, the ionization threshold of Xe^+ is lower than that of Xe. A power law fit to the Xe^+ ionization curve before saturation gives electron density $N_e \propto I^{0.97\pm.15}$, resembling a single-photon ionization rate (red).

The discrepancy between collisional population rates and the Xe^+ ionization fraction is explained through resonant multiphoton excitation and the AC Stark shift. The transition probability between two states which are exactly one laser photon apart in energy is linearly proportional to intensity, as discussed in chapter 1. In light elements, with large spacing between atomic transitions, it is improbable for an arbitrary laser frequency to be resonant with even one transition. However, in heavy atoms, such as xenon, the excited electronic levels are more closely spaced, and spin splitting further increases the level density. In Xe^+, the largest spacing between adjoining excited levels, neglecting the ground state, is less than .3 eV, compared to nearly 3 eV in Ar^+. As a result, the probability of a resonant transition in heavy atoms is much higher than for light

atoms. In xenon, there are twenty-two electronic transitions which are exactly resonant over the spectrum of a 25 nm bandwidth centered at 800nm (typical for a laser pulse for this system) [74].

To demonstrate the ability of resonant excitations to produce the observed ionization rate, simulations are done for a five level atom with a small but nonzero initial population in each state in a radiation field. The system is modeled using the Bloch equations solved numerically with a 4th order Runge-Kutta solver

$$\dot{\rho}_{mn} = -i\omega_{mn}\rho_{mn} + iF_{mn}(\rho_{nn} - \rho_{mm}) + i\sum_{k\neq m,n}(F_{mk}\rho_{kn} - F_{kn}\rho_{mk}) \tag{6.1}$$

$$\dot{\rho}_{mm} = -i\sum_{k} F_{mk}(\rho_{mk} - \rho_{km}) \tag{6.2}$$

where $\omega_{mn} = \omega_m - \omega_n$ and $F_{mn} = -\frac{e}{\hbar} r_{mn} E$. The Bloch equations give the evolution of the density matrix elements ρ_{mn} with time, assuming a Hamiltonian $H = H_0 - e\vec{r}\cdot\vec{E}$ where $\vec{E}$ is the optical field. The dipole matrix elements $e \cdot r_{mn}$ describe the coupling between states m and n. A complete set of measured dipole moments is not available, so the dipole elements are assumed to be on the order of $e \cdot r_0$ where r_0 is the Bohr radius. Only neighboring states are coupled in the simple model. A large damping term is included for the population of the highest energy state, representing the continuum, so that ionized electrons do not couple back into the system. The lowest level, representing the ground state, has a large energy gap between it and the next nearest state. The other four levels are assumed to be exactly resonant with the field photon energy.

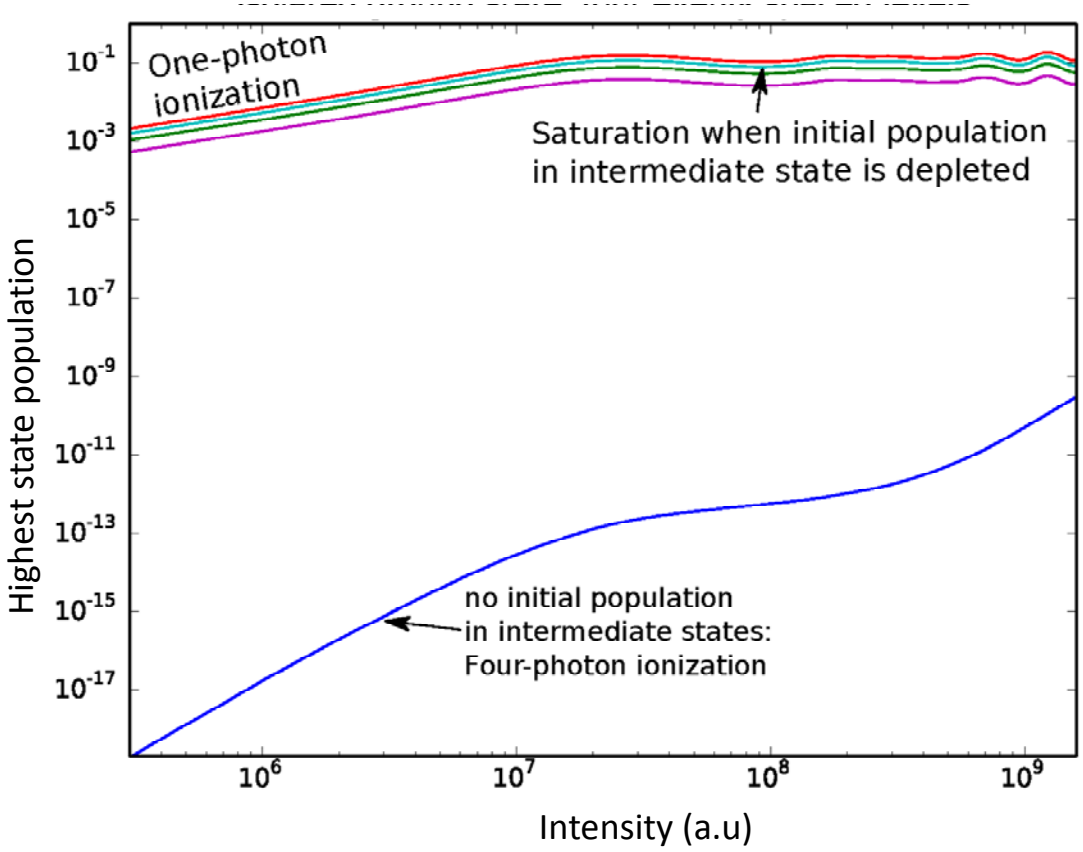

Figure 6.10 Simulation of five level atomic system. The initial population of the lowest intermediate state is 0 (blue) $1 \cdot 10^{-2}$ (purple), $2 \cdot 10^{-2}$ (green), $3 \cdot 10^{-2}$ (cyan), $4 \cdot 10^{-2}$ (red) with each subsequent state having half the initial population of the next lowest state. The ground state contains any population not in the intermediate states, with the total population normalized to one.

In the simulation, a linear ionization rate is observed as a function of intensity, as seen in the experimental data, at low intensities when the excited states start with a few percent population Figure 6.10. Once the excited state population, which is serving as a source of electrons, is depleted, ionization ceases to occur and the continuum population becomes constant. The small observed oscillations in the continuum population after saturation in the simulation are due to non-physical Rabi-flopping between the incompletely damped continuum state and lower excited states. The simulation results are qualitatively a good match for the shape of the observed ionization vs intensity curve

in xenon. Once the low-lying excited state populations are depleted, it is expected that the ionization rate will take on a non-resonant multiphoton characteristic with the ground state serving as a source and 14 photon absorption required to reach ionization. No resonant transition is possible from the ground state to the first excited state due to the 11eV energy gap between them. Thus the population of low energy excited states is critical.

The AC Stark shift of ionic states in an oscillating external field provides an additional component for resonant ionization. The Stark shift arises from modification of the bound electronic state energies due to the external potential provided by the laser field and is proportional to the field intensity [39]. The magnitude of the non-resonant Stark shift of the low-lying excited states, which are more tightly bound than other electronic levels and thus have the smallest shift, may be estimated from measurements of the Stark shift for similar states in neutral xenon. In neutral xenon, an intensity of $2 \cdot 10^{13} \mathrm{W/cm^2}$ is expected to shift the first excited state by .11 ±.05 eV relative to the ground state [80]. The first excited state of ionic xenon is more tightly bound to the atomic core than the analogous state of neutral xenon. The quadratic Stark shift depends on the atomic polarizability α according to

$$\Delta \mathcal{E} = -\frac{1}{2} \alpha E^2 \tag{6.3}$$

$$\alpha = 2e^2 \sum_{n \neq m} \frac{|r_{nm}|^2}{\mathcal{E}_n - \mathcal{E}_m} \tag{6.4}$$

Empirically, the polarizability of heavy atoms scales roughly as $\frac{1}{Z_{eff}}$ [81] so it is expected that the Stark shift for singly ionized xenon will be approximate half that of a

comparable state in neutral xenon. Excited states with energies above ~17eV may be approximated as free electrons and experience Stark shifts relative to the ground state on the order of the ponderomotive potential of the external field [82]

$$U_p = \frac{2\pi e^2}{m_e c}\frac{I}{\omega^2} \tag{6.5}$$

For 800 nm light at an intensity of $2\cdot10^{13}$W/cm^2 , $U_p \approx 1.5$ eV, as large as the energy of a laser photon. Since the ionic xenon is exposed to a laser pulse, with intensity varying from zero to I_{peak} and back during the pulse envelope, the magnitude of the Stark energy level shift takes on all values from zero to ΔE^i_{max} where i indicates a particular state. The estimated maximum shifts are large enough to contribute to the number of direct resonant ionization path from the lowest excited states to the continuum in a Xe^+ plasma in the presence of an external laser pulse. An example of such a transition, from initial state $5p^4(^3P_2)5d\ ^2[2]$ J=3/2 which is observed in the absorption spectra at 597.6 nm [74], is shown in Figure 6.11

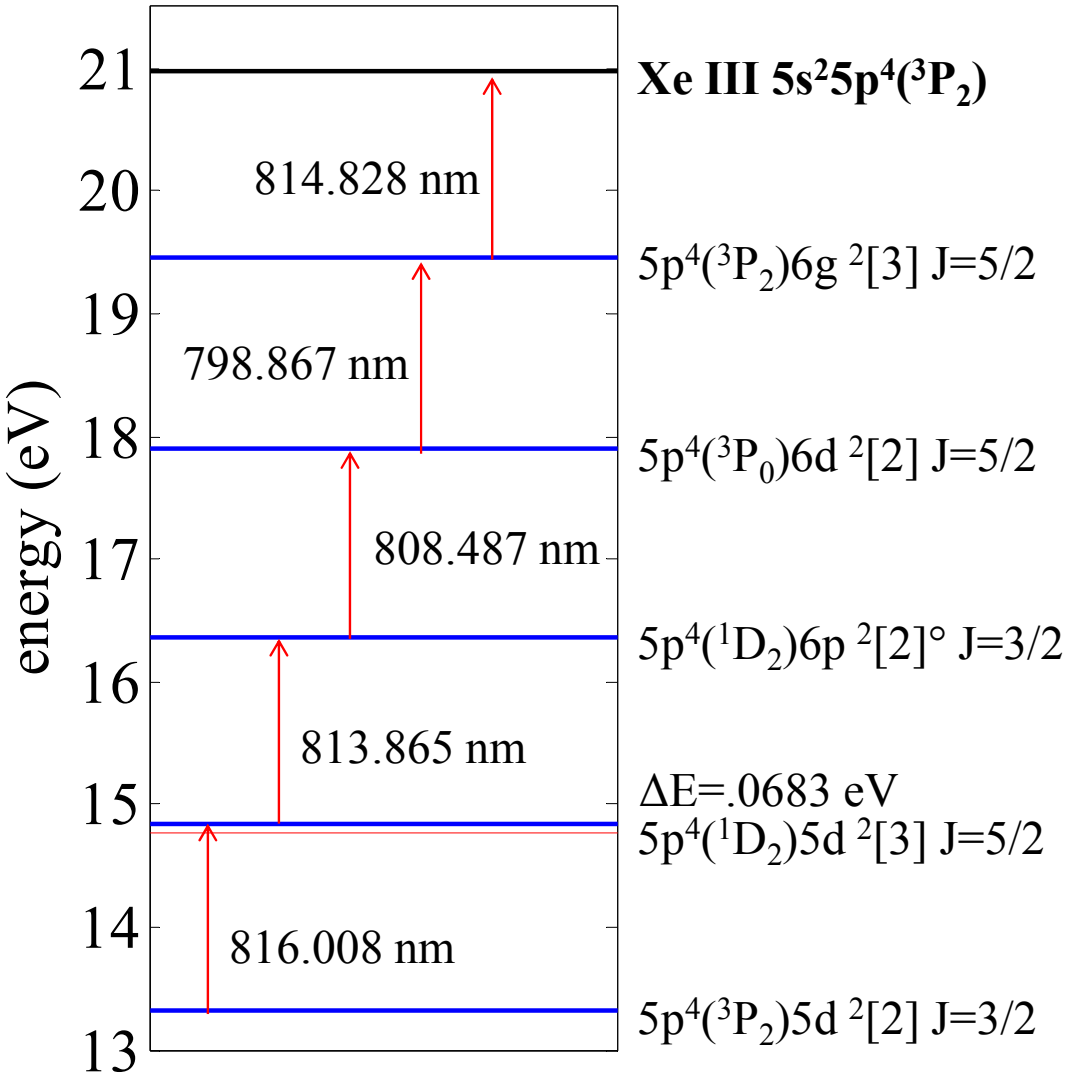

Figure 6.11 One possible completely resonant ionization path from the spectroscopically observed lower state $5p^4(^3P_2)5d\ ^2[2]$ J=3/2 assuming a spectrum with 32nm of bandwidth centered around 800nm. A Stark shift is required for the first absorbed photon, with the unperturbed xenon state shown in red and the shifted state in blue. The Stark shift ΔE=.0683eV relative to the initial state. All other transitions are possible with no shift.

6.5 Conclusions

Generally, the effect of resonant multiphoton ionization in calculation of ionization rates is neglected for ionization by laser pulses which are not tuned to any particular resonance. However, in large atoms and moderate to high intensities this assumption is

no longer valid due to Stark shifting of already closely spaced electronic states. Additionally, collisional excitation is not considered for low density gases. However, this experiment demonstrates that even small collisional excitation rates can significantly alter the behavior of an atomic system. The ionization intensity threshold of heavy atomic gasses with excited state populations is shown to be considerably lower than that calculated from the ionization potential. The Xe^+ plasma medium described above provides a unique opportunity to investigate complex resonant multiphoton ionization processes present in the laser-gas interaction of heavy atoms. Time-resolved absorption spectroscopy may also enable the measurement of AC Stark shifts of excited states which are generally difficult to access and for which no experimental values for dipole moments are available.

Chapter 7 : Progress towards measuring plasma birefringence

7.1 Introduction

There have been several recent publications exploring the concept of birefringence in a plasma medium [83,84]. Non-magnetized plasma is isotropic, so any birefringence effects require a magnetic field of significant strength. In laser-plasma interactions, the magnetic field is supplied by the laser field and is only significant for relativistic intensities, quantified by the normalized vector potential

$$a_0 \equiv \frac{eE_0}{m_e \omega c} = \sqrt{\frac{I\lambda^2[\mu m]}{1.37\times 10^{18}}} \tag{7.1}$$

Magnetic field effects begin to be noticeable around $a_0 \approx .1$. For a Ti:Sapphire laser with center wavelength 800nm, this corresponds to an intensity I~$2.4\cdot 10^{16}$ W/cm^2, easily achievable with today's laser technology.

Birefringent plasma could possibly be used in place of traditional polarizing optics for high intensity applications where solid materials suffer catastrophic breakdown [83]. Birefringence in plasma has been observed previously due to a plasma grating induced by intensity modulations imposed on a gas during ionization [85]. The intensity modulations are a result of interference between a degenerate pump and probe propagating with a 45 degree angle between them and cause corresponding modulations in the electron density. A perturbation theory analysis of plasma in the presence of a relativistic, linearly polarized strong laser pulse (the pump) done to lowest order in the probe normalized vector potential predicts a difference in the laser-induced change in index of refraction probed parallel to the pump pulse (x-direction) compared to that

probed perpendicular to the pump pulse (y-direction) [84] due to the relativistic quiver energy of the electrons in the direction parallel to the driving electric field.

$$\Delta n'_y - \Delta n'_x \approx \frac{k_p{}^4 a_0{}^2}{8\left(1+a_0{}^2/2\right)^2 k'^2}\left(\frac{1}{k_+{}^2}+\frac{1}{k_-{}^2}\right) \tag{7.2}$$

Here the prime refers to the probe pulse (ie *k'* is the probe wave-number), $k_p = \frac{c}{\omega_p}$ is the plasma wave-number (the plasma frequency $\omega_p \equiv \sqrt{\frac{4\pi e^2 N_e}{m_e}}$), and $k_\pm \equiv k \pm k'$ is the sum (difference) of the strong pulse and probe wave-numbers. Eq (7.2) refers to the case of a non-degenerate pump and probe. Assuming realistic parameters for an experiment with the Ti:Sapphire laser system discussed in chapter 3 (I=4.3·10^{17}W/cm^3, $a_0 = .5$, $N_e = 4\times10^{18}$ electrons/cm^3, $\lambda' = 600nm$, $\lambda = 800nm$, interaction length L=400μm) Eq (7.2) predicts a phase shift of 3 mrad. 3 mrad is near the noise floor of the SSSI technique. Tsaur et al [84] checked their perturbation solution against 1D particle in cell (PIC) simulations which agree with the theory, but no attempt was made to verify that the results hold for higher dimensions. Since birefringence is an intrinsically 2D phenomenon, the PIC code Turbo Wave [86] is used to extend the simulation results. A linearly polarized 100 fs laser pulse with peak normalized vector potential $a_0 = 0.25$ is propagated through a 640 μm thick plasma slab with electron density 7.2·10^{18} cm^{-3}. Two weak broadband probes polarized parallel and perpendicular relative to the strong pulse co-propagate through the plasma. The difference in phase shift between the two probes

for light with wavelength 675 nm is extracted after the laser pulses exit the plasma. In the 1D PIC code, the resulting phase difference is 11 mrad, compared to 2D results with phase difference 8 mrad [87]. 3D simulations are currently underway.

7.2 Experiment

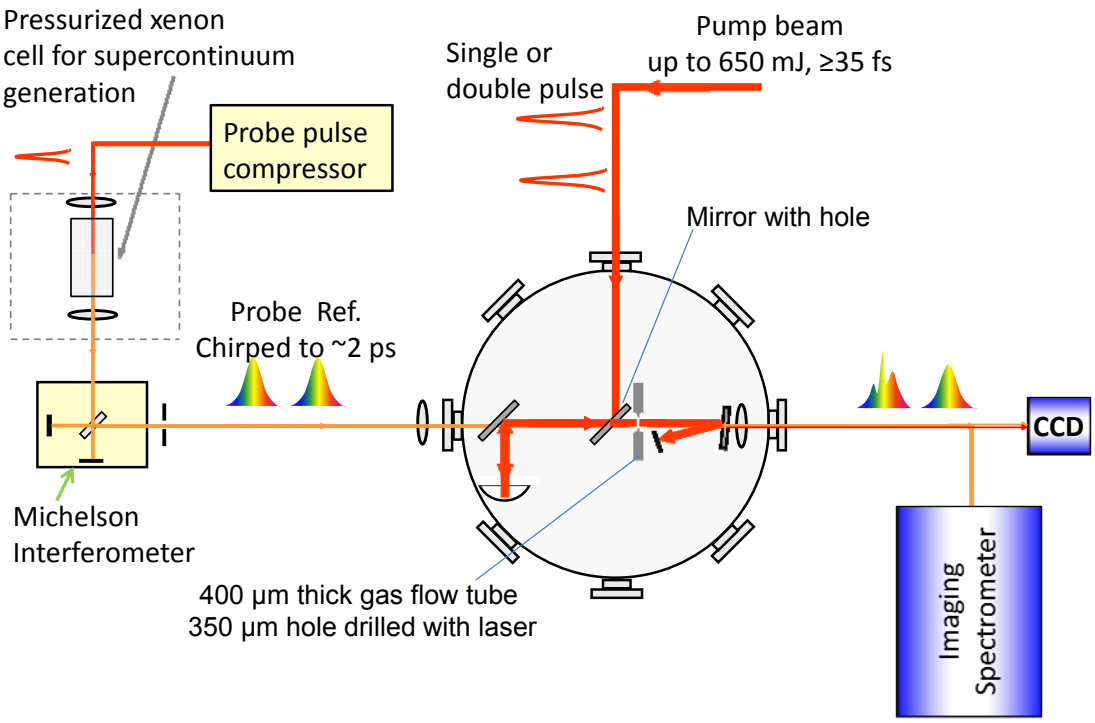

Figure 7.1 Diagram of experimental set-up. The pump pulse is focused using a spherical mirror, which retroreflects the beam through a small hole drilled in one of the turning mirrors.

The experimental layout is shown in Figure 7.1. The beam for generating the supercontinuum pulse for the SSSI probe and reference pulses comes from leakage through an 800nm broadband dielectric mirror in the Ti:Sapphire multipass amplifier before the beam is directed to the vacuum compressor. The probe is independently compressed in a single grating compressor to 60 fs, and contains approximately 300µJ of IR energy after compression. The compressor diffraction grating ruling is 1500 lines/mm, and the compressor is designed to compensate $1.7 \cdot 10^6$ fs^2 group delay

dispersion and $1.1 \cdot 10^6$ fs^3 third order dispersion. The dispersion compensation is based upon the geometry of the pump beam compressor, using the well-known equations for second and third order dispersion [88]

$$\phi_2 = \frac{b\lambda_0^3}{\pi c^2 d^2} \frac{1}{1-(\lambda_0/d - Sin[\gamma])^2} \tag{7.3}$$

$$\phi_3 = \left.\frac{d\phi_2}{d\omega}\right|_{\omega_0} = \frac{3\lambda_0}{2\pi c} \frac{b\lambda_0^3}{\pi c^2 d^2} \frac{1}{1-(\lambda_0/d - Sin[\gamma])^2} (1 - \lambda_0/d \frac{(\lambda_0/d - Sin[\gamma])}{1-(\lambda_0/d - Sin[\gamma])^2}) \tag{7.4}$$

where b is the path length between the first and second grating reflections, d is the spacing of the grating grooves, λ_0 is the center wavelength of the laser, and γ is the incident angle of light onto the grating. The supercontinuum probe is polarized 45° relative to the pump polarization. After the interaction region, the probe is separated into parallel and perpendicularly polarized beams of approximate equal energy so that the difference in phase shift due to the plasma birefringence may be measured.

The main laser pulse is focused using a spherical mirror to retro-reflect the beam through a hole drilled in the center of one of the input mirrors. After phase front optimization using a deformable mirror, the main focal spot is elliptical with a full width at half maximum of 12.5μm in the vertical direction and 16.2μm in the horizontal direction Figure 7.2. 90% of the total intensity is contained within the Gaussian central spot. The ring around the central spot in the focal profile is due to the mirror with a hole drilled through it, which removes the center of the unfocused beam. The hole is 4mm in diameter, compared to the 4cm collimated beam. The Rayleigh range of 500μm is measured by using the deformable mirror to move the focal spot location axially and recording the location where the peak intensity drops by a factor of two. The SSSI probe

is focused more gently and significantly overfills the main beam spot, with a FWHM spot size of 220μm. The interaction region is defined by a thin flow tube as discussed in chapter 2, with an approximate interaction length of 400μm. The center of the interaction region is imaged onto the spectrometer.

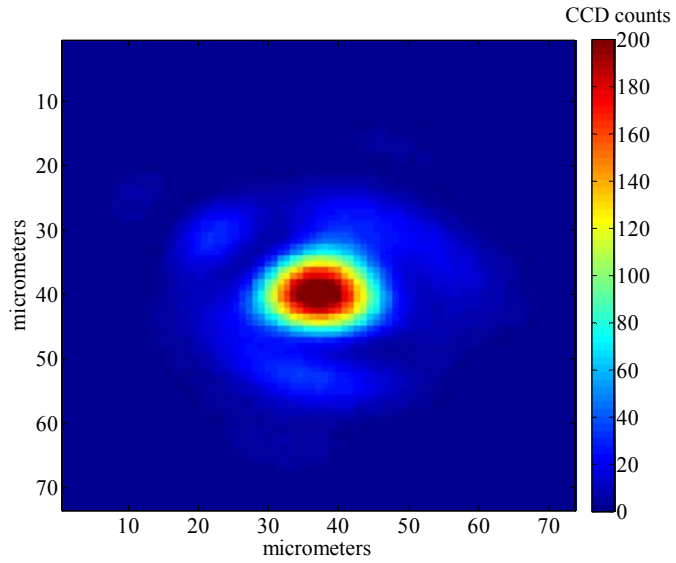

Figure 7.2 Pump focal spot

The predicted birefringence should only occur when pump and probe are temporally overlapped. The strong phase shift of the probe due to ionization is expected to swamp the small difference in phase shift from birefringence. The experiment is therefore designed to include a pre-pulse with enough energy to fully pre-ionize the gas. The pre-pulse is created by placing a thin window before the last mirror of the multi-pass amplifier. The window is used at nearly 0°, and reflects approximately 5% of the incident laser light. See the diagram in Figure 7.3. With 300mJ of incident laser energy ($I= 4.3\cdot10^{17}$ W/cm^2, $a_0 \sim .4$ for 70 fs pulse and the measured focal spot) the pre-pulse contains 15mJ, which is more than enough to completely ionize 100 Torr of hydrogen.

The time delay between the pre-ionizing pulse and main pump pulse is controlled by changing the spacing between the window and multi-pass mirror.

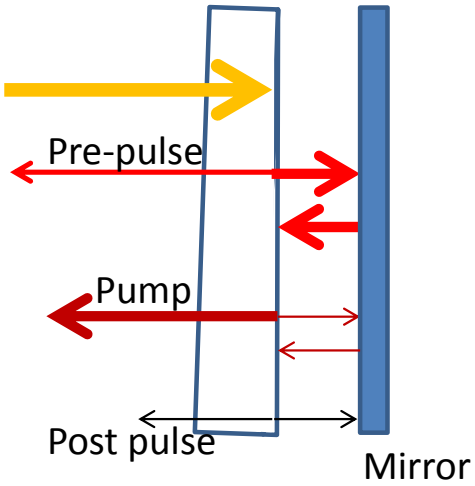

Figure 7.3 Diagram of pre-pulse generation. The window is slightly wedged, so that only one pre-pulse copropagates with the pump pulse. The pre-pulse from the first surface reflection of the window is not aligned to the pump spot location. The pre-pulse contains approximately 5% of the incident energy. The small set of post pulses contains negligible energy.

Supercontinuum (SC) generation by the pump laser pulse saturates the SSSI spectrometer CCD at high gas pressures, overlapping the probe SC spectrum and making phase extraction of the probe pulse impossible. In practice, the gas pressure must be kept below 100 Torr with a pump pulse duration of 70 fs or greater to reduce the pump's undesirable SC generation enough to make SSSI useable. At lower pressures, where the unwanted SC generation does not saturate the CCD but is still visible on the spectrometer, its contribution reduces the signal-to-noise ratio in the SSSI phase maps during the ionization time window. Introduction of a pre-ionizing pulse is expected to eliminate this noise by placing the ionization process outside the SSSI time window, although the limitations imposed by undesirable SC saturation of the CCD remain. Two roots blower vacuum pumps are used in series to maintain a low background pressure.

Vibrations from the vacuum pumps couple to the experimental chamber and introduce significant shot-to-shot transverse spatial jitter of the pump focal spot and temporal jitter between the pump and probe pulse arrival times in the interaction region. A box filled with sand is placed around the vacuum line and reduces the vibrational noise by a factor of two, but jitter is still a significant problem. It is possible to adjust for this jitter during the data processing (see Appendix A) but generally the vacuum pump closest to the experiment is simply turned off during data acquisition, which reduces the jitter to below detectable levels. The background pressure remains below 1 Torr even with one vacuum pump off.

7.3 Preliminary results

To test the SSSI set-up, a single high energy pulse was focused into the gas tube backed with 50 Torr hydrogen gas. The resulting phase map is shown in **Error! Reference source not found.** for two pulse energies, along with a one-dimensional plot of the phase verses time for two transverse spatial locations. At an energy of 5mJ, the onset of ionization is visible. The transverse dimension of the plasma is larger than the central Gaussian focal spot, but matches well with the focal spot width if energy in the outer ring is taken into account. The maximum phase shift saturates at 50mJ, and the transverse extent of the ionization region widens to fill the hole in the gas tube. A region of decreased phase shift begins to form at the center of the focal spot as the laser energy increases further. At 200 mJ, the phase map has a pronounced trench with a FWHM of approximately 15μm, which corresponds closely to the width of the Gaussian portion of the focal spot in the vertical dimension, which is projected along the slit. It is not clear yet what is causing the decrease in phase shift. During the laser pulse, the ponderomotive

force is expected to eject electrons from the high intensity region of the focus while the heavier ions remain stationary. This is consistent with the location of the decreased phase. However, after the laser pulse the Coulomb force between the stationary ions and electrons should cause the electron density in the central region to increase, creating an electrostatic plasma wave. The plasma period for 50 Torr (electron density $1.7 \cdot 10^{17}$ cm^{-3}) is 80fs, so any plasma wave will be clearly visible along the temporal axis of the phase map. There is no evidence of a plasma wave. Furthermore, for a_0 =.25and 75 Torr pressure, 2D PIC simulations predict the ponderomotive phase shift to be ~30mrad. The phase dip observed in Figure 7.4(a) is too large. Other possible explanations are refraction of the probe due to background gas in the vacuum chamber outside the gas flow tube or ionization prior to the reference pulse arrival by a pre-pulse. The source of the phase trench is currently under study. Observation of a plasma wave similar to the results of [46] is an immediate goal, to demonstrate the functionality of the SSSI diagnostic on the 25 TW laser system prior to observation of the small phase shift signal due to plasma birefringence.

The noise floor of the SSSI diagnostic is visible in Figure 7.4(c) and has a value of 25mrad, which is too high to detect the expected phase difference due to plasma birefringence. A number of avenues to decrease the noise floor are planned for study and discussed in the concluding chapter.

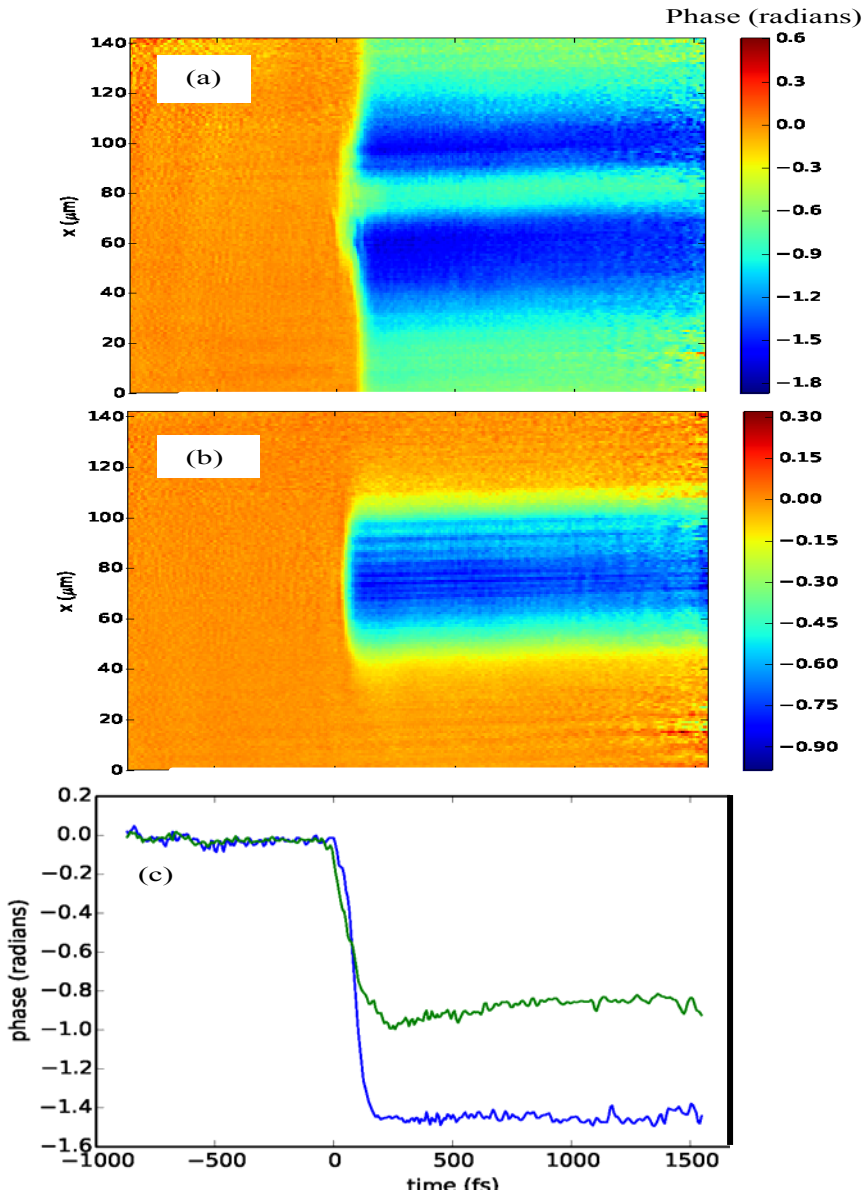

Figure 7.4 (a) 2D phase map for 200mJ incident energy. (b) 2D phase map for 5 mJ pulse energy. (c) Average of ten horizontal lineouts from (a) at centered at 80μm (green) and 100μm (blue)

7.4 Current status of the experiment

The construction of a beam line and diagnostic is complete and sources of noise are now being isolated and removed. An operable range of parameters has been found and PIC simulations with these parameters as inputs are being run in support of the experiment. Generation of a pre-ionizing pulse which fully ionizes hydrogen at the

desired pressures has been demonstrated. An upper limit for temporal jitter is measured to be 20 fs, so laser-driven ponderomotive plasma waves should be clearly resolvable. Work remains to be done in identifying and eliminating sources of noise in the SSSI diagnostic to reach the target noise floor.

Chapter 8 : Conclusions and future work

8.1 Electron Density and Spectroscopy Measurements of Plasma Columns for Atmospheric Lasing

It is possible to generate plasma with a large population of molecular nitrogen remaining after ionization using a few mJ short pulse laser. The plasma density in such a process is on the order of 10^{16}electrons/cm^3. A longer pulse containing two orders of magnitude more energy focused into the plasma column can be used to increase the electron temperature, as evidenced by an increase in recombination emission of the plasma. There is no evidence of a population inversion generated between the $C^3\prod_u$ v'=0 and $B^3\prod_g$ v''=0 states of molecular nitrogen. It may be that the electron temperature remains too small or that a recombination path other than the theorized mechanism [67,68] dominates.

Despite the lack of lasing in the heated nitrogen plasma studied in chapter four, the idea of heating a tenuous plasma using a longer laser pulse is an area of current study [75,89,90]. In a laser heated plasma with a non-Maxwellian electron distribution it is not easy to measure the electron energy distribution function, which is of critical importance in quantifying the efficiency of laser heating. However, time-resolved absorption spectroscopy using a light source which spans the near UV to near IR, covering the strong absorption lines in molecular and slightly ionized nitrogen, would allow limits to be placed on the electron heating. The xenon supercontinuum source used in chapters five and six is well-suited to this application. Absolute absorption measurements could also be compared to the estimated electron densities which are somewhat in doubt due to the strong effect of refraction. Finally, only electron densities

for the igniter-generated plasma were measured in this work. It would be of great interest to measure the density of the heated plasma, which requires a probe which may be separated either through polarization or wavelength from the 800nm igniter and the 1064nm heater pulses.

8.2 Resonant multiphoton ionization of Xe+

A few percent ionization in plasma consisting primarily of Xe^+ is observed for incident laser intensities well below the expected ionization threshold. Furthermore, the amount of ionization increases as a function of time after plasma generation over several picoseconds, when the ionization at low incident intensities saturates. Comparison of experimental electron density measurements as a function of incident laser intensity with simulations of a five level atom indicates that the low intensity ionization mechanism is a two-step process. First, excited states of Xe^+ are collisionally populated over several picoseconds. Second, resonant multiphoton ionization, having a linear dependence on incident intensity, occurs until the excited state population is depleted. AC Stark shifts of the excited levels may contribute to the number of possible resonant ionization pathways. As demonstrated by the time-dependence of absorption strength in krypton, the collisional population of excited states on the picosecond timescale is not unique to xenon. However, it has not yet been demonstrated that the resonant multiphoton ionization of atoms applies to krypton or smaller atoms. It is not possible with the laser used in this investigation to fully ionize neutral krypton, let alone smaller atoms like argon or neon. Once the SSSI diagnostic is shown to be operable on the 25 TW laser system discussed in chapter 6, it will be straightforward to extend the investigation of ionization of pre-ionized plasma to other species. For smaller atoms, with larger spacing

between excited states, it is expected that the ionization signal should decrease or disappear altogether. In this case, it should be possible to execute the originally intended experiment-measuring the nonlinear index of refraction of an ion species.

8.3 Plasma birefringence

An experiment has been designed and constructed to measure a hypothesized birefringent effect in plasma. Efforts are underway to completely characterize the diagnostic and reduce the noise floor to a level below the proposed signal. PIC simulations in support of the experiment are currently being run.

A great deal of work remains to be done on this experiment. Beyond identifying artifacts currently contaminating the data, it is clear that the signal-to-noise ratio must be increased observe the extremely small birefringent plasma signal. Possibly the simplest method to increase the signal is to increase the supercontinuum brightness on the spectrometer slit. This may be done by focusing the existing supercontinuum more tightly, to raise the intensity on the slit. In the current experimental geometry the focal length of the supercontinuum lens is limited by the position of the dielectric mirror through which the supercontinuum couples to the IR pump beam path. The focal length could be shortened by at most 10 cm, increasing the focused intensity by approximately 25%. Changing the lens would also decrease the observable transverse region of plasma, which is undesirable. Alternatively, the supercontinuum energy may be increased. Using the current supercontinuum generation technique, the conversion efficiency from IR to supercontinuum is limited by the filamentation process. Increasing the IR energy input into xenon cell above the critical power for filamentation causes multiple filaments [71], which destabilizes the supercontinuum output and increases the SSSI noise floor.

Recently, a new supercontinuum generation method was discovered [91] which could be used to increase the supercontinuum intensity by a factor of ten or more. Glass cover slips placed where the xenon pressure cell currently resides will enable testing of this concept quickly and without major construction. Signal may also be increased by decreasing the temporal spacing between SSSI probe and reference, which will increase the spectrometer interference fringe contrast. For zero time delay between probe and reference the fringe contrast increases by a factor of two. With a single Michelson interferometer the minimum time delay between the reference and probe is set by the need for the reference to pass through the interaction region before plasma formation. A second Michelson may be added after the interaction region, so that the time delay between the probe and reference at the interaction point is set to be large with the first Michelson and shifted to zero with the second interferometer. It is questionable how much signal will be gained using this method, since the second Michelson cuts the supercontinuum intensity by a factor of two. However, the double interferometer system has the additional advantage of increasing the possible time delay between reference and probe so that the reference may be placed before any pump pre-pulse arrives which will aid in diagnosis of SSSI artifacts.

Focusing the pump laser beam using an off-axis parabola would have several advantages over the current focusing scheme using a spherical mirror. First, the drilled mirror could be eliminated from the beam path so that the focal spot no longer has an outer ring. The ionized region in the transverse direction would be smaller, allowing a smaller hole in the gas tube. There is some speculation that current artifacts are due to gas leaking out of the flow tube to fill a larger than expected axial region. A flow tube

with a smaller hole would mitigate this effect. Second, the pump and supercontinuum probe would no longer be forced to perfectly co-propagate. A slight angle between pump and probe would remove the signal contamination from pump-induced supercontinuum generation, allowing operation at shorter pulse durations and higher densities, both of which are expected to increase the measured phase shift.

Appendices

A.1 Jitter compensation in SSSI

For measurements which are stable from shot-to-shot and requiring very high phase shift sensitivity, the single-shot interferograms may be averaged over hundreds to thousands of shots. For the high power Ti:Sapphire laser system used in chapter 6, small timing jitter between the reference and probe pulses originating from vibrations in the Michelson interferometer causes interferograms to average to zero and must be taken into account during data analysis. A small change in path length in one of the interferometer arms will change the location of maxima and minima in the interferograms, eliminating the signal to noise improvement from averaging interferograms. This small jitter may be compensated in the data analysis by inserting an artificial time delay into each data set, such that the phase for a given pixel of the detector CCD is constant. The correction is only possible for small vibrations, such that the change in phase between shots is less than pi. The fringe contrast is increased by better than a factor of three using jitter compensation, significantly improving the signal to noise ratio. See Figure A1.1

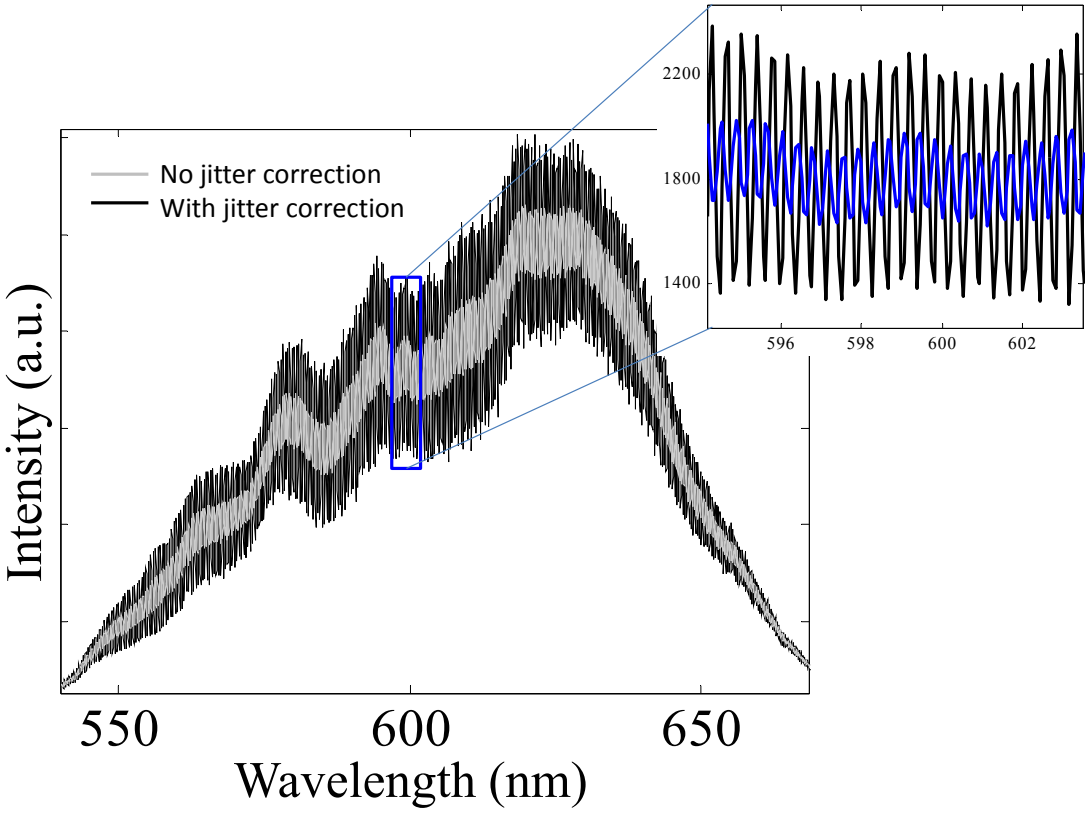

Figure A1.1 One dimensional lineout of spectral interference pattern as a function of spectrometer wavelength. Jitter correction during data processing improves the interference fringe depth by better than a factor of three.

Bibliography

[1] J. Meijer, K. Du, A. Gillner, D. Hoffmann, V. S. Kovalenko, T. Masuzawa, A. Ostendorf, R. Poprawe, and W. Schulz, CIRP Ann. - Manuf. Technol. **51**, 531 (2002).

[2] I. Ratkay-Traub, T. Juhasz, C. Horvath, C. Suarez, K. Kiss, I. Ferincz, and R. Kurtz, Ophthalmol. Clin. North Am. **14**, 347 (2001).

[3] R. A. Ganeev, *Laser - Surface Interactions* (Springer Netherlands, Dordrecht, 2014).

[4] S. P. D. Mangles, C. D. Murphy, Z. Najmudin, A. G. R. Thomas, J. L. Collier, A. E. Dangor, E. J. Divall, P. S. Foster, J. G. Gallacher, C. J. Hooker, D. A. Jaroszynski, A. J. Langley, W. B. Mori, P. A. Norreys, F. S. Tsung, R. Viskup, B. R. Walton, and K. Krushelnick, Nature **431**, 535 (2004).

[5] S. V. Bulanov and V. S. Khoroshkov, Plasma Phys. Reports **28**, 453 (2002).

[6] A. L. Cavalieri, N. Müller, T. Uphues, V. S. Yakovlev, A. Baltuska, B. Horvath, B. Schmidt, L. Blümel, R. Holzwarth, S. Hendel, M. Drescher, U. Kleineberg, P. M. Echenique, R. Kienberger, F. Krausz, and U. Heinzmann, Nature **449**, 1029 (2007).

[7] N. Jhajj, E. W. Rosenthal, R. Birnbaum, J. K. Wahlstrand, and H. M. Milchberg, Phys. Rev. X **4**, 011027 (2014).

[8] P. Franken, A. Hill, C. Peters, and G. Weinreich, Phys. Rev. Lett. **7**, 118 (1961).

[9] M. Bass, P. Franken, A. Hill, C. Peters, and G. Weinreich, Phys. Rev. Lett. **8**, 18 (1962).

[10] J. Giordmaine and R. Miller, Phys. Rev. Lett. **14**, 973 (1965).

[11] C. C. Wang and G. W. Racette, Appl. Phys. Lett. **6**, 169 (1965).

[12] Y. R. Shen, *The Principles of Nonlinear Optics* (John Wiley & Sons, Inc, New Jersey, 2003).

[13] A. Yariv and D. M. Pepper, Opt. Lett. **1**, 16 (1977).

[14] D. Burnham and D. Weinberg, Phys. Rev. Lett. **25**, 84 (1970).

[15] R. Boyd, *Nonlinear Optics*, Third Edit (Elsevier, Burlington, 2008).

[16] D. E. Spence, P. N. Kean, and W. Sibbett, Opt. Lett. **16**, 42 (1991).

[17] M. Piché, Opt. Commun. **86**, 156 (1991).

[18] J. K. Wahlstrand, Y.-H. Cheng, and H. M. Milchberg, Phys. Rev. A **85**, 043820 (2012).

[19] J. K. Wahlstrand, Y.-H. Cheng, Y.-H. Chen, and H. M. Milchberg, Phys. Rev. Lett. **107**, 103901 (2011).

[20] Y. Chen, The Ultrafast Nonlinear Response of Air Molecules and Its Effect on Femtosecond Laser Plasma Filaments in Atmosphere, University of Maryland, 2011.

[21] Y.-H. Chen, S. Varma, A. York, and H. M. Milchberg, Opt. Express **15**, 11341 (2007).

[22] L. V. Keldysh, Sov. Phys. JETP **20**, 1307 (1965).

[23] V. S. Popov, Physics-Uspekhi **47**, 855 (2004).

[24] A. Perelomov and V. Popov, Sov. Phys. JETP **25**, 336 (1967).

[25] A. Nikishov and V. Ritus, Sov. Phys. JETP **25**, 145 (1967).

[26] A. A. Radzig and B. M. Smirnov, *Reference Data on Atoms, Molecules, and Ions* (Springer Berlin Heidelberg, Berlin, Heidelberg, 1985).

[27] D. R. Hartree, Math. Proc. Cambridge Philos. Soc. **24**, 111 (2008).

[28] M. V Ammosov, N. B. Delone, and V. P. Krainov, Sov. Phys. JETP **91**, 1191 (1986).

[29] N. Delone and V. Krainov, *Multiphoton Processes in Atoms* (Springer-Verlag, Heidelberg, Berlin, 2012).

[30] F. H. M. Faisal, J. Phys. B At. Mol. Phys. **6**, L89 (1973).

[31] H. Reiss, Phys. Rev. A **22**, 1786 (1980).

[32] H. Reiss, Phys. Rev. A **42**, 1476 (1990).

[33] H. R. Reiss, J. Opt. Soc. Am. B **7**, 574 (1990).

[34] H. Reiss, Phys. Rev. Lett. **101**, 043002 (2008).

[35] M. Klaiber, E. Yakaboylu, and K. Hatsagortsyan, Phys. Rev. A **87**, 023418 (2013).

[36] V. D. Mur, B. M. Karnakov, and V. S. Popov, J. Exp. Theor. Phys. **87**, 433 (1998).

[37] S. Popruzhenko, V. Mur, V. Popov, and D. Bauer, Phys. Rev. Lett. **101**, 193003 (2008).

[38] N. Delone and V. Krainov, Physics-Uspekhi **669**, 669 (1999).

[39] J. S. Bakos, Phys. Rep. **31**, 209 (1977).

[40] L. Kotova and M. Terent'ev, Sov **25**, 481 (1967).

[41] R. M. Potvliege, Comput. Phys. Commun. **114**, 42 (1998).

[42] D. Bauer and P. Koval, Comput. Phys. Commun. **174**, 396 (2006).

[43] E. Esarey, C. Schroeder, and W. Leemans, Rev. Mod. Phys. **81**, 1229 (2009).

[44] A. V. Bashinov and A. V. Kim, Phys. Plasmas **20**, 113111 (2013).

[45] E. Tokunaga, A. Terasaki, and T. Kobayashi, Opt. Lett. **17**, 1131 (1992).

[46] N. H. Matlis, S. Reed, S. S. Bulanov, V. Chvykov, G. Kalintchenko, T. Matsuoka, P. Rousseau, V. Yanovsky, a. Maksimchuk, S. Kalmykov, G. Shvets, and M. C. Downer, Nat. Phys. **2**, 749 (2006).

[47] J.-P. Geindre, P. Audebert, S. Rebibo, and J.-C. Gauthier, Opt. Lett. **26**, 1612 (2001).

[48] C. Y. Chien, B. La Fontaine, A. Desparois, Z. Jiang, T. W. Johnston, J. C. Kieffer, H. Pepin, F. Vidal, and H. P. Mercure, Opt. Lett. **25**, 578 (2000).

[49] A. Benuzzi-Mounaix, M. Koenig, J. M. Boudenne, T. A. Hall, D. Batani, F. Scianitti, A. Masini, and D. Di Santo, Phys. Rev. E **60**, 2488 (1999).

[50] K. Y. Kim, I. Alexeev, and H. M. Milchberg, Appl. Phys. Lett. **81**, 4124 (2002).

[51] Y.-H. Chen, S. Varma, I. Alexeev, and H. Milchberg, Opt. Express **15**, 7458 (2007).

[52] P. Chessa, E. De Wispelaere, F. Dorchies, V. Malka, J. R. Marquès, G. Hamoniaux, P. Mora, and F. Amiranoff, 3 (1999).

[53] K.-Y. Kim, MEASUREMENT OF ULTRAFAST DYNAMICS IN the Interaction of Intense Laser Pulses with Gases, Atomic Clusters, and Plasmas, University of Maryland, 2003.

[54] K. Kim, I. Alexeev, and H. Milchberg, Opt. Express **10**, 1563 (2002).

[55] E. Tokunaga and A. Terasaki, J. Opt. Soc. Am. B. **13**, 496 (1996).

[56] K. Y. Kim, V. Kumarappan, and H. M. Milchberg, Appl. Phys. Lett. **83**, 3210 (2003).

[57] M. Takeda, H. Ina, and S. Kobayashi, J. Opt. Soc. Am. **72**, 156 (1982).

[58] C. Dorrer, N. Belabas, J. Likforman, and M. Joffre, **17**, 1795 (2000).

[59] Y.-H. Cheng, High Field Optical Nonlinearities in Gases, University of Maryland, 2013.

[60] D. Marcuse, *Theory of Dielectric Optical Waveguides*, Second (Academic Press, Inc, San Diego, CA, 1991).

[61] C. R. Pollock, *Fundamentals of Optoelectronics* (Irwin, 1995), p. 569.

[62] C. G. Durfee, Plasma Waveguide for High Intensity Laser Pulses, University of Maryland, 1994.

[63] P. G. Gobbi and G. C. Reali, Opt. Commun. **52**, 195 (1984).

[64] D. Strickland and G. Mourou, Opt. Commun. **56**, 219 (1985).

[65] H. G. Heard, Nature **200**, 667 (1963).

[66] A. Ali, A. C. Kolb, and A. D. Anderson, Appl. Opt. **6**, 2115 (1967).

[67] P. Sprangle, J. Penano, B. Hafizi, D. Gordon, and M. Scully, Appl. Phys. Lett. **98**, 211102 (2011).

[68] J. Peñano, P. Sprangle, B. Hafizi, D. Gordon, R. Fernsler, and M. Scully, J. Appl. Phys. **111**, 033105 (2012).

[69] D. Kartashov, S. Ališauskas, G. Andriukaitis, A. Pugžlys, M. Shneider, A. Zheltikov, S. L. Chin, and A. Baltuška, Phys. Rev. A **86**, 033831 (2012).

[70] Q. Luo, W. Liu, and S. L. Chin, Appl. Phys. B Lasers Opt. **76**, 337 (2003).

[71] A. Couairon and A. Mysyrowicz, Phys. Rep. **441**, 47 (2007).

[72] Y.-H. Chen, S. Varma, T. M. Antonsen, and H. M. Milchberg, Phys. Rev. Lett. **105**, 215005 (2010).

[73] A. Lofthus and P. H. Krupenie, J Phys Chem Ref Data **6**, 113 (1977).

[74] A. Kramida, Y. Ralchenko, J. Reader, and N. A. Team, NIST At. Spectra Database (ver 5.2) (2014).

[75] P. Polynkin, B. Pasenhow, N. Driscoll, M. Scheller, E. M. Wright, and J. V. Moloney, Phys. Rev. A **86**, 043410 (2012).

[76] L. Shi, W. Li, D. Bai, H. Zhou, D. Wang, L. Ding, and H. Zeng, Phys. Rev. A **88**, 013418 (2013).

[77] L. Shi, W. Li, Y. Wang, X. Lu, L. Ding, and H. Zeng, Phys. Rev. Lett. **107**, 095004 (2011).

[78] L. Shi, W. Li, H. Zhou, L. Ding, and H. Zeng, Opt. Lett. **38**, 398 (2013).

[79] I. P. Zapesochnyi, A. I. Imre, and Y. N. Semenyuk, JETP **99**, 721 (1991).

[80] P. Kruit, J. Kimman, H. G. Muller, and M. J. Van der Wiel, J. Phys. B At. Mol. Phys. **16**, 937 (1983).

[81] R. D. Johnson III, NIST Stand. Ref. Database 101 (release 16a) (2013).

[82] M. P. de Boer and H. G. Muller, J. Phys. B At. Mol. Opt. Phys. **27**, 721 (1994).

[83] P. Michel, L. Divol, D. Turnbull, and J. D. Moody, Phys. Rev. Lett. **113**, 205001 (2014).

[84] G. Tsaur, N.-H. Kang, Z.-H. Xie, S.-H. Chen, and J. Wang, Phys. Rev. A **83**, 033801 (2011).

[85] J. K. Wahlstrand and H. M. Milchberg, Opt. Lett. **36**, 3822 (2011).

[86] D. F. Gordon, IEEE Trans. Plasma Sci. **35**, 1486 (2007).

[87] G. Hine, Private Communication, University of Maryland College Park, 2014.

[88] E. Treacy, Quantum Electron. IEEE J. **QE-5**, 454 (1969).

[89] Y.-F. Xiao, H.-H. Chu, H.-E. Tsai, C.-H. Lee, J.-Y. Lin, J. Wang, and S.-Y. Chen, Phys. Plasmas **11**, L21 (2004).

[90] C.-H. Pai, M.-W. Lin, L.-C. Ha, S.-T. Huang, Y.-C. Tsou, H.-H. Chu, J.-Y. Lin, J. Wang, and S.-Y. Chen, Phys. Rev. Lett. **101**, 065005 (2008).

[91] C.-H. Lu, Y.-J. Tsou, H.-Y. Chen, B.-H. Chen, Y.-C. Cheng, S.-D. Yang, M.-C. Chen, C.-C. Hsu, and A. H. Kung, Optica **1**, 400 (2014).